Optimization of passivating contacts for high-efficiency p-type silicon solar cells

R. van der Vossen

TU Delft

Optimization of passivating contacts

for high-efficiency p-type silicon solar cells

by

R. van der Vossen

to obtain the degree of Master of Science
at the Delft University of Technology,
to be defended publicly on Wednesday May 17, 2017 at 13:00 PM.

Student number:	4241959	
Project duration:	August 1, 2016 – April 30, 2017	
Thesis committee:	Prof. dr. ir. M. Zeman,	TU Delft
	Prof. dr. A. Weeber,	TU Delft
	Dr. R. Ishihara,	TU Delft
	Dr. F. Feldmann,	Fraunhofer ISE, daily supervisor
	Dr. O. Isabella,	TU Delft, supervisor

This thesis is confidential and cannot be made public until May 17, 2017.

Fraunhofer ISE

TU Delft

Preface

This thesis is the result of a nine months research period to complete the graduation research project for the Master degree in Sustainable Energy Technology at Delft University of Technology. The research was conducted at the Fraunhofer Institute for Solar Energy Systems in Freiburg, Germany. After completing a Bachelor degree in Applied Physics I searched for an interesting topic to apply my obtained knowledge and further specialize my engineering abilities. I found what I was looking for in the Master Sustainable Energy Technology and from the beginning my attention was drawn to solar energy. The intriguing physical phenomena governing this technology, together with the abundance of solar irradiation, grasped my attention and made me decide to specialize in this form of renewable energy.

After interesting courses which touched upon the essential aspects of solar energy, and graduation courses which provided me with the in-depth knowledge necessary for the graduation project, I found a graduation topic which matched my interests at the Fraunhofer ISE. It has been a great experience conducting experimental research on passivating contacts. I would like to express my gratitude to my supervisor at Fraunhofer ISE, Dr. Frank Feldmann, for his excellent supervision and great discussions. He ensured I got the guidance I needed during my time at ISE and was always available to discuss results. I would also like the thank Dr. Olindo Isabella for his supervision from Delft. Despite the distance, I felt supported in my research and really appreciate the Skype meetings to discuss my progress. I would like to thank Dr. Olindo Isabella for introducing me at Fraunhofer as well, which made it possible for me to go abroad for nine months to do this research, resulting in this work.

Furthermore, I would like to thank dr. Martin Hermle for providing important and refreshing insight into my work. The technical staff at Fraunhofer ISE also made a great contribution to this thesis, especially F. Schätzle, A. Leimenstoll, A. Seiler, and S. Seitz. Thanks to their excellent work all the cleanroom processes ran smoothly and I received the samples I needed in the best possible condition. A big thanks to F. Martin for measuring my devices and making sure I received the nutrition I needed at the appropriate time.

I would like to thank all my other colleagues at Fraunhofer, both in the office and throughout the department, for enabling me to learn as much as I did during my time in Freiburg whilst also enjoying my time there. I also would like to express my gratitude to the members of my thesis committee for reading and discussing my work. Finally, I would like to thank my parents and my sister Merel for their unending support.

Solar energy will in my opinion make a significant contribution to the energy transition we will be facing in the coming decades or centuries. A lot of progress has been made on the topic of photovoltaics, this is something realized all the more whilst conducting my research in Freiburg. Cooperating with colleagues, some of whom worked at the institute before I was born, made me realize what incredible progress has been made in photovoltaics already. Therefore I believe that there is great potential in this technology and in the people contributing to improving this technology day after day. Finally, I would like to express my gratitude to all the people who made it possible for me to make a small contribution in this great field of research.

R. van der Vossen

Delft, May 2017

Abstract

The goal of this master thesis was to optimize the tunnel oxide passivating contact (TOPCon) concept for p-type substrates and implementation in silicon (Si) solar cells. TOPCon and other passivating contacts are believed to be a crucial link for increasing solar cell efficiency and further reducing the costs of photovoltaic (PV) systems. The concept that comes closest to the theoretical Auger limit is the Si heterojunction cell with a record efficiency of 26.6 % [1]. A problem with this type of cells is that the process temperature that is allowed is limited, increasing the processing temperature results in decreasing passivation and thus loss of efficiency.

The TOPCon concept can withstand higher processing temperatures, which is beneficial when it comes to applying a transparent conductive oxide (TCO) layer of certain metallization schemes. For n-TOPCon good results have been obtained in the past leading to a record efficiency of 25.7 % [2]. For p-TOPCon, the efficiency is significantly lower and the cause of this discrepancy is not fully understood yet.

In this work, the boron doped TOPCon configuration was optimized by optimizing all of the individual components of this passivating contact concept. During this work the tunnel oxide, which can be grown using various methods, proved essential to obtain a good passivation. A comparison was made between four different growth methods for the tunnel oxide, from which it was concluded that the thermally grown tunnel oxide performed best in terms of passivation quality and thermal stability. The optimal p-TOPCon stack was found to consist of three layers: a thin intrinsic hydrogenated amorphous silicon (a-Si:H) layer, followed by a boron doped a-Si:H layer. The p-TOPCon stack is finalized by depositing a thin silicon carbide (SiC) capping layer, which was also boron doped.

Besides passivation, the specific contact resistivity was also investigated. A metallization stack consisting of titanium, palladium, and silver proved to result in the lowest contact resistivity values. The lowest value which was measured was 10 mΩcm^2, this is below the threshold value for which fill factor (FF) losses are to be expected. Implementing a thin tungsten oxide (WO_x) layer underneath this metallization stack resulted in a stark increase in the specific contact resistivity values. Furthermore, the tunnel oxide influenced the contact resistivity values, where a lower oxidation time and temperature resulted in lower contact resistivity values. In order to better understand the correlation between contact resistivity and passivation, the contact resistivity values and corresponding recombination current values were fitted to two different models: the oxide tunneling model [3] and the pinholes model [4]. The measured resistivity values all laid in the saturated regime, which made it difficult to exclude one of the two models.

The passivation quality of the p-TOPCon stack was improved by altering the tunnel oxide to a thermally grown oxide and optimizing the TOPCon stack. This resulted in an implied open-circuit voltage (iV_{oc}) value of 710 mV and an implied fill factor (iFF) value of 84.5 %. A good contact was obtained with a titanium, palladium, silver metallization. This resulted in a specific contact resistivity value of 10 mΩcm^2.

Contents

1

Introduction

1.1. Motivation

In the transition from fossil fuels to renewable energy, PV technology will play a crucial role. Solar energy has a huge potential with the annual solar irradiation being 10000 times the current annual energy consumption [5]. Photovoltaic technology is a fast growing market with a growth rate of 41 % between 2000 and 2015 [6]. Silicon (Si) wafer based solar cells dominate the market with a market share of 93 % in 2015 [6]. Another clear trend in the silicon PV market is the decline of module prices over time with a learning rate of 23 % [6].

Since the module prices are on this steady decline, the non-module costs of a PV system are making up an increasing part of the PV system costs [5]. These costs, also called balance of system (BOS) costs, can be reduced by increasing the module efficiency. Several factors have to be addressed in order to produce more efficient modules. One of these aspects is the base material quality. Improved wafer production processes have allowed production of superior silicon wafers with less defects. This drastically reduces the bulk recombination and thus allows minority charge carriers to reside in the bulk material for a longer time, reducing losses and increasing the efficiency. Furthermore, there has been a trend of using thinner wafers as the base for solar cells to decrease resource consumption and module cost. These two factors have made losses at the wafer/contact surface more dominant, however.

A logical next step would be to bring down the surface recombination in solar cells in order to further increase the efficiency. In order to decrease the charge carrier recombination at the silicon/metal interface, several strategies have been proposed. One strategy is to minimize the silicon/metal surface area by covering most of the cell area with a passivating layer, usually a dielectric, and forming local contacts through the dielectric. This cell configuration is called passivated emitter and rear cell (PERC) [7, 8]. Passivation of the contacts is an essential step to further improve the Si based module efficiency and thus further reducing the cost of PV systems. For a n-type substrate, some successful passivation techniques have been developed, one of them is the TOPCon technology developed at Fraunhofer ISE [9].

In this thesis, optimization of the fabrication for p-type TOPCon passivating contacts will be investigated. The hole-selective TOPCon layer still shows inferior properties compared to the n-TOPCon counterpart. Since the majority of modules produced nowadays consist of p-type silicon, it could be of great interest to the industry to produce passivating contact solar cells on this substrate. This will further increase the effi-

ciency of the cells and thus allow for further decrease in the PV system costs.

1.2. Research objectives

As mentioned before, the main goal of this thesis is to optimize the passivation quality of the p-TOPCon contact. This will be achieved by optimizing the various components of the TOPCon configuration individually. Realizing these goals involves both experiments as well as modeling of the underlying behavior. The main research questions which will be addressed in this thesis are:

- What is the influence of the different components of the stack on the p-TOPCon passivation quality?
- What is the relationship between the saturation current density and contact resistivity?
- Which theory describes the behavior of the hole-selective contacts accurately?

1.3. Outline

In this thesis the optimization process of the boron doped TOPCon layer will be documented. In Chapter 2 the fundamental physical phenomena which describe semiconductor materials will be explained. This chapter furthermore deals with the basic working principles of silicon solar cells by the example of a pn homo-junction. Thereafter several concepts for overcoming the limitations of a homo-junction device will be addressed.

In Chapter 3, the various process techniques used for the fabrication of the TOPCon samples will be explained. The order of this chapter follows the process sequence during fabrication in order to ensure a good flow in the chapter. Chapter 4 deals with the characterization techniques used to evaluate the fabricated samples. For each technique the governing physical processes as well as the practical applications will be discussed.

After an introduction into the theory and the used methodology, the first results will be presented and discussed in Chapter 5. In this chapter the results from the optimization of the individual components will be presented and discussed, starting with the dopant concentration and the annealing temperature of the TOPCon stack itself. Thereafter, the tunnel oxide will be optimized and lastly the composition of the different layers within the TOPCon stack will be optimized. Concluding this chapter the first research question will be answered.

The second research question will be addressed in Chapter 6. Here the relationship between the surface recombination velocity and the specific contact resistivity will be investigated. The main part of this chapter deals with the influence of the tunnel oxide thickness and oxidation method on the contact resistivity and the passivation quality, the obtained data will be fitted to two theoretical models which describe this relationship.

2

Theory

In this chapter the theoretical framework to understand the work done during this master thesis will be provided. Firstly, a brief introduction to semiconductor device physics will be given based on the books by Colinge [10], Neamen [11] and Würfel [12]. Secondly, the generation and recombination of charge carriers in semiconductor material will be explained. Thereafter, the working principle of a solar cell will be explained by the hand of a pn homo-junction. Furthermore, the limitations of the homo-junction configuration will be discussed as well as several configurations to overcome these limitations. During this section, the focus will lie on poly-Si passivating contacts. Finally, an overview of the current status quo from research groups working on passivating contacts will be provided.

2.1. Semiconductor physics

A semiconductor material is a material which is typically a crystalline solid material or a solid with an amorphous structure. The resistance of a semiconductor is much higher than that of metals, yet also much lower than that of insulators. To explain the behavior of semiconductor materials one has to introduce quantum mechanics. According to quantum mechanics, there are only a limited number of energy levels an electron belonging to an atom can have. These 'quantized' levels can contain only two electrons with different spin, this phenomenon is called Pauli's exclusion principle [13]. The next electron will simply occupy a higher quantum state until all electrons are used up. The energy level that is then reached is called the Fermi energy. If the electrons have no thermal energy, this occurs at 0 °K, all the energy levels below the Fermi energy are completely filled and all the energy states above the Fermi energy are completely empty. At higher temperatures, the electrons gain thermal energy which causes some of them to occupy states with a higher energy than the Fermi energy. The formula describing the probability that a certain energy state is occupied is called the Fermi-Dirac distribution.

$$f(E) = \frac{1}{e^{\frac{E-E_F}{k_B T}} + 1} \tag{2.1}$$

In Equation (2.1), E is the energy of the state, E_F the Fermi energy, k_B Boltzmann's constant and T the temperature in °K.

Now, if we consider a crystalline structure made of these atoms, there is an interaction between the atoms

since they are positioned very close to each other. This interaction causes a splitting of the originally identical energy levels. In order to obey Pauli's exclusion principle, there will be a very small difference between the lowest energy state of each atom. The same for the second to lowest energy state etc. The difference between these energy levels is so small, that they can be considered as continuous bands of allowed energy states spanning several electron-volts. The bands with the lowest energies are always filled, and the highest band is always empty. The lowest ground-state band which is still completely filled at absolute zero is called the valence band, and the next band is called the conduction band.

The position of the Fermi Energy with respect to the conduction and the valence band, determines the conductivity of the material. For metals, the valence and the conduction band overlap, thus resulting in a Fermi level in both the conduction and the valence band. This makes transport of electrons very easy. For insulators, the Fermi level lies in the middle of the band gap, which usually spans several electronvolts (eV). This means that an electron has to gain several eV of energy in order to reach the conduction band, which is very unlikely to occur. For intrinsic semiconductors, the Fermi level also lies in the middle of the band gap,

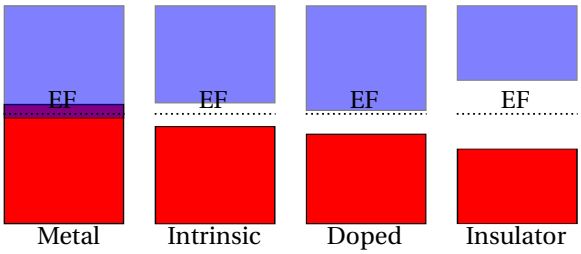

Figure 2.1: Band gap diagrams for materials with a varying conductivity.

but the size of the band gap is usually lower. This implies that the energy which is needed for an electron to be excited to the conduction band is lower. Furthermore, the semiconductor can be doped.

When a semiconductor is doped, atoms are introduced in the crystal lattice which have either an extra electron, or one fewer electron than the other atoms in the crystal lattice. These atoms are called electron donors or acceptors, respectively. These extra electrons or lack of electrons can shift the Fermi level towards either the conductance band (donor doped) or the valence band (acceptor doped). This increases the probability of electrons to be excited to the conductance band, or for p-type material, for electron vacancies to be created in the valence band. These electron vacancies will be indicated with the term hole from now on. The generation of these charge carriers leads to an increased conductivity. A graphical overview of the band gap diagrams for various materials can be found in Figure 2.1.

From Figure 2.1 one can see that for metals the conduction and the valence band overlap. As a consequence, electron transport in a metal is very easy. For the semiconductor material there is a relatively small band gap and for the doped case the Fermi level is shifted towards the conduction band. It can be seen from Equation (2.1) that this shifts the Fermi-Dirac distribution, making it more likely for an electron to be in the conduction band. For an insulator, with a band gap energy of several eV, exciting an electron to the conduction band becomes highly unlikely, as can be seen by looking at Equation (2.1). The behavior of the minority charge carriers after creation will be discussed in the following paragraphs.

There are five equations which, when combined, describe semiconductor devices in an orderly manner. The forces acting on electrons and holes respectively, are based on both the electrical and chemical potential gradients. The chemical potential gradient induces a diffusion current and the electrical potential gradient a drift current. Of course, these forces act on the charge carriers in all three dimension, but generally it is

justified to make the behavioral analysis in one dimension. The diffusion current density can be found in Equation (2.2a) for electrons and Equation (2.2b) for holes.

$$J_{n,diff} = qD_n \frac{dn}{dx} \tag{2.2a}$$

$$J_{p,diff} = -qD_p \frac{dp}{dx} \tag{2.2b}$$

In these equations D_n and D_p are the diffusion coefficients for the electrons and holes, respectively. Furthermore, q is the elementary charge and n and p are the carrier concentrations of the electrons and holes.

The drift current density is found in Equation (2.3a) for electrons and Equation (2.3b) for holes.

$$J_{n,drift} = q\mu_n nE \tag{2.3a}$$

$$J_{p,drift} = q\mu_p pE \tag{2.3b}$$

In these equations, μ is the carrier mobility and E is the electric field. The total current densities for holes and electrons can be obtained by adding the drift and diffusion current densities. The result can be found in Equation (2.4a) and Equation (2.4b).

$$J_n = q\mu_n nE + qD_n \frac{dn}{dx} \tag{2.4a}$$

$$J_p = q\mu_p pE - qD_p \frac{dp}{dx} \tag{2.4b}$$

These two equations partially describe the transport phenomena in semiconductor devices [11]. Another important equation is Poisson's equation. Poisson's equation is used to describe the field which is induced by a given charge density distribution. For the derivation, we start with Gauss's law in the differential form.

$$\nabla E = \frac{\rho}{\varepsilon} \tag{2.5}$$

In this equation, ∇E is the divergence of the electric field, ε the electric constant of the material and ρ the electric charge density per unit volume. According to Gauss's law, there is a proportionality between the flux going through a certain closed surface and the charge contained in that surface [14]. Combining this with the relation between the electric field and potential:

$$E(x) = -\frac{d\Phi(x)}{dx} \tag{2.6}$$

This equation shows that the electric field is equal to the derivative of the electric potential in the x direction. Combining both equations, Poisson's equation in one dimension is obtained.

$$\frac{d^2\Phi(x)}{dx^2} = -\frac{\rho}{\varepsilon_s} \tag{2.7}$$

In Equation (2.7), Φ is the electric potential, ρ the charge density and ε_s the permittivity of the semiconductor material. Poisson's equation is used to describe the potential energy field induced by the aforementioned charge distribution.

Finally, the continuity equations complete our set of equations to describe the transport phenomena in semiconductor materials. The continuity equations are a simple yet powerful tool to trace the charge carrier concentration over time in a certain volume. In order to track the change in charge carrier concentration appropriately, the continuity equations take into account three terms. In the first term, the change in current density over the length is determined. Of further influence are the external generation and the internal recombination rates [11]. The external generation rate is the number of charge carriers that get excited to

the conduction band due to external influences like illumination and heat. The internal recombination rate accounts for the number of charge carriers that recombine under thermal equilibrium conditions. Please note that this is a net recombination, thus this number also includes the internal generation rate. Adding these three terms results in equations describing the change in charge carrier concentration over time. Below Equation (2.8a) describes the excess electron concentration over time and Equation (2.8b) the excess hole concentration over time

$$\frac{\partial n}{\partial t} = \frac{1}{q}\frac{\partial J_n}{\partial x} + (G_n - U_n) \tag{2.8a}$$

$$\frac{\partial p}{\partial t} = -\frac{1}{q}\frac{\partial J_p}{\partial x} + (G_p - U_p) \tag{2.8b}$$

Where G_n and G_p are the external generation rates as mentioned above and U_n and U_p the internal recombination rates.

2.2. Generation and recombination

If an electron gains an amount of energy which is equal to or greater than the band gap energy, it can be excited from the valence band to the conduction band. In this process a hole is created in the valence band. Thus when an electron is excited a charge carrier pair is created. If an electron gains more than the band gap energy E_g it will get excited beyond the conduction band boundary. Very quickly after this initial excitation, the electron will transfer excess energy in to the lattice vibration, and fall back to the boundary of the conduction band. The transfer of energy to lattice vibration is indicated with the term phonon. The energy from the phonons is converted into heat and this process is called thermal relaxation.

After reaching the conduction band boundary, the electron can remain there for a relative long period in the order of milliseconds for silicon [12]. After this time the electron will fall back to the valence band and recombine with the hole. For a properly working solar cell it is important that the electrons and holes do not recombine until they are collected at their respective contacts. When the semiconductor material is in thermal equilibrium, the generation rate equals the recombination rate and there is no net growth or decay of the number of electrons and holes in the material. When the material is exposed to illumination, this changes. The photons that are absorbed can transfer their energy to electrons, thus providing them with enough energy to cross the band gap and get excited to the conduction band. The goal is then to keep these electrons and holes separated, although there are numerous processes that can undermine this.

There are three important processes that cause the recombination of electrons and holes in silicon. The first is called radiative recombination and is an unlikely recombination path for silicon solar cells. During radiative recombination the electron simply falls back to the valence band, whilst emitting a photon with the band gap energy. This type of recombination requires the lowest energy of the conduction band to occur at the same wave number as the highest energy of the valence band, these type of semiconductor materials are called direct-band gap materials. This is the case for materials like gallium-arsenide. Since silicon has a so called indirect band gap (which means the lowest conduction band energy is not at the same wave number as the highest valence band energy), energy from lattice vibrations (phonons) is required to change the momentum and thus the wave number of the electron, after which it can recombine with a hole. Since the probability that a phonon with the right momentum interacts with an electron is quite small, this recombination is also not found to be dominant for silicon materials. The second type of recombination is called Auger recombination, and this limits the ultimate efficiency of silicon solar cells to 29.4 % [15]. For Auger recombination a third charge carrier, which can be a hole or an electron, is necessary for the recombination process. When an

electron recombines with a hole, energy is emitted. During Auger recombination, this energy is transferred to the third charged particle instead of being emitted as a photon. The third charge carrier is then excited deeper into the valence or conduction band, depending on the charge and relaxes thermally. During thermal relaxation energy is transferred to the lattice and becomes useless for electricity generating purposes.

The third and last recombination mechanism is called Shockley-Read-Hall (SRH) recombination and is the dominant recombination process in most current silicon solar cells. SRH recombination is promoted by defects in the crystalline structure of the silicon and thus is more pronounced in multi-crystalline silicon or at the silicon surface than in the c-Si bulk. This is caused by the fact that at surfaces there is usually a mismatch in the crystal structures, resulting in unsaturated or 'dangling' bonds. These 'dangling' bonds are also called traps and they create an extra possible energy level in the band gap. Unlike dopants, which create energy levels close to the conduction or valence band, the traps create levels closer to the middle of the band gap. These new allowed energy levels, also called the defect band, serve as a stepping stone for the electron to fall back to the valence band, thus losing an electron-hole pair. The internal recombination of SRH-recombination is described by the following equation [16]

$$U_s = \frac{n_s p_s - {n_i}^2}{\frac{n_s + n_1}{S_{p0}} + \frac{p_s + p_1}{S_{n0}}} \tag{2.9}$$

where $n_1 = n_i e^{\left[\frac{(E_t - E_i)}{k_B T}\right]}$ and $p_1 = n_i e^{\left[\frac{(E_i - E_t)}{k_B T}\right]}$ are statistical factors, E_t is the trap energy of the defect in the band gap. $S_{p0} = \sigma_p \nu_{th} N_{st}$ is the surface recombination rate of holes and $S_{n0} = \sigma_n \nu_{th} N_{st}$ that of electrons. For the surface recombination velocity, σ is the capture cross section, N_{st} is the number of surface states per unit area and ν_{th} the thermal velocity of the charge carriers. Furthermore, n_s and p_s are the electron and hole concentrations at the surface of the semiconductor interface. E_i is the intrinsic Fermi energy, T the temperature and k_B Boltzmann's constant.

Equation (2.9) shows that in order to minimize recombination, N_{st} should be as small as possible and the charge carrier concentrations should be adjusted to the type of charge-carrier that is to be extracted at the contact. The bulk recombination has been substantially decreased over the years due to better wafer production processes. As a consequence, the majority of the recombination that occurs, happens at the surfaces of the silicon material. In order to reduce the recombination here, there are two commonly used strategies. The first is through chemical passivation of the surface. Here the number of surface states is reduced by passivating the dangling bonds via for example hydrogen passivation or via the application of a dielectric that passivates the bonds through hydrogen effusion [17]. The second strategy focusses on repelling one type of charge carrier at the surface whilst attracting the oppositely charged carriers. This method of passivation is called field effect passivation. Usually, a dielectric containing charge or a higly-doped region is applied on top of the silicon surface. The excess charge carrier in the dielectric/highly-doped region recombine with the charge carriers of opposite charge at the surface, thus reducing the effective charge carrier concentration and recombination [18]. There is an optimum dopant concentration when it comes to minimizing the recombination losses. In order to reduce the charge carrier concentration as much as possible, the doping concentration should be as high as possible. However, doping concentration has to stay below a value of typically $N_{D,n+} \approx 10^{18}$ cm^{-3}. If the doping concentration is increased beyond this point, band gap narrowing and Auger recombination become the dominant recombination process, undermining the passivating quality of the contact[19, 20].

2.3. Basic solar cell operations

The working principle of solar cells relies on the conversion of photons to electricity. This is achieved by converting the energy of the photon to chemical energy, which is then converted into electrical energy. In order to understand the functioning of a solar cell, a situation with two differently doped Si layers is considered. One layer is phosphorus doped, which has shifted the Fermi level to the conduction band, and the other boron doped. A schematic representation can be found in Figure 2.2a. Before these two layers are joined, they can be considered as isolated with each their own Fermi level:

$$E_{Fn} = E_C + k_B T ln\Big(\frac{N_D}{N_C}\Big) \tag{2.10a}$$

$$E_{Fp} = E_V + k_B T ln\Big(\frac{N_A}{N_V}\Big) \tag{2.10b}$$

Where N_D and N_A are the donor and acceptor concentrations, respectively. N_C and N_V are the density of states for the conduction and valence band, respectively. And finally, E_C and E_V the energies of the conduction and valence band, respectively. If one of these layer is now illuminated it will cause a splitting in the Fermi level. These so-called quasi Fermi levels is what drives the current in a solar cell, but since no potential difference is present there is no current flow in the layers at this moment.

If the phosphorus and boron doped Si layers are joined, which is called a pn-junction. The Fermi levels will come to an equilibrium. This leads to a bending of the conduction and the valence band which can be found in Figure 2.2b. The electrons in the n-type material close to the junction will diffuse into the p-type material and recombine with the holes there, leaving behind charged ions. The region where the minority charge carrier have recombined is called the space-charge region or the depletion region. Due to these charged ions, an electric field is generated in the depletion region. From Poisson's equation, it is known that integrating the electric field over the entire depletion region calculates the potential difference between the n-type and the p-type layer, which is called the built-in voltage. This is described by Equation (2.11).

$$V_{bi} = \frac{k_B T}{q} ln\Big(\frac{N_A N_D}{n_i^2}\Big) \tag{2.11}$$

In this equation n_i^2 is the intrinsic charge carrier concentration and this is described using the following equation:

$$ni^2 = N_c N_v e^{\frac{E_g}{kT}} \tag{2.12}$$

If an incident photon with sufficient energy gets absorbed ($E_{ph} \geq E_g$) by one of the layers, an electron can be excited to the conduction band from the valence band as described in Section 2.2. The chemical energy that is produced equals the sum of the electrochemical potentials of holes and electrons, which on it's turn equals the energy difference between the quasi-Fermi levels and is described by Equation (2.13).

$$E_{Fn} - E_{Fp} = k_B T \ln\left(\frac{(p_0 + \Delta p)(n_0 + \Delta n)}{n_i^2}\right) \tag{2.13}$$

With p_0 and n_0 are the equilibrium concentrations for holes and electrons, respectively. Δp and Δn are the excess concentrations generated when the semiconductor material is illuminated. To convert this newly generated chemical energy into electrical energy, the electrons and holes have to be separated. Under illumination the Fermi level is split in the 'quasi Fermi' levels as mentioned before. The gradient in the quasi Fermi levels causes a potential difference over the terminals, which drives the electrons and holes to their respective contacts. This can be described by the following equation [12]:

$$V = \frac{1}{q} \int_{\frac{-W}{2}}^{\frac{W}{2}} \frac{dE_{FC}}{dx} \mathrm{d}x. \tag{2.14}$$

with W the width of the junction, $\frac{dE_{FC}}{dx}$ the gradient of the Fermi energy at the conduction band. This voltage is a measure for the potential difference between the quasi Fermi levels and is called the iV_{oc}.

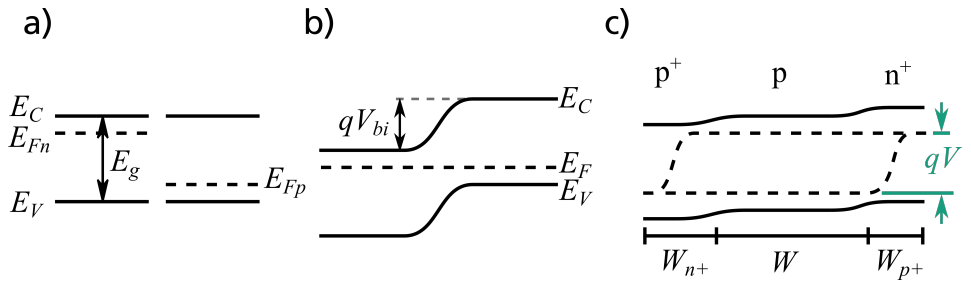

Figure 2.2: Energy band diagram of (a) separated n- and p-type Silicon, (b) a pn-junction in thermal equilibrium and (c) under illumination at open-circuit conditions. Picture taken from [21].

In order to successfully collect the charge carriers at the designated terminals, the built-in voltage has to exceed the splitting of the Fermi energy into the quasi Fermi levels as described in Equation (2.13). This leads to the following condition:

$$V_{bi} \geq \frac{k_B T}{q} ln\Big(\frac{\Delta n(\Delta n + N_A)}{n_i^2} \cong iV_{oc}\Big) \tag{2.15}$$

Usually this requirement is fulfilled since the doping concentrations in the emitter and the p-type region at the rear of the solar cell exceed the excess carrier concentration at 1 sun with ease. Under illumination conditions, the difference between the Fermi level energies is smaller than the band gap of the material. This implies an incomplete conversion of energy, which can be explained by the fact that entropy is generated during the conversion process [12].

2.4. Limitations of homojunctions

As described in Section 2.3 the front and backside of the homojunction solar cell consist of a highly doped ($N_D = 1 \cdot 10^{19} - 1 \cdot 10^{20} \text{cm}^{-3}$) Si region. This high doping concentration causes band gap narrowing due to interaction between the charge carriers, which can no longer be described as free electrons completely, and increased Auger recombination. The recombination at the semiconductor metal interface also proves to be a limitation to the efficiency of the homojunction solar cells. As mentioned in Section 2.3, the built-in voltage has to exceed the difference in the quasi Fermi levels. To achieve this, a high doping concentration in the n^+ and p^+ type region is required. This is usually not a problem for homojunction devices, but comes at the cost of higher Auger recombination and band gap narrowing as mentioned before.

Several strategies have been implemented to reduce these unwanted side-effects as much as possible. The recombination at the semiconductor metal interface can be reduced by minimizing the surface area between the two. To achieve this, typically the semiconductor material is passivated by a dielectric such as silicon nitride (SiN_x), aluminium oxide (Al_2O_3) or silicon oxide (SiO_x). Local point contacts are made in the coating to allow charge carriers to flow to the metal contact, whilst minimizing the surface area. This PERC configuration has increased the homojunction efficiency significantly [7, 8]. Further modifications focus on light trapping technology to boost efficiencies, leading to more complicated production procedures, however.

2.5. Passivating and carrier selective contacts

2.5.1. amorphous silicon/c-Si heterojunction

As an alternative way to overcoming the fundamental limitations of homojunction solar cells, different solar cell configurations have been proposed. One of the successful ones is the heterojunction solar cell. Instead of using the same semiconductor material with a different type of doping, but the same band gap, two different semiconductor materials with different band gap energies and different doping are used. Due to this difference in band gap energy, the minority carrier recombination at the metal contacts can be minimized, since a barrier can be created for one of the charge carriers. A very common heterojunction consists of an amorphous silicon (a-Si) c-Si junction, for which the typical band diagram can be found in Figure 2.3. Figure 2.3 shows

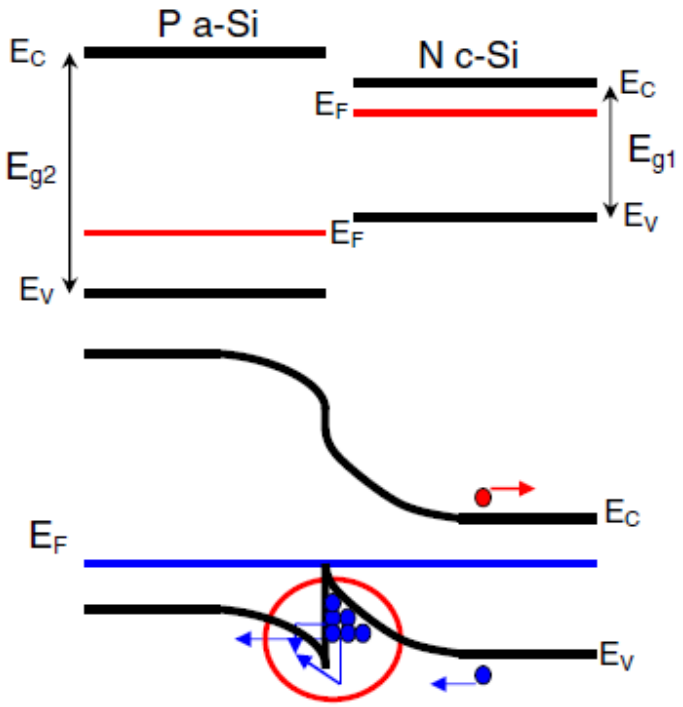

Figure 2.3: Energy barrier for holes in a a-Si/c-Si heterojunction. Due to the larger bandgap in the a-Si, an energy barrier is created in the valence band. This limits the transport of holes, whilst promoting the transport of electrons. Picture taken from [22]

that a-Si has a higher bandgap energy than c-Si, whilst it still can be doped with both boron and phosphorus [23].

Research has shown however, that a very thin layer of intrinsic a-Si is essential to reduce the interface trap density to such an extent that excellent chemical passivation can be achieved [24]. With this configuration, which is also named Heterojunction with Intrinsic Thinlayer (HIT), high efficiencies have been achieved [25]. A problem with this type of solar cells is the poor blue response. This is mostly caused by the boron doped a-Si:H layer which is a source of parasitic absorption [26], thus should be as thin as possible, whilst still achieving a good passivation. The parasitic absorption can be overcome by merging the heterojuncion with inderdigitated back contact (IBC) technology. With this configuration the world record efficiency of 26.6 % has been achieved, but the production process of these types of cells is complex, making large scale industrial implementation unlikely [1]. Futhermore, the a-Si:H layers are sensitive to high temperature treatments

which limits the back-end processing like deposition of a TCO layer and the metallization, since these processes usually require high temperature steps [27].

2.5.2. poly-Si passivating contacts

Another way to suppress recombination at the surface of solar cells is through passivating contacts. The so-called poly-Si/SiO_x emitter technology was first developed for bipolar junction transistors, where it has demonstrated significant current gains by minimizing the minority carrier recombination [28]. The poly-Si passivating contacts consist of a thin oxide layer with a thickness of less than 20 Å and a heavily doped poly-Si layer on top. This technique was historically heavily used for the micro-electronics industry, where traditionally a chemically grown oxide was used and thereafter an a-Si or poly-Si layer was grown using low pressure chemical vapour deposition (LPCVD). The deposited silicon layer would then be doped and annealed at high temperatures to drive in and activate the dopant atoms. The high temperature anneal would cause break-up of the chemically grown oxide which would decrease the specific contact resistivity, but increase the leakage current. This lead to a problematic trade-off in passivation quality and specific contact resistivity that has been the subject of many experiments since then.

The first application of a poly-Si passivating contact to solar cells was done by Lindholm et al. [29]. In the same year a successful attempt was reported by Yablonovitch et al., which was named the semi-insulating polysilicon (SIPOS) solar cell. This resulted in a high open-circuit voltage (V_{oc}) value of 720 mV but no reported FF [30]. Some early approaches where made to improve the solar cell efficiency using poly-Si contacts by Tarr et al. in the same year [31]. In 2008 renewed interest arose for the poly-Si contacts after a successful attempt from Borden et al., who created the poly-Si contact using equipment from the integrated circuit (IC) industry like rapid thermal processing (RTP) and LPCVD. The idea for this solar cell for which the passivating contact consists of a 6-12 Å thick tunnel oxide and an doped poly-Si layer, paved the road for further development of the passivating contacts, although the V_{oc} and FF values of this cell were not record breaking [32].

The first time passivating contacts showed a significant improvement of the solar cell efficiency was through a passivating contact concept named TOPCon, which was introduced by Feldmann et al. [33]. The TOPCon is based on the poly-Si passivating contacts. However, the poly-Si layer is replaced by SiC, since this material has a wider band gap than crystalline silicon, a heterojunction is created. Between the bulk wafer and the SiC layer a tunnel oxide is grown which acts a a barrier where the carriers need to tunnel through. The tunnel oxide is grown using either wet chemical oxidation [34–36] or UV light is used to create ozone [37]. A third technique is the growth of a tunnel oxide using rapid thermal oxidation [38], but a drawback of this technique is the high thermal budget and the difficulty to obtain a stable process which results in good passivation time after time. After this the doped Si is deposited on the tunnel oxide using plasma enhanced chemical vapour deposition (PECVD). Finally, the structure is annealed at a high temperature (800-1000°C) to partially crystallize the Si layer and activate the dopants [39]. The highly doped region strongly reduces the surface recombination at the metal/semiconductor interface, this enabled high V_{oc} and FF at the same time [40].

One of the advantages of this configuration is the fully contacted backside which enables current flow perpendicular to the irradiated surface, thus eliminating FF losses which are typically observed in PERC solar cells [9]. This cell architecture built on a n-type float-zone wafer has resulted in a very high V_{oc} of 718 mV, together with an FF of 83.2 % which resulted in a record efficiency of 25.7 % for double sided contacted solar cells [2]. The cell configuration can be found in Figure 2.4. To achieve these excellent characteristics one

has to obtain very good interface passivation together with highly doped layers and efficient majority carrier transport. The interface passivation proved to be very good which resulted in high lifetimes. The resulting

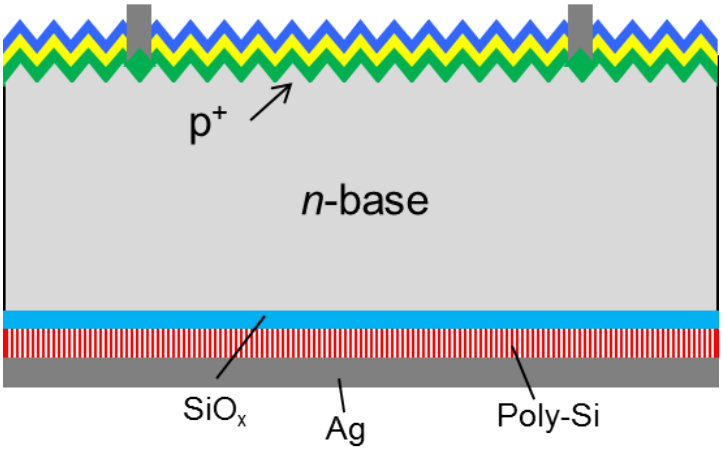

Figure 2.4: Schematic representation of the n-TOPCon structure at the rear of the cell. Picture taken from [41].

structure can be produced more easily than more complicated cell configurations like the IBC solar cells and is more stable to high temperature back-end processing than a-Si heterojunction solar cells [9].

Since the majority of the market share for commercial solar cells consists of p-type semiconductor material, TOPCon contacts for p-type silicon were also developed [21]. A good measure for comparing the passivation quality of passivating contacts it the recombination current J_0. For n-type passivating contacts low recombination current values around 10 fA/cm^2 have been reported, whereas for p-type material these values typically lie around 20 fA/cm^2 [42]. Multiple explanations for the lower passivation quality for p-type contacts have been proposed: larger diffusivity of boron in silicon, fewer boron atoms which have been ionized are segregated in the grain boundaries [43]. Furthermore, the boron atom induces more defects in the Si/SiO_2 interface. This is caused by penetration of boron into the substrate [44]. Therefore the p-type TOPCon contact has thus far not reached the excellent V_{oc} and FF values that were achieved for n-TOPCon. As mentioned above, Gan & Swanson saw that for higher annealing temperatures the oxide started breaking up which correlated with a sharp drop in the contact resistance. They concluded that this indicates that instead of charge carriers tunneling through the oxide barrier, another transport mechanism becomes dominant [45]. Peibst et al. have indicated that this other transport phenomenon might be local current transport through pinholes [4]. This might be worth exploring as deliberately formed pinholes could decrease the contact resistivity, thus improving the contact. This will contribute to the subject of this thesis which is to optimize the p-TOPCon passivating contact.

2.5.3. Other passivating contacts

Besides the passivating contacts based on silicon, more options have been explored resulting in good passivating contacts. Promising results have been obtained with transition metal-oxides (TMO). In these configurations, the metal-oxides either replace the doped silicon layer, or are inserted as an additional layer between the doped silicon layer and the TCO [46]. Two promising candidates are molybdenum oxide (MoO_x) and WO_x which originate from organic photovoltaics and are now applied to silicon photovoltaics. Since these metals have a high work function they cause a band bending of the silicon which makes it a suitable hole-contact. Battaglia et al. explored sub-stoichiometric MoO_x as a hole-selective contact. This resulted in a open-circuit

voltage of 711 mV and a conversion efficiency of 18.8 % [47].

Bivour et al. have also conducted research on MoO_x and WO_x. This resulted in passivating contacts with a V_{oc} of 630 and 660 mV for MoO_x and WO_x, respectively [46]. Another promising candidate is the titanium oxide (TiO_x). Liao et al. have used atomic layer deposition (ALD) to thermally deposit TiO_x films on undiffused crystalline silicon resulting in very low surface recombination velocities of 2.8 cm/s and 8.3 cm/s for n-type and p-type c-Si wafers, respectively [48]. Allen et al. achieved similar surface recombination velocity of 6.1 cm/s for gallium oxide (Ga_2O_3) on crystalline silicon, where they explored a range of deposition parameters resulting in layers of 4.5 nm thickness with good surface passivation [49].

A further benefit to these type of contacts with respect to their doped silicon counterparts is the lower thermal budget. All the process steps for both the MoO_x and WO_x as well as for the TiO_x contacts occur at a temperature below 200°C, for and Ga_2O_3 this is below 400°C, which is still much lower than for the TOPCon layer where a annealing step with temperatures of 800-950°C are the norm. The lower thermal budget is also a limiting factor since it prohibits certain metallizations and deposition of certain TCO layers. Despite the low surface recombination velocity, V_{oc} V_{oc} values lag behind the values found for the TOPCon configuration.

2.6. Status quo

Worldwide there are a several research groups working on passivating contact configurations similar to TOPCon. In this section an overview of the state-of-the-art projects will be given. The Institute for Solar Energy Research (ISFH) in Hamelin studied and compared the performance of thermally and chemically grown tunneling oxides, varying different parameters for each type. For both types of oxides good passivation characteristics were achieved. For the thermal oxide a J_0 of 5 fA/cm^2 was achieved in combination with a contact resistance of 0.1 Ωcm^2. For a chemically grown oxide a J_0 of 20 fA/cm^2 was measured with a contact resistance of 0.0121 Ωcm^2 [50].

Tempress developed a n-type poly-Si passivating contact for the use with industrial solar cells in collaboration with the Dutch energy research center ECN. This research focusses on the use of low-cost processes which can be applied on a industrial scale. The resulting bifacial solar cells reach an efficiency of 20.7 % with an average V_{oc} value of 674 mV [51]. The Photovoltaic Materials and Devices research group from Delft University of Technology studies passivating contacts on a poly-Si basis as well. Their latest results include a 21.2 % n-type IBC cell with a V_{oc} of 692 mV using ion-implanted poly-Si as the passivating layer [52].

The American research institute NREL also researched passivating contacts. Their most recent publications show that chemically grown oxides for a n-type passivating contact result in iV_{oc} values of well above 700 mV combined with a contact resistivity of 20 mΩcm^2. The NREL reproduced the TOPCon cell resulting in a solar cell with 21.48 % efficiency and an iV_{oc} of 698 mV and a FF of 78.37 % [53]. Furthermore, NREL looked into the major barriers for p-type passivating contacts, which typically shows lower quality passivation than their n-type counterpart as was also found by Feldmann et al. [21]. One of the most probable causes for the lower passivation quality was found to be hydrogen blistering and pinhole formation, which undermine the barrier quality of the tunneling oxide layer. Boron diffusion into the wafer and aggregation on the tunnel oxide/wafer interface was found to be a possible cause for the SiO_2 degradation and possible break-up. The resulting solar cells after metallization have a V_{oc} of 676 mV and a FF of 79 % which give an efficiency of 20.3 %. Less than the typical n-type passivated solar cells [54].

At Georgia Tech a tunnel oxide passivating contact which uses poly-Si technology has been developed for large-area n-type solar cells. The parameters during the various production processes were optimized. First the PECVD process was optimized by varying the SiH_4/PH_3 flow rate and the H_2 flow rate. It was found

that the higher H_2 rate improved the passivation. The annealing temperature was optimized and the best passivation was found to occur at 875°C. Furthermore the oxidation process which is used to grow the tunnel oxide was optimized in terms of processing temperature and used power. These optimal parameters resulted in a contact with a V_{oc} of 730 mV and a FF of 84.5 %. The resulting cell efficiency was 21.2 % [55]. From the literature available it can be concluded that the n-type passivating contact are quite reproducible and achieve excellent passivation. For their p-type counterparts these results have not yet been achieved.

2.7. Contact resistivity and saturation current relationship

As described above in Section 2.5.2 the oxide ideally acts as a semi-permeable membrane that allows charge carriers of one kind to pass with easy, whilst effectively blocking transport of the other type of charge carrier. In order to design effective cells, a thorough understanding of the transport phenomena which occur in these oxide layers is required. This section will elaborate on the most common theories and in Chapter 6 these theories will be compared to the obtained experimental data.

2.7.1. Oxide tunneling theory

One of the theories that describe the current flow across a barrier is called tunneling. Tunneling is a phenomenon described by quantum mechanics and is used to describe the non-zero probability of a particle crossing a barrier for which it classically does not have sufficient energy. The phenomenon is related to the Heisenberg uncertainty principle. A theoretical description about the mathematical description of this phenomena as well as the historical context can be found in ref. [13].

A mathematical description of the tunneling current through an oxide similar to the one used in the TOPCon configuration will be given next based on the derivation as found in ref. [3]. This derivation is semi-classical, assuming two semiconductor regions separated by an insulating layer (the tunneling oxide). The mean thermal velocity of holes which is given by the following equation:

$$\nu_{th} = \sqrt{\frac{8k_B T}{\pi m_{eff,h}}} \tag{2.16}$$

where k_B is the Boltzmann constant, T the temperature in $^\circ K$ and m_{eff} the effective mass of holes, which is assumed to be isotropic, or equal in different directions. If we now want to describe the net current in the x direction the following equation is used:

$$J_h = \frac{q {n_{io}}^2 \nu_{th} P_{t,h}}{N_{eff}} \tag{2.17}$$

where n_{io} is the charge carrier density in intrinsic silicon, N_{eff} the effective charge carrier density, q the elementary charge and P_t the tunneling probability.

This expression for the tunneling current is valid under the assumption that both regions contain silicon. The tunneling probability P_t can be described by looking at the tunneling through a rectangular barrier, which is a typical problem described by quantum mechanics, and described by the following equation:

$$P_{t,h} = \mathrm{e}^{\frac{-2t_{ox}}{\hbar}\sqrt{2qm_{eff,ox}\phi_{ox}}} \tag{2.18}$$

where t_{ox} is the oxide thickness, $m_{eff,ox}$ the effective hole mass in the oxide and ϕ_{ox} the barrier height of the oxide, the hole energy is set to zero in this example. Besides the tunneling current, a recombination current also occurs at the Si/SiO_x interface. This recombination current is described by Equation (2.19)

$$J_{rec} = \frac{q n_{i0}^2 S_{int}}{N_{eff}} \tag{2.19}$$

In Equation (2.19) S_{int} is the recombination velocity at the Si/SiO_x interface. Adding the tunneling and the recombination current leads to an expression for the saturation current which can be found in Equation (2.20).

$$J_0 = \frac{q n_{i0}^2 S_{int}}{N_{eff}} + \frac{q {n_{io}}^2 v_{th} P_{t,h}}{N_{eff}} \tag{2.20}$$

Besides the saturation current density, another important parameter is the specific contact resistivity. This is described by the following equation:

$$\rho_c = \frac{k_B T}{q^2 N_{eff} v_{th} P_{t,e}} \tag{2.21}$$

with $P_{t,e}$ the electron tunneling probability described analogously to Equation (2.18) just with the electron barrier height and effective mass.

From Equation (2.17) and Equation (2.21) is becomes clear there is a trade-off between the saturation current and the contact resistivity since both depend on the hole or electron current, respectively.

Table 2.1: Input parameter values for the oxide tunneling model

Parameter	**Value**	**Units**
$m_{\mathrm{e,eff}}$	0.3	
$m_{\mathrm{h,eff}}$	0.4	
$\phi_{\mathrm{ox,e}}$	4.7	eV
$\phi_{\mathrm{ox,h}}$	3.2	eV
N_{eff}	$4{\cdot}10^{18}$	cm^{-3}
T	298.15	K
t_{ox}	0.5-1.5	nm

An exemplary diagram of the relationships for different interface recombination velocities can be found in Figure 2.5. The parameter values which were used can be found in Table 2.1 and are adopted from earlier work by Graaff et al. [56].

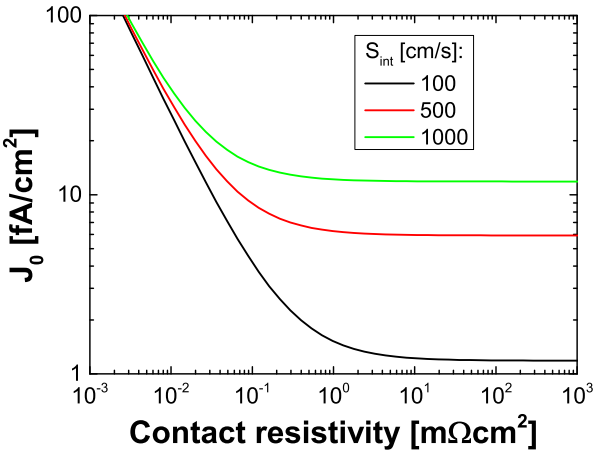

Figure 2.5: Plot of the contact resistivity versus the saturation current for various interface recombination velocities . In order to cover the full range of contact resistivity the oxide thickness was varied from 0.5 to 5 nm.

Figure 2.5 shows different behavior depending on the oxide thickness. For thin oxides, which corresponds

to a low contact resistivity, The tunneling becomes dominant and the recombination current increases significantly with decreasing oxide thickness. For a thicker oxide, the recombination at the interface becomes dominant, and the recombination current stabilizes. This leads for a saturated regime for the higher oxide thickness.

2.7.2. Pinhole theory

Another theory is that the annealing at high temperatures causes the oxide to deteriorate and eventually break-up. This is clearly observed for the chemically grown oxides at high temperature anneal, the pinhole theory assumes that before the oxide breaks up entirely, small punctures are created, named pinholes. These pinholes allow local contacts between the bulk material and the contact, thus enhancing the transport of charge carriers and increase of the saturation current. Two of the commonly found models will be described next. The first model is described extensively in [57], but will be summarized below. This model assumes a PERC like structure to account for the hole current. A schematic representation of the assumed situation can be found in Figure 2.6.

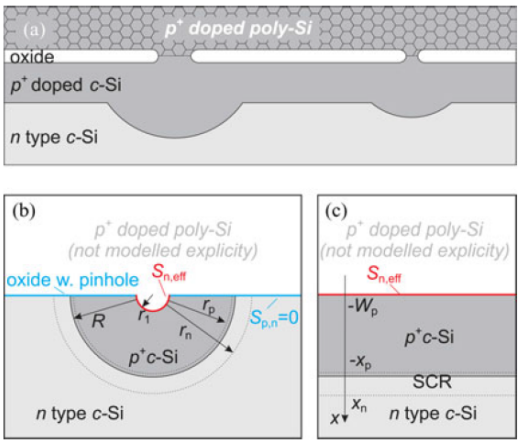

Figure 2.6: Schematic representation of the pinhole situation as described by Peibst et al. in ref [57].

In Figure 2.6 a typical passivating contact as is the case for the TOPCon structure is shown. In this case a n-type base material is taken and an oxide is grown on top of the substrate. Thereafter, a boron doped layer is deposited on top of the oxide and a high temperature anneal causes both a local break-up of the oxide as well as a diffused p-type region in the normally n-type substrate. It is assumed that in the regions where an oxide still exists, there is no recombination of charge carriers. Where there is a pinhole however, there is assumed to be an electron recombination velocity $S_{n,eff}$. These assumptions lead to equations for the hole current density J_p which can be found in Equation (2.22).

$$J_p = -qD_p p_{n0} r_n e^{\left(\frac{r_n}{L_p}\right)} \left(e^{\left(\frac{qV}{V_{th}}\right)} - 1\right) e^{\left(\frac{r_n}{L_p}\right)} \left(\frac{1}{r_n L_p} - \frac{1}{{r_n}^2}\right) \tag{2.22}$$

This hole current density is then used to calculate the saturation current density which can be found in Equation (2.23).

$$J_{0p} = \frac{J_p A N_{pin}}{(e^{qV/kT} - 1)} \tag{2.23}$$

In Equation (2.23), N_{pin} is the fraction of the surface that is covered by pinholes, and $A = 2\pi r_n^2$ the surface area of the dome of doped material that is formed under the pinhole. Furthermore, the specific contact resistivity

Table 2.2: Input parameter values for the pinhole model

Parameter	**Value**	**Units**
S_{met}	$1{\cdot}10^{7}$	cm/s
r	2	nm
W	140	nm
T	298.15	K
N_A	$4{\cdot}10^{18}$	cm^{-3}
p	$5{\cdot}10^{-7}$-$5{\cdot}10^{-2}$	$\#/\text{cm}^2$

can be found in Equation (2.24).

$$R_S = \frac{1}{2q\mu_p p_{p0}\pi N_{pin}} \cdot \left(\frac{1}{r_1} - \frac{1}{R}\right) \tag{2.24}$$

A graphical representation of the behavior of this model can be found in Figure 2.7. The dotted line indicates the model described above which has no recombination at the passivated fraction of the contact. One can see that for increasing contact resistivity, or lower pinhole density, the saturation current density continues to decline.

An elaboration to this model was done by Peibst et al. [4] where recombination at the oxide surface was taken into account. For this situation, which is based on the model developed by Fischer [58], the contact resistance contains two parts which can be seen as two parallel resistance contributions. The contact resistance of the pinholes is described by Equation (2.25) and is indicated with R_s.

$$R_s = p^2 \frac{\rho}{2\pi r} \arctan\left(\frac{2W}{r}\right) + \rho W \left\{1 - \exp\left(-\frac{W}{\rho}\right)\right\} \tag{2.25}$$

In Equation (2.25), p indicates the pinhole spacing, r the pinhole radius, W the thickness of the doped region underneath the tunnel oxide and ρ the resistivity of the doped region Furthermore, there is the contribution from the passivated region is indicated with $\tilde{R}_s$ which is described in Equation (2.26).

$$\frac{1}{\tilde{R}_s} = \frac{1}{\rho W} - \frac{2\pi r}{\rho p^2 \arctan\left(\frac{2W}{r}\right)\exp\left(\frac{W}{p}\right)} \tag{2.26}$$

These two contributions to the contact resistivity are added in parallel to achieve to total contact resistivity, but since generally the resistance of the passivated region is quite small, it is approximated by Equation (2.25). The two contributions to the contact resistance are implemented in Equation (2.27) to calculate the saturation current.

$$J_0 = D n_0 \left\{\left(\frac{R_s}{\rho} + \frac{D}{f_c S_{pin}}\right)^{-1} + \left(\frac{\tilde{R}_s}{\rho} + \frac{D}{(1-f_c) S_{ox}}\right)^{-1}\right\} \tag{2.27}$$

In Equation (2.27), the influence of the two resistance contributions R_s and $\tilde{R}_s$ is evident as well as the fraction of the area that is covered in pinholes f_c, the diffusion constant of the minority-carriers D and the surface recombination velocities at both the pinholes (S_{pin}) and the oxide (S_{ox}). In Figure 2.7 the saturation current is plotted against the contact resistivity for several values of the surface recombination values at the passivated region. Again the used parameters can be found in Table 2.2, which are mostly adopted from earlier work by Peibst et al. [4]. The depth of the profile and the acceptor concentration were adopted from the ECV profile, as will be explained more elaborately in Section 6.4.

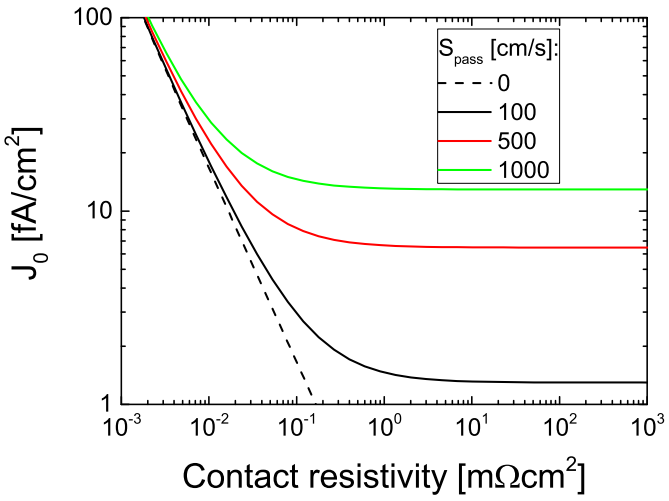

Figure 2.7: Plots of saturation current versus contact resistivity for various surface recombination velocities. The original model has a $S_{ox} = 0$ [57].

From Figure 2.7 it is observed that the behavior of the pinholes model which takes into account recombination at the passivated fraction of the contact is analogous to the oxide tunneling model. For higher values of the contact resistivity the saturation current stabilizes instead of further decreasing into the sub-fA regime, which does occur for the original model where perfect passivation is assumed at the oxide interface.

3

Processing techniques

In this chapter the processing techniques used to fabricate the lifetime samples and solar cells will be discussed and the underlying physical phenomena will be explained. To keep a logical flow in this chapter the processes will be described in the order in which they occur during lifetime sample fabrication.

3.1. Base material and cleaning

The lifetime samples and solar cells were fabricated on float zone (FZ) materials with varying bulk resistivity, typically 1 or 10 Ωcm. The samples received the cleaning procedure which became the standard cleaning routine for silicon wafers and originates from the Radio Corporation of America and is hence called RCA cleaning. The goal is to clean the wafers of organic and metallic residues and prepare the wafers for further processing.

The standard cleaning sequence at Fraunhofer ISE is described hereafter [59]. During each step an oxide is grown on the wafer surface, which is thereafter removed in hydrofluoric acid (HF). First the wafers are rinsed in deionized water (DI water) and afterwards submerged in boiling nitric acid (HNO_3). The grown oxide was then removed by a HF dip and the wafer was rinsed in DI water. Thereafter, the first step from the RCA cleaning sequence, called SC-1 is commenced. This step is used to clean the wafers of any organic and particle contamination. It consists of rinsing the wafers in DI water and thereafter submerging them in a mixture of DI water, ammonium hydroxide (HNO_3) and hydrogen peroxide (H_2O_2) heated to 70 °C. After the submerging the wafer is again rinsed thoroughly with DI water and a HF dip is used to remove the oxide. A second cleaning step, called SC-2, can be implemented to remove any metallic contamination which is present on the wafer. This step starts with submerging the wafer in a mixture of DI water, hydrogen chloride and hydrogen peroxide which is again heated to 70 °C. After submerging the wafers in this solution further rinsing with DI water is required.

During the cleaning procedure and the storage afterwards the surface of the wafer is oxidized, resulting in a thin native oxide on the silicon wafer. Since this is not wanted during the following process steps, a short dip HF is required to etch the oxide layer and expose the bare silicon surface after which the wafers, which are now hydrophobic, are rinsed one last time and then dried in a nitrogen atmosphere to minimize oxidation until the wafers are further processed and receive their tunneling oxide [60]. This HF dip is done right before

further processing is commenced in order to minimize the risk of re-contaminating or re-oxidizing the wafer.

3.2. Oxide growth

After cleaning the wafer a thin oxide has to be grown in order to obtain good passivation across the entire wafer surface. To achieve this and still be able to make a good contact, it is required that the oxide layer is thin (< 20 Å) as mentioned in Section 2.5.2. Growing such a thin oxide is by no means an easy process since it is difficult to create an oxide with a low enough leakage current combined with a uniform thickness on the entire wafer area [36]. There are multiple techniques which can be used to grow these oxides, a small overview of the different ways and their pros and cons will be discussed. The four techniques used in this work are a wet chemically grown oxide in a HNO_3 bath called ChemOx, a wet chemically grown oxide in a bath of ozonated water (O_3), an oxide grown in a dry ozone atmosphere under an UV excimer (UV/O_3) and finally a thermally grown oxide in a furnace under a mixed O_2/N_2 atmosphere.

The ChemOx oxide is grown in boiling 68 wt% nitric acid at 110 ° C. To obtain an oxide with a thickness of approximately 14 Å, the wafers are submerged in the HNO_3 solution for approximately 10 minutes, after this the thickness of the oxide does not further increase since the oxidation is a self limiting process. One of the big benefits of growing a wet-chemical oxide is the relatively low processing temperature, which results in a very homogeneous oxide. A thorough explanation of this oxide growth method can be found in ref. [61].

The O_3 oxide can be either grown in a wet or in a dry environment. During the wet oxidation process, O_3 is dissolved in de-ionized water at a temperature of around 45 °C for 10 minutes with a concentration of around 40 ppm, the process is a self-limiting process [62]. The resulting oxide shows high homogeneity and is very applicable to textured surfaces since the growth rate is independent on the crystal orientation, in contrary to some other growth methods [63]. Increasing the pH of the solution or increasing the temperature has a negative effect on the ozone concentration and thus on the growth rate of the oxide.

The other way to grow an oxide with ogyxen radicals as an oxidant is through ozone generation by UV radiation. The photochemical reaction occurs under the absorption of UV radiation with a wavelength of 185 nm. This radiation, which can be generated by either a low pressure mercury lamps or excimer systems, leads to dissociation of molecular oxygen with the production of ozone as a consequence [64], this ozone then falls apart in atomic oxygen and oxygen radicals, which react with the silicon on the surface of the wafer resulting in a SiO_x oxide layer. By varying the distance between the sample and the source and the exposure time, the oxide density and thickness can be varied.

Finally, there is the possibility to grow a thin oxide layer using thermal oxidation. During this process, the wafers are placed in a furnace and subjected to an elevated temperature (typically in the range of 600-700 ° C, whilst feeding a certain gas mixture into the tube (typically nitrogen, argon, and oxygen). The elevated temperature accelerates the oxide growth and by varying the flow rates of the gases the density of the oxide can be altered. But when creating a ultra-thin oxide required for the TOPCon structures it was observed that the uniformity across the wafer is usually less for a thermally grown oxide than for the oxides grown using wet-chemical methods [65]. However, there are cases known in literature where thermally grown oxide with a low defect density and the required thickness have been produced [38].

3.3. PECVD of doped Si layers

PECVD is the chosen deposition technique for depositing the TOPCon layers. PECVD is a suitable technique for depositing the thin highly-doped layers used in these carrier-selective contacts, since it produces a highly

uniform layer and it is rather easy to adjust the layer properties as desired. Another advantage of PECVD compared to atmospheric or low pressure chemical vapour depositions, is the lower processing temperature. This significantly decreases the thermal budget necessary to produce the samples and it also circumvents the problem of alteration of the substrate due to the high processing temperature which might occur.

During PECVD depositions a certain gas mixture is brought in contact with either a RF or a microwave source. This source creates a rapidly changing electric field between an anode and a cathode. The electrons in the gas molecules can easily follow this fast changing electric field since they are very light. The atom cores, however, have more inertia and cannot follow the switching electric field. This causes some of the electrons to be separated from the atoms, leaving behind ions. These liberated electrons can collide with another atom, liberating another electron in the process, thus, creating more ions. During processing, there is an equilibrium of generation and recombination of these ions, also called radicals.

In the PECVD reactor used during these experiments, an AK400M produced by the company Roth & Rau, the walls of the processing chamber are grounded, whilst the substrate plate which holds the samples is capacitively coupled to the RF generator. This means that if electrons hit the chamber's walls, they are transported away. But if they hit the plate, a negative charge is transferres to the substrate plate. This negatively charged plate is more likely to attract positively charged ions. This focusses the ion flow towards the sample and this ion bombardement can break up weak bonds like the Si-H bonds. This enhances growth of the silicon layer and leads to a denser film [66]. Once the radicals make it to the sample they are absorbed and become part of the deposited layer. A schematic representation of the Roth & Rau reactor can be found in Figure 3.1.

As is evident from Figure 3.1, this reactor is a two chamber system. The load lock is necessary to maintain a good vacuum in the reactor chamber and without it a lot of humidity would gather in the processing chamber each time samples are loaded in the reactor. After evacuation of the load lock to an acceptable pressure ($5{\cdot}10^{-2}$ mbar) the substrate plate with the samples are driven into the reactor chamber after which the substrate plate is heated to the desired temperature (usually the temperature is set in the range of 400-500 ° C). After this temperature is reached, the process pressure is set (typically 0.3 mbar) and a five minute preheat is started to ensure a stable substrate temperature. After the preheat the process gases are fed into the chamber, the plasma is ignited and the deposition is completed.

The gases used during a PECVD process varied depending on the composition of the layer and whether

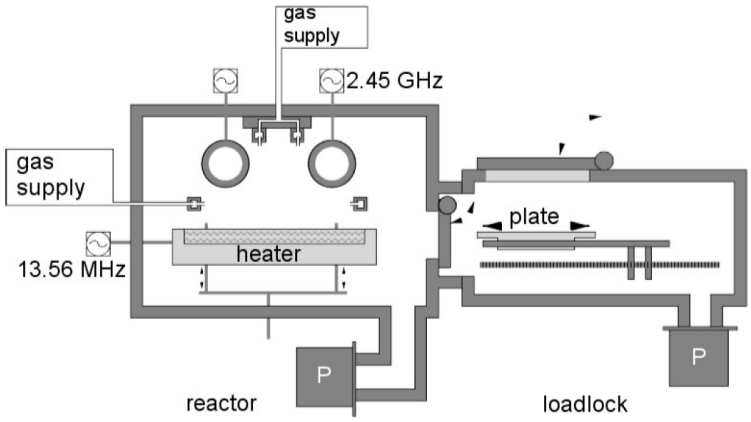

Figure 3.1: Schematic representation of Roth & Rau PECVD reactor used in the experiments. Picture adopted from [66]

the layer was to be n-type or p-type. A short overview of the different gases and a short summary of their purpose can be found in Table 3.1. It can be seen that the dopant sources are either delivered by phosphine

Table 3.1: Overview of the gases used during the PECVD depositions and a short description of their purpose

Gas	**function n-TOPCon**	**function p-TOPCon**
SiH_4	Silicon, Si-C layers	Silicon, Si-C layers
CH_4	Carbon in Si-C layer	Carbon in Si-C layer
PH_3	Dopant gas	
B_2H_6		Dopant gas
H_2	Limit H-content of layer	LimitH-content of layer

gas for n-type layers or diborane gas for p-type layers. The hydrogen is not a supplier of atoms but is used to dilute both the phosphine and the diborane gases. Furthermore, changing the hydrogen flow influences the amount of hydrogen that is incorperated in the deposited layer, an increased H_2 flow leads to a decreased hydrogen incorporation into the layer as well as a decreased deposition rate [67].

Besides changing the gas flows and the gas flow ratios, the following parameters can be adjusted: substrate temperature, operating pressure and RF power. For each of the variables the effects on the deposition rate and the quality of the film will be discussed. For a more elaborate analysis, the reader is reffered to [67]. The substrate temperature plays an important role in a lot of the kinetics involved in growing the deposited layer, and is thus a very important deposition parameter. Increasing the substrate temperature, decreases the hydrogen content, and disorder of the deposited sheet. The deposition rate is barely affected by the substrate temperature. It can be a little tricky to determine the substrate temperature correctly as it is not directly measured in the AK400M reactor. To be sure about the substrate temperature during deposition, a calibration step is needed.

The operation pressure should be kept above a minimum value to avoid poor film quality. At a too low pressure the film might be damaged by ion bombardment and a higher concentration of SiH_2 and SiH bonds will find their way into the layer. Increasing the pressure too much leads to a shorter mean free path-length which can lead to the formation of powders as a consequence of gas-phase polymerization. These powders can clog the system, thus shutting down the reactor [68]. The hydrogen content of the film is also found to rise with rising pressure [69].

Finally, increasing the RF power increases the deposition rate until the gas flow starts limiting the deposition rate. Another effect of changing the RF power is the type of bonds found in the deposited layer. Decreasing the power lessens the dissociation of SiH_4 and hence a lot of SiH bonds are found. Increasing the RF power decreases the layer quality and since the dissociation of SiH_4 is also increased, there are more SiH_2 bonds found in the film [67].

3.4. High-temperature anneal

After the deposition of the thin dopant rich layers the wafers receive an anneal. This is again done in a furnace under a N_2 atmosphere an an elevated temperature of 800-1000 ° C. This anneal has multiple functions, first it crystallizes the layer which is deposited as amorphous or hydrogenated amorphous silicon. This is beneficial as crystallized silicon has superior electrical and optical properties when compared to amorphous silicon [70]. The high temperature anneal also activates the dopants that are deposited during the PECVD step. The activation is thought to be limited by boron cluster forming and to prevent this from happening a high ramp

up speed is beneficial during the annealing step [71], in the annealing process used during these experiments a ramp up speed of 10 ° K min^{-1} was used. The oxide layer between the bulk and the doped poly-Si layer also changes during the high-temperature anneal. The stoichiometry changes through hydrogen effusion and the integrity of the oxide might be undermined as is observed for the ChemOx oxide.

A third effect that is observed is the increased diffusion of the dopants by the high temperature. This will cause some boron diffusion through the oxide into the bulk silicon material, this results in an inferior passivation and it is thus important to minimize the boron diffusion into the bulk as much as possible. Therefore, it is important to have an oxide layer with a high thermal stability since the oxide also functions as a diffusion barrier.

3.5. Hydrogen passivation

The remote plasma hydrogen passivation (RPHP) is a process where atomic hydrogen is used to passivate defects in the silicon layer in order to improve the passivation of the samples. Atomic hydrogen is chosen over molecular hydrogen because it has a higher mobility in Si and atomic hydrogen is better at passivating dangling bonds, especially in a-Si [72]. A good way to generate atomic hydrogen, is through a hydrogen plasma. Hence remote plasma hydrogen passivation was chosen as the preffered passivation technique. It was first implemented to passivate the defects in low efficiency multi-crystalline silicon solar cells [73]. Most defects are caused by a dangling bond which is caused by an discontinuity in the silicon crystal, especially at the interface of two materials, for example silicon and silicon-oxide, a lot of these defect are present resulting in a higher recombination and thus decreased minority carrier lifetimes. These dangling bonds can bond with a hydrogen atom, which will passivate the defect and decrease recombination.

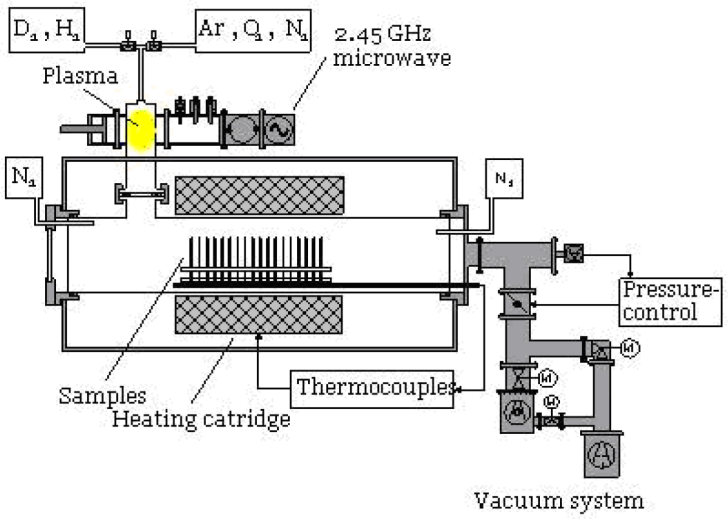

Figure 3.2: Schematic representation of the RPHP processing setup. Picture adopted from [73]

The processing is done in a tube furnace of approximately 2 meters, of which a schematic representation can be found in Figure 3.2. A smaller quartz tube is connected perpendicular to the large tube at around 30 centimeters from the entrance of the tube. In this smaller quartz tube a gas feed of argon, oxygen, and hydrogen are mixed and subjected to microwave radiation. This microwave radiation excites a plasma which forms hydrogen radicals, these radicals are used to passivate the defects on the layer interfaces in the sample. In order to prevent plasma damage, the samples are positioned further down the tube where they are out of reach

of the plasma. Hence the name remote plasma hydrogen passivation. The process occurs at a temperature of 400 ° C and at a pressure of 0.3 mbar.

4

Characterisation techniques

In this chapter the most important characterization techniques used to test the sample performance will be described. The working principle behind the techniques and the physics governing these processes will be treated. In order to keep a logical flow in this chapter the processes will be described in order of occurrence during a normal lifetime sample processing sequence.

4.1. QSSPC

One of the most important characterization methods is the quasi-steady-state photo conductance (QSSPC) technique. This technique measures the lifetime of minority charge carriers in the sample and thereby provides a lot of information. The measurement setup is relatively simple and used a regular flash lamp used in photography (which has a time decay constant of 2.3 ms and an irradiance of up to 1000 suns) and a coil. A great benefit of the QSSPC measurement method is that it is a non-destructive and contactless method. This means that the sample can be measured during the fabrication process without damaging it, allowing tracing of the minority carrier lifetime throughout the fabrication sequence. The wafer is placed on a platform under which the coil is located to measure the photo-conductivity of the wafer. When the light flashes, this light generates excess charge carriers which induce a photocurrent as is described in Equation (4.1).

$$J_{ph} = \frac{\Delta n_{av} q W}{\tau_{eff}} \tag{4.1}$$

In Equation (4.1), Δn_{av} is the average excess minority carrier density, W the wafer thickness and τ_{eff} the effective minority carrier lifetime. Furthermore, the excess photo-conductance is described by Equation (4.2).

$$\sigma_L = q \Delta n_{av} (\mu_n + \mu + p) W \tag{4.2}$$

In Equation (4.2) μ_n and μ_p are the charge carrier mobility of electrons and holes, respectively. Since the mobility of charge carriers in silicon is well documented, it is possible to find Δn_{av} and $(\mu_n + \mu_p)$ that correspond to the measured photo-conductance through an iterative process with available data. This information can be used to extract the minority carrier lifetime. From this information other parameters like iV_{oc} and iFF can be derived as described by Sinton et al. [74]. This is done by combining Equation (4.1) and

Equation (4.2), from which the minority carrier lifetime can be determined as is expressed in Equation (4.3).

$$\tau_{eff} = \frac{\sigma_L}{J_{ph}(\mu_n + \mu_p)} \tag{4.3}$$

The incident irradiation is measured using a calibrated reference cell and from this information the photocurrent is calculated using available data about the calibrated cell. The value of J_{ph} of the measured sample with respect to the reference cell is influenced by parameters like wafer thickness, material resistance and doping of the wafer bulk, which can be changed in the software.

From this minority carrier lifetime the iV_{oc} value can be determined using Equation (4.4).

$$iV_{oc} = \frac{kT}{q} ln\Big(\frac{\Delta n[N_A + \Delta p]}{{n_i}^2}\Big) \tag{4.4}$$

In Equation (4.4), N_A is the dopant density and Δn and Δp the photo-generated electron and hole density, respectively.

Furthermore, the saturation current density J_0 can be determined using the QSSPC data. This is done using the method described first by Kane and Swanson [75]. During this extraction method, the saturation current is described as follows:

$$J_0 = S\frac{q n_{i,eff}^2}{N_{dop} + \Delta n}. \tag{4.5}$$

In this equation, S is the effective surface recombination velocity (SRV) and Δn the injection density.his equation is then differentiated with respect to Δn. The effective SRV is given by the following equation:

$$S = \frac{W}{2\tau_s}. \tag{4.6}$$

Here, τ_s is the surface lifetime defined as follows:

$$\frac{1}{\tau_s} = \frac{1}{\tau_{eff}} - \frac{1}{\tau_{intr}} - \frac{1}{\tau_{SRH}}. \tag{4.7}$$

τ_{eff} is the effective minority lifetime, τ_{intr} accounts for the radiative and Auger recombination, and τ_{SRH} accounts for the SRH recombination. Implementing these expressions in Equation (4.5) and deriving with respect to Δn leads to the following expression:

$$J_0 = S\frac{qW}{2}\frac{d}{d\Delta n}\Big(\frac{n_{i,eff}^2}{\tau_s - \frac{W^2}{D\pi^2}}\Big) \tag{4.8}$$

In the method developed by Kane and Swanson the SRH recombination was assumed to be independent of the injection. This was later improved by Kimmerle et al. by taking into account the injection dependence of the SRH recombination [76].

4.2. Spectroscopic ellipsometry

Spectroscopic ellipsometry (SE) is an optical measurement technique utilized in order to check the thickness and the optical properties of a layer deposited on the bulk material, for example after a PECVD process. Besides the thickness of all the sublayers, more information like the optical properties and the band gap of the deposited layer can be determined. The way SE works is through a change in polarization of the light when it is reflected from the sample. During an ellipsometry measurement, one starts with light that is circularly polarized. This means that the beam consists of equally parallel polarized and perpendicular polarized light. For crystals with a cubic structure, or an amorphous material that is isotropic, the propagation of the differently polarized waves is equal [77]. However, most materials do not consist of cubic crystals. This means

that light waves that travel in the same direction, but with different polarization, experience different optical properties of the material like indices of refraction. This will cause a phase and an intensity difference for both types of linear polarization. This results in light with elliptic polarization instead of circular polarization, from which information about the layer configuration, thickness, optical properties and band gap can be extracted. The propagation of the light with circular polarization is described using a Jones vector:

$$\overrightarrow{E} = \begin{bmatrix} |E_p|e^{i\delta_p} \\ |E_s|e^{i\delta_s} \end{bmatrix}. \tag{4.9}$$

Here, $|E_p|$ is the amplitude of the parallel component, and $|E_s|$ the amplitude of the perpendicular component. Furthermore, δ_p and δ_s are the phase factors of the parallel and the perpendicular component, respectively. After reflection on both the top surface of the sample and at the interfaces of the different layers a reflected Jones vector will contain different phases for the parallel and the perpendicular component as well as a different amplitude. If we define the complex amplitudes for both the incident and the reflected beam we can easily derive the Fresnel reflection coefficients:

$$r_s = \frac{E_{rs}}{E_{is}} = tan(\psi_s)e^{i\Delta_s} \tag{4.10}$$

$$r_p = \frac{E_{rp}}{E_{ip}} = tan(\psi_p)e^{i\Delta_p}, \tag{4.11}$$

$$\tag{4.12}$$

where ψ is the ratio for the reflected and incident field magnitudes and Δ the phase change. From these reflection coefficients the ratio can be determined:

$$\rho = \frac{r_p}{r_s} = \frac{tan(\psi_p)}{tan(\psi_s)}e^{(\Delta_p - \Delta_s)} = tan(\psi)e^{\Delta}. \tag{4.13}$$

Of course with multiple interfaces where both reflection and transmission take place these equations become more complicated, although in the end the result is similar in the form of 2 angles. Excellent elaboration on the topic can be found in [77]. These measurements can be done for different wavelengths resulting in different angles for each wavelengths due to the changing optical properties of the material with changing wavelength. From this data properties about the sample can be extracted. In order to extract this information one has to have a rough idea what the sample consists of, with the help of a model the experimental data is roughly reproduced after which a fitting process optimizes the parameters which are to be fitted, thus providing sample information. Since the fitting procedure is a purely mathematical process, it is of the utmost importance to check the results for physical validity[77].

In this thesis, the thickness of tunnel oxides was measured using spectroscopic ellipsometry. Since these oxides have a thickness in the sub-nanometer range, three methods were developed for determining the oxide thickness as accurate as possible. Since each wafer has a surface roughness it is important to eliminate the influence of this surface roughness on the measurement. To achieve this, one wafer is cleaned using the standard cleaning procedure, and after the HF dip transported directly to the SE for a measurement, minimizing the interference of a natively grown oxide with the measurement. Thereafter the oxidized wafers are measured. The first method to obtain an accurate thickness measurement, determines the surface roughness on the cleaned reference wafer, and subtracts this thickness from the oxide thickness at each of the oxidized wafers in order to obtain the true oxide thickness, this method will hereafter be indicated with the

S_{rough} method. Another method uses a material model from the ellipsometer which describes the behavior of interfacial SiO_2. This model is more suitable for describing tunnel oxides than standard SiO_2 since the stochiometry is a better match. This model was first developed by Herzinger et al [78] and will hereafter be indicated by the I_{jaw} method. The final method used, determines the optical constants of the wafer with the native oxide for the cleaned reference cell, and used this as a substrate in the model. In this way only the additional oxide thickness is taken into account for the oxidized wafers.

4.3. ECV profiling

Electrochemical capacitance-voltage (ECV) measurements are used to determine the doping profile in the wafer. This measurement technique enables high resolution profiling of shallow dopant profiles. The technique combines a traditional capacitance-voltage measurement with a chemical etching step in order to analyze the dopant concentration deeper in the sample. This measurement setup was first introduced by Ambridge et al. [79]. It made the measurement of a dopant concentration profile a lot easier since both processes can take place in the same electrochemical cell. A schematic representation of the measurement set-up can be found in Section 4.3.

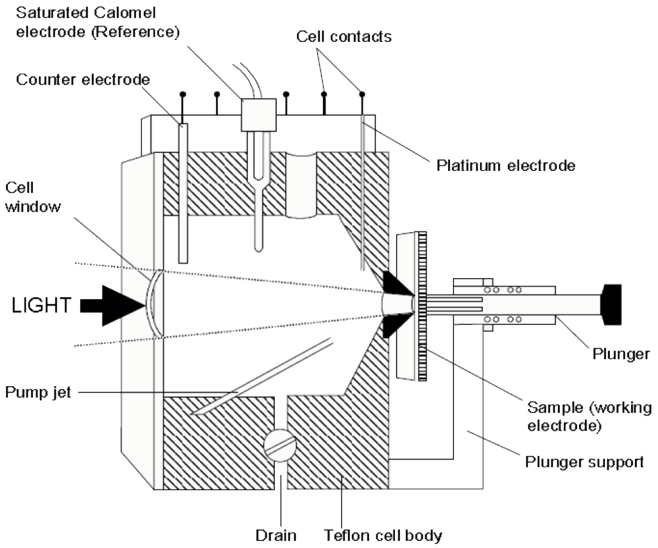

Figure 4.1: A schematic representation of the electrochemical cell from an ECV profiler. Picture taken from [80].

The disadvantage of this method is that it is destructive to the sample. In the following section the capacitance-voltage profiling will be described following the explanation of [81] for n-type material with dopant densities N_D, of course an analogous derivation can be made for p-type material.

Figure 4.2 shows a Schottky barrier for a n-type substrate. During an ECV measurement, the metal layer is replaced by an etchant and a negative bias voltage is applied to put the semiconductor in depletion mode. The capacitance of such a depletion layer Schottky contact is described by Equation (4.14) and is derived in [79].

$$C = \sqrt{\frac{qn\epsilon_s}{2\Psi}}A \tag{4.14}$$

In this equation q is the elementary charge, n the net donor concentration,Ψ the surface potential and A the area of the semiconductor that is in contact with the etchant. This equation can be rewritten to yield the

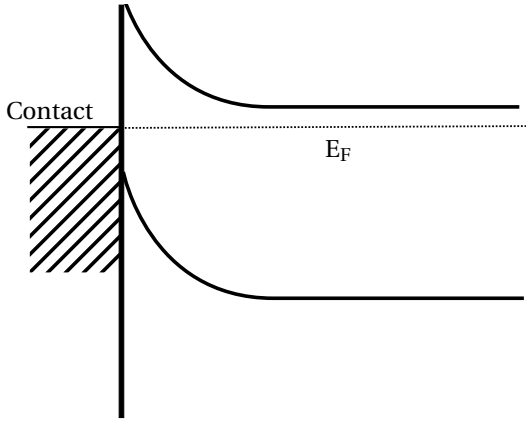

Figure 4.2: Band diagram of an n-type substrate in a Schottky contact with a metal.

following equation:

$$\frac{1}{C^2} = \frac{2(V - V_{FB})}{qn\epsilon_s A^2} \tag{4.15}$$

where V the bias potential that is applied, V_{FB} is the flat band potential. This equation can be rewritten to isolate the dopant concentration n which results in Equation (4.16).

$$n = \frac{2}{q\epsilon_s A^2 \frac{d(1/C^2)}{dV}} \tag{4.16}$$

The depletion width is calculated using the simple expression for plate capacitors and the capacitance value C

$$W_d = \frac{\epsilon_s A}{C} \tag{4.17}$$

During a measurement, the sample is pressed against the sealing ring and the electro-chemical cell is filled with echant, in our case 0.1 molar ammonium bifluoride (ABF). A negative bias is applied between the platinum electrode positioned close to the sample's surface with respect to the saturated calomel electrode to bring the sample into depletion mode as mentioned before. This negative DC bias is then slowly varied with a stepsize ΔV of 30 mV. For each DC bias value the capacitance is measured by superimposing an AC voltage of 25 mV on top of the DC bias. This AC signal is used to measure the admittance, which is then used to determine the following measurement variables: capacitance C, series resistance R_S and the parallel conductance G.

The relationship between these three variables and the admittance can be found in Equation (4.18) and an equivalent circuit to describe the electrochemical cell better can be found in Figure 4.3.

$$\frac{1}{Y} = R_S + \frac{1}{G + j\omega C} \tag{4.18}$$

The capacitance is calculated from the admittance using the following equation:

$$C = \frac{|Y|^2}{\ln(Y)\omega\left(1 + \frac{{\omega_0}^2}{\omega^2}\right)} \tag{4.19}$$

where $\omega_0 = \omega \frac{\mathrm{RE}(Y) - R_S|Y|^2}{\ln(Y)}$. Furthermore, the parallel capacitance is calculated by:

$$G = \omega_0 C. \tag{4.20}$$

By measuring the admittance at two different frequencies ω the mean value and standard deviation of the capacitance and parallel capacitance can be calculated. This is done for several values of the DC bias voltage,

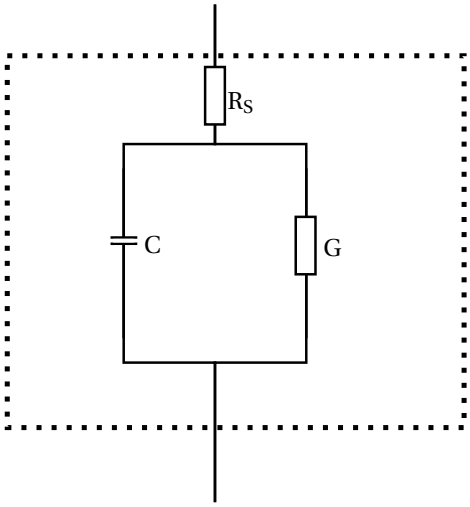

Figure 4.3: Schematical drawing of the equivalent circuit describing the electrochemical cell.

where the mode of the sample is varied between deeper and less deep depletion. Thereafter, the slope of this $\frac{1}{C^2}$ curve is used to determine the dopant concentration. Finally, the current depth is accurately determined by adding the etched depth to the depletion depth according to the following equation found in [82].

$$x = W + \frac{M}{zF\rho A}\int_0^t I_{dis}\,dt \tag{4.21}$$

In Equation (4.21), M is the molecular weight of the semiconductor material, z the number of charge carriers needed to dissolve one semiconductor atom, F Faraday constant, ρ the semiconductor density and A the area of the semiconductor in contact with the etchant. During the measurement the current is integrated electronically to obtain the current depth in the semiconductor material.

4.4. EDNA Analysis

EDNA is a freeware tool developed by McIntosh et al. [83] and is designed to calculate the recombination in heavily doped silicon regions and their surfaces. Thus, it is typically used to model emitter and back-surface field regions of a conventional silicon solar cell. In this thesis it is used to determine effective SRV of the passivating contact which combines both recombination at the Si/SiO_x interface as well as in the TOPCon layer. Hence, it is possible to isolate the effect of different tunnel oxides on the surface passivation quality.

The benefit of this effective surface recombination S_{eff} value is that it combines different surface parameters like interface state density, capture cross sections, and surface charge into one parameter which can be compared easily between different samples. The drawback of this method is that it becomes more difficult to understand the physical principles that govern the changes in the effective surface recombination velocity [84]. The recombination current density value obtained by lifetime measurement as described in Section 4.1 is used as a fitting parameter in combination with the dopant concentration profile obtained with ECV measurements as described in Section 4.3.

EDNA uses the dopant concentration profile and a given value for the effective SRV to calculate an emitter recombination current density. This process takes place as follows: First the sheet resistance of the silicon layer corresponding to the dopant concentration profile is calculated. This is done using the following equation:

$$\rho_{sq} = \frac{1}{q\int_0^z \mu_{maj}(z)N(z)dz} \tag{4.22}$$

where μ_{maj} is the majority carrier mobility which is described by a model developed by Klaassen et al. [85] and $N(z)$, the net ionized doping concentration which is determined from the dopant concentration profile and the base dopant concentration of the wafer, here complete ionization is assumed.

Secondly, the effective intrinsic carrier concentration $n_{i,eff}$ is calculated as well as the energies of the conduction and the valence band and the Fermi energies. During these calculations a model developed by Schenk et al. is used to accurately describe bandgap narrowing [86]. Finally, the emitter saturation current density is determined using the calculated parameters and models for the radiative, Auger and SRH recombination. For the Auger recombination, the model developed by Richter et al. was used [15]. For the SRH recombination, the S_{eff} value was varied and the corresponding J_0 value was compared to the value which was obtained during the saturation current extraction method as developed by Kimmerle et al. [76]. By sweeping the S_{eff} value over a wide range, the influence of the recombination on the passivation of the samples was examined.

4.5. TLM measurement of contact resistivity

Another important property of the samples that has to be determined is the contact resistivity. The specific contact resistivity $\rho_c(\Omega cm^2)$ is not a very well defined parameter as it not only consists of the resistivity of the metal/semiconductor interface, but also part of the metal layer which lies directly on top of that interface and the layer of semiconductor material directly below. Since it is impossible to accurately extract the pure resistance of the interface, the term specific contact resistivity will be used from now on [82]. If the contact resistivity is too high this implies it is not possible to achieve a good contact between the doped layer and the metal, thus resulting in a high series resistance and as a consequence, losses in the FF value. A way to determine the contact resistivity is through transfer length method (TLM). The transfer length method uses a row of either rectangular or circular contacts on a semiconductor surface. The TLM methods completely describes the contacts by giving information about the sheet resistance, the contact resistance and the specific contact resistivity. The two measurement structures used in this work can be seen in Figure 4.4

(a) Circular TLM structures

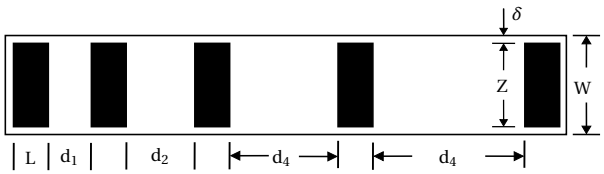

(b) Linear TLM structures

Figure 4.4: Overview of the two TLM structures used to determine the specific contact resistivity. (image recreated from an example in [82].)

First the linear TLM structure from Figure 4.4b will be discussed and thereafter the circular structures

from Figure 4.4a. The derivation for the linear transfer length method was first described by Shockley [87]. It is assumed during these measurements that the metallized pad with L is larger than the transfer length L_T. The transfer length is defined as distance over which the voltage drops by a factor $\frac{1}{e}$. The transfer length is described by the following equation:

$$L_T = \sqrt{\frac{\rho_c}{R_{sh}}}, \tag{4.23}$$

where L_T is the transfer length, ρ_c the contact resistivity and $R_s h$ the sheet resistance. If this assumption is valid the relationship between the contact resistance and the contact resistivity is given by:

$$R_c = \frac{\rho_c}{LZ}, \tag{4.24}$$

where R_c is the contact resistance, L is the metal contact length and Z the height. The total resistance between any of the two contacts in Figure 4.4b is given by:

$$R_T = \frac{R_{sh} d}{Z} + 2R_c, \tag{4.25}$$

where d is the distance between the contacts. Under the assumption that $L \geq 1.5 L_T$ and using Equation (4.24), Equation (4.25) becomes:

$$R_T = \frac{R_{sh} d}{Z}(d + 2L_T) \tag{4.26}$$

For all of the pads the resistance can be measured by forcing a known current from one metal contact to the other and measure the potential difference across the two contacts. The measurement is conducted using a four point probe technique, where two contacts are used for the current flow and two more contacts for the voltage measurement. This technique has the advantage that resistance from the cabling and other measurement components cancels out, thus increasing the measurement accuracy. The total resistance can then be plotted over distance; from this plot all the information about the contact can be derived. The slope of the curve gives the sheet resistance according to the following relationship.

$$\frac{\Delta R_T}{\Delta d} = \frac{R_{sheet}}{Z} \tag{4.27}$$

Furthermore, the abscissa equals twice the contact resistance $d = 0$, $R_t = 2R_c$. Where the curve intersects the x-axis corresponds to twice the transfer length $-d = 2L_T$. From this information the specific contact resistivity is derived using Equation (4.24). An exemplary plot of TLM data can be found in Figure 4.5

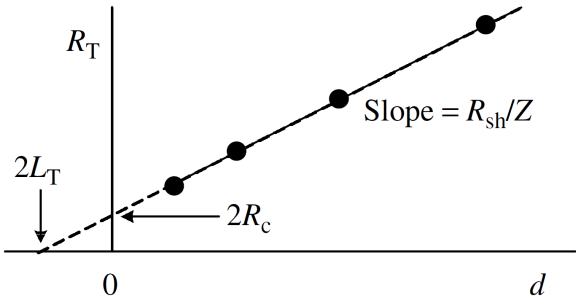

Figure 4.5: Exemplary plot of TLM data with the possibilites to extract data shown. Picture adopted from [82].

A problem with the linear structures occurs when the sample width W is larger than the metal contacts. It is known from experiments that the contact resistivity is overestimated for $\delta \neq 0$. In order to circumvent

this problem it is possible to perform TLM measurements on circular structures like the ones in Figure 4.4a. The derivation of the contact resistivity is analogous to the one for linear structures. We again start with the equation for the total resistance:

$$R_T = \frac{R_{sh}}{2\pi L}(d + 2L_T)C \tag{4.28}$$

with:

$$C = \frac{L}{d} ln\left(1 + \frac{d}{L}\right) \tag{4.29}$$

as one can see the contact height has been replaced by the contact circumference and a correction factor C has been added to correct the total resistance of the circular structure. This is especially important as the gap d becomes large with respect to the contact radius L. Besides these minor adjustments the rest of the derivation is completely analogous to the one for linear contacts. A further complication when determining the specific contact resistivity is the neglect of a current flow through the wafer bulk. Since a traditional TLM measurement only assumes current flow through the emitter, current flow through the bulk can cause an overestimation of the specific contact resistivity. A description on how to account for these effects can be found in [88], although this method was found to still overestimate the specific contact resistivity values.

The best results are obtained by simulating the contacts in Quokka, a simulation program developed by Fell et al. [89]. Picking initial values for ρ_c and simulating the TLM structures allows one to iterate and optimize the ρ_c and R_{sheet} values until a good fit is obtained. At this moment, this process is very time consuming, making it practically impossible to fit large data sets. Since for this thesis it is more important that the specific contact resistivity values stay below the limit where FF losses start to occur, it is sufficient to obtain the upper boundary value of the contact resistivity. Hence, circular TLM measurements without bulk corrections was chosen as the measurement method.

5

Development and optimization of p-type passivating contacts

In this chapter the important experiments for optimizing the boron doped TOPCon layer will be discussed and analysed. The goal of this chapter is to create insight into the functioning of these type of passivating contacts and ultimately increase the passivation. In the first experiment the status quo is reproduced to check the fabrication sequence functions as expected. In the follow-up experiment a thermally grown tunnel oxide is introduced and optimized. The third experiments compares the passivation quality of the thermally grown tunnel oxide with competing tunnel oxides and in the final two experiments the TOPCon layer itself is optimized in terms of stack configuration.

5.1. UV/O_3 and O_3 tunnel oxides

The first experiment was designed to recreate the results obtained thus far with a boron doped TOPCon configuration. Until now the best values for a p-TOPCon configuration were obtained using an UV/O_3 oxide and an annealing temperature of 850 ° C. With this configuration an iV_{oc} of 704 mV was obtained in combination with an iFF value of 85.03 % [90]. This is already a promising result but it is still far behind the results for n-TOPCon which are currently at an iV_{oc} value of 742 mV and an iFF value of 86.3 %. In order to see if there the fabrication process still functioned at the same level, the status quo for p-TOPCon was reproduced.

5.1.1. Experimental details

In this experiment two different tunnel oxides were tested. The UV/O_3 oxide, which produced the highest passivation quality thus far for p-TOPCon, was tested against the wet-chemically grown O_3 oxide. The O_3 oxide has provided excellent passivation results for n-TOPCon which might be transferred to the p-TOPCon contact. Moreover, the doping concentration of the poly-Si layer as well as the annealing temperature (T_{anneal}) was varied.There were three variations for the gas flow ratio, which can be found in Table 5.1. For each ratio, the samples were annealed at four different high temperature anneal processes, which can be found in Table 5.2.

The impact of the annealing temperature as well as the annealing time was investigated using the four

Table 5.1: Overview of the different gas flow variations used in this experiment

B_2H_6/H_2 gas flow [sccm]	25/75	50/50	75/25

Table 5.2: Overview of the four different annealing processes used in this experiment.

Annealing process	1	2	3	4
T_{anneal} [°C]	850	875	900	900
Annealing time [min]	10	10	10	30

different annealing processes. Since a new furnace was implemented in the fabrication sequence, it is important to investigate the influence of this new furnace on the passivation quality. As for the doping, it is chosen to make a wide variation to track the optimum value.

The sample configuration fabricated during this experiment is depicted in Figure 5.1. The base material consisted of 10 Ωcm p-type FZ wafers. On the rear side, all samples received a wet-chemically grown O_3 oxide on the with the standard n-TOPCon layer on top as a precursor. After deposition of the n-TOPCon layer, the wafers were cleaned once more to remove any organic or metallic contamination. This ensures cleanliness and thus reproducibility of the samples. The precursor samples then received a front side oxidation with either the UV/O_3 or the O_3 oxide. For the layer configuration the standard p-TOPCon configuration was used. This configuration consists of a 4 nm intrinsic a-Si:H layer, followed by a 10 nm boron doped a-Si:H layer. Finally, a 4 nm SiC capping layer with the same dopant concentration was deposited. The built-up sequence of the stack can also be found in Figure 5.1.

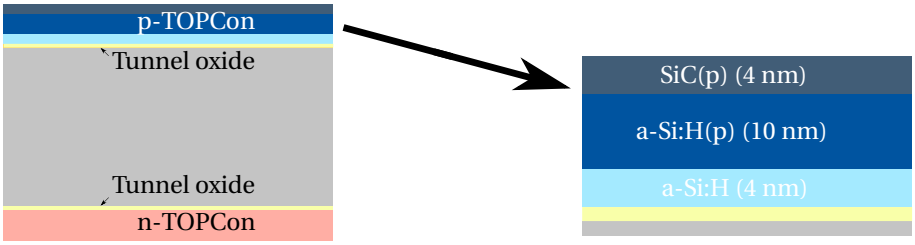

Figure 5.1: Overview of the lifetime samples used in this experiment with the p-TOPCon stack of i-layer, p++-layer and capping layer.

For each oxide, two wafers received the same dopant concentrations during deposition and were then halved. The halves were then annealed at the four different annealing processes. The last step was hydrogen passivation in the RPHP reactor to boost the minority carrier lifetime.

5.1.2. Results and discussion

Using QSSPC measurements of the samples, information about the sheet resistance (R_{sheet}), minority carrier lifetime, implied open-circuit voltage and implied fill factor are obtained. The iV_{oc} and R_{sheet} values are plotted in Figure 5.2a and Figure 5.2b, respectively.

In Figure 5.2 the UV/O_3 oxide is represented with the filled symbols and the O_3 oxide with the open symbols. The n-TOPCon reference cells, which have the O_3 oxide followed by the n-TOPCon layer on both sides, are indicated with the blue open symbols. On the x-axis the annealing processes are plotted and on the y-axis

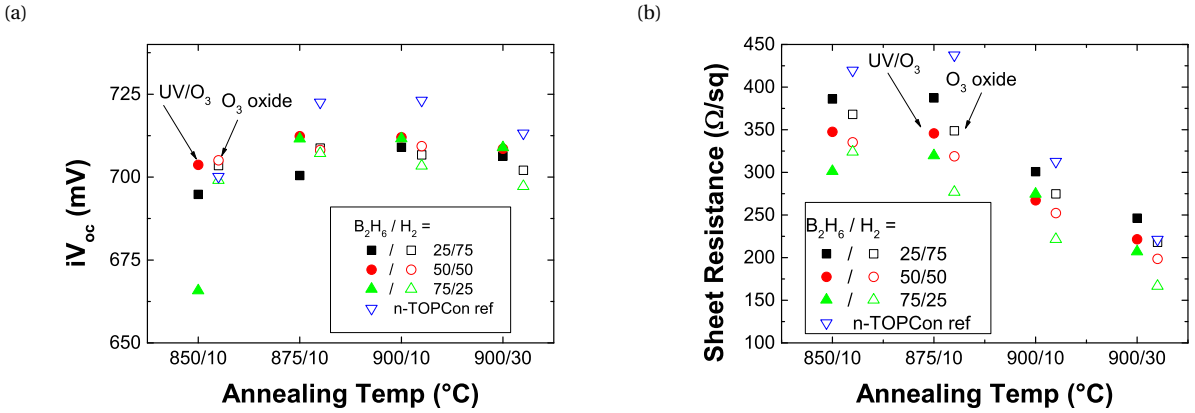

Figure 5.2: Obtained data for iV_{oc} and R_{sheet} values of the the asymmetric lifetime samples.

the open circuit voltage and sheet resistance, respectively. By analyzing the graphs, it can be concluded that the passivation of the p-TOPCon layer was acceptable for both oxides. It should be noted that the iV_{oc} values show the passivation of the entire sample, since the n-TOPCon layer on the back is known to have a excellent passivation, this is clear when looking at the n-TOPCon references fabricated in this experiment. Since the samples were asymmetric, it can be expected that the symmetric p-TOPCon samples will result in slightly lower values.

For the 850 °C anneal, the O_3 oxide gave a slightly better passivation than the UV/O_3 oxide. The n-TOPCon reference had a similar passivation as the O_3 oxide. For the UV/O_3 oxide a relatively large fluctuation of the passivation quality with dopant gas flow ratio was observed for the 850 °C anneal. The best passivation was observed for the medium doped sample, and for the lowly and especially the highly doped sample the passivation was drastically decreased. For the O_3 oxide, this effect was not observed at 850 °C. For the 875 °C anneal, the n-TOPCon reference showed better passivation compared to both the n-TOPCon reference samples annealed at 850 °C and the asymmetric samples annealed at 875 °C. For this annealing temperature, the UV/O_3 oxide resulted in superior passivation when compared to the O_3 oxide, except for the lowly doped sample. The overall passivation quality of both oxides was improved over the 850 °C anneal. For the O_3 oxide samples, the dependence of the passivation quality on the dopant gas concentration is minimal for this annealing process.

The 900 °C anneal with a processing time of 10 minutes resulted in similar passivation quality for the n-TOPcon references. The UV/O_3 oxide again outperformed the O_3 oxide and the lowly doped sample with UV/O_3 oxide now showed superior passivation when compared to the 875 °C anneal. The optimal gas flow ratio for the UV/O_3 oxide seemed to lie at the 50/50 sccm point for both this and the 875 °C anneal. For the O_3 oxide, the sample with medium doping resulted in the best passivation. Both increasing and decreasing the dopant concentration led to inferior iV_{oc} values. Finally, the 900 °C anneal with a processing time of 30 minutes resulted in a decreased passivation for the n-TOPCon reference samples. The samples with the UV/O_3 oxide also showed a slight drop in iV_{oc}, but not to the same extend as the n-TOPCon reference samples. For the O_3 oxide, the reduction in passivation quality was more pronounced. Unfortunately, the medium doped wafer halve with the O_3 oxide was lost in the fabrication process, so no data point is available for this annealing process.

In general, the UV/O_3 seemed to outperform the O_3 oxide for most annealing processes, of which the 900 °C/10 minute anneal resulted in the best passivation quality for the UV/O_3 sample with a B_2H_6/H_2 gas flow

ratio of 50/50 sccm. The UV/O_3 also showed a more consistent passivation quality for higher T_{anneal}.

Figure 5.2b shows two clear trends. First of all, increasing the dopant gas flow decreased the sheet resistance. This trend is independent of the tunnel oxide used since it was observed for both the UV/O_3 and the O_3 oxide. Secondly, increasing the annealing temperature or annealing time also decreases the sheet resistance. When comparing the 850 and the 875 °C anneal, the n-TOPCon reference samples showed a slight increase in the sheet resistance with increasing T_{anneal}. The asymmetric samples with the UV/O_3 oxide showed stable R_{sheet} values and the O_3 oxide a slight decrease in R_{sheet} values. For further increasing T_{anneal}, the sheet resistance dropped for both oxides. The lowest sheet resistance values were found for the 900 °C anneal for 30 minutes. Finally, the O_3 oxide systematically resulted in lower R_{sheet} values than the UV/O_3 oxide.

In order to link the sheet resistance values to dopant concentration in the samples, ECV measurements were conducted on the samples which received the 900 °C/30 minute anneal in order to compare the dopant profiles. The resulting profiles can be found in Figure 5.3. Figure 5.3 shows the boron concentration profiles

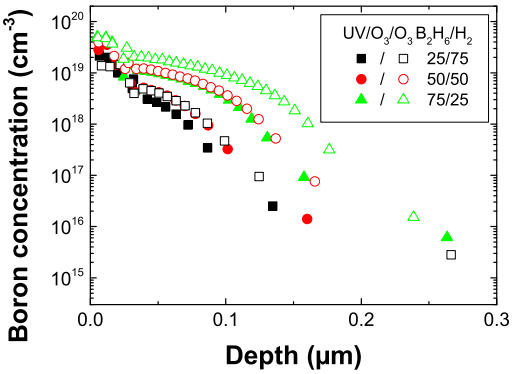

Figure 5.3: Dopant profiles obtained by ECV measurements for different dopant gas flows.

for both oxides at every gas flow ratio. The deepest profile, which also shows the highest surface dopant concentration, was obtained for the O_3 oxide with the highest diboran flow. The UV/O_3 oxide with the same gas flow ratio resulted in a significantly shallower profile. Reducing the diboran flow reduced the profile depth for both the UV/O_3 and the O_3 oxides, as can be seen in Figure 5.3. The shallowest profile was obtained for the UV/O_3 oxide with the lowest diboran flow.

Summarizing the results from this experiment, the UV/O_3 resulted in the best passivation quality for the 900 °C/10 minute anneal at a 50/50 gas flow ratio. The sheet resistance showed a high dependence on both the gas flow ratio and the annealing temperature. A possible explanation is that if more dopant atoms are available, this will increase the boron content in the deposited layer. During the annealing in the furnace, some dopants will diffuse into the bulk material, thus increasing the conductivity and decreasing the resistance in the wafer directly below the tunnel oxide. If more dopant atoms are available in the TOPCon layer, it is likely that a larger number of dopant atoms will also diffuse into the bulk and thus will lead to a lower sheet resistance. Another factor that increased dopant diffusion is the annealing temperature, diffusion increases with temperature, thus is is to be expected that for higher annealing temperatures the dopant diffusion would increase leading to lower sheet resistances. Finally, the O_3 oxide showed a systematically lower R_{sheet} value than the UV/O_3 oxide. This implies that the UV/O_3 oxide was a better diffusion barrier than the O_3 oxide. This was confirmed by the shallower ECV profiles for the UV/O_3 oxide which can be seen in Figure 5.3. If the data from the iV_{oc} and the R_{sheet} values are combined, it can be concluded that the tunnel oxide has a significant

effect on both the boron diffusion and the passivation quality. The difference in passivation quality might be caused by different recombination velocities for the different oxides.

5.2. Thermally grown tunnel oxide

From the previous experiment it was observed that the status quo can be reproduced without major issues. The passivation optimal for a 900 ° anneal and the UV/O_3 oxide that proved a better diffusion barrier for boron resulted in superior passivation. This implies that it is important that the oxide is a good diffusion barrier for boron and it succesfully passivates the surface. Or in other words, shows low recombination. Hence it is important to have an oxide which is dense and remains stable at the higher annealing temperatures which are typically used in the fabrication process of TOPCon cells [45]. From literature it is known that a thermally grown oxide shows excellent stability at high temperatures. Hence, it was chosen to conduct an experiment where a thermally grown oxide was incorporated into the p-TOPCon lifetime sample fabrication process.

5.2.1. Experimental details

The lifetime samples produced to investigate the passivation of a p-TOPCon layer with a thermally grown oxide were fabricated symmetrically to exclude any positive effect on the lifetime properties from the n-TOPCon layer. The oxide was grown on the n-type Ωcm FZ wafer in a Centrotherm furnace at a temperature of 600 °C. The total gas flow through the furnace was 10 standard liter per minute, with three variations of the N_2/O_2 ratio. These gas flow ratios can be found in Table 5.3.

Table 5.3: Gas flow ratio variations for the thermally grown oxide.

Process	**Time [min]**	**N_2 flow [slm]**	**O_2 flow [slm]**
1	10	10	0
2	10	7	3
3	10	4	6
4	20	4	6

After the oxides were grown, the samples were measured using SE to determine the oxide thickness using the interface jaw method described in Section 4.2. Thereafter, the samples received a symmetrical p-TOPCon or n-TOPCon layer in a PECVD process using the optimal configurations obtained during the experiment described in Section 5.1. The n-TOPCon layer was also tested with the thermally grown oxide since solar cells will be fabricated which contain an n-TOPCon layer on the front and a rear-emitter consisting of a p-TOPCon layer. After the TOPCon depositions the samples were halved and received an anneal at either 900 or 1000 °C, these annealing temperatures were chosen since it was expected that the oxide had a good thermal stability as has been stated in previous papers. Finally, the RPHP step was used to passivate defects.

5.2.2. Results and discussion

In Table 5.4 the result of the SE thickness measurements can be found. In Table 5.4 the oxide thickness increased with increasing oxygen flow. Futhermore, increasing the oxidation time further increased oxide thickness. It is remarkable that even under a pure nitrogen gas flow an oxide thickness was measured. It should be noted that the thickness of the oxide is at the limit of what can be resolved using SE. The passivation quality of the different oxides was investigated using QSSPC. In Figure 5.4 the results from the QSSPC measurement

Table 5.4: Thickness of the oxides grown during the four different oxidation processes obtained by spectroscopic ellipsometry measurements.

N_2/O_2 flow [sccm]	**Thickness [nm]**
10/0	1.06-1.07
7/3	1.23-1.27
4/6	1.31-1.37
4/6, 20 min	1.4-1.47

for the p-TOPCon lifetime samples are plotted. Figure 5.4a shows the iV_{oc} values for the four different oxi-

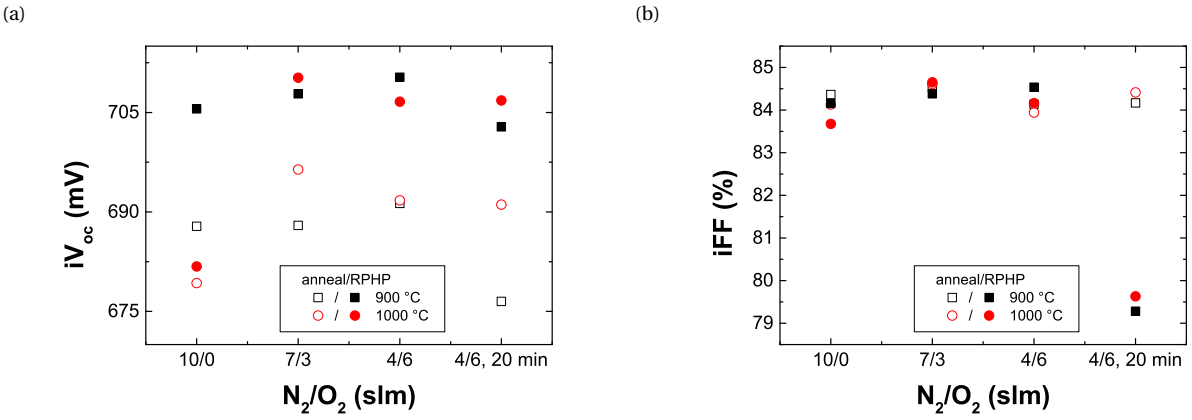

Figure 5.4: Obtained data for iV_{oc} and iFF values of the the p-TOPCon lifetime samples with thermally grown oxide.

dation processes before and after hydrogen passivation. On the x-axis the four different oxidation processes are displayed, and on the vertical axis the iV_{oc} is displayed. In this graph each data point represents one sample. After annealing, the samples which were annealed at 900 °C all showed an iV_{oc} value around 690 mV. The longer oxidized wafer showed a substantially lower iV_{oc} value. For the samples which were annealed at a 1000 °C, the oxide grown under pure nitrogen gas flow showed inferior passivation quality. After RPHP, a significant increase in the iV_{oc} values was observed for all samples, except the sample with the pure N_2 oxide which was annealed at 1000 °C. For the 7/3 gas flow ratio, the 1000 °C anneal resulted in a slightly superior passivation, whereas for the 4/6 gas flow ratio, the 900 °C proved superior. This sample also provided the best passivation with an iV_{oc} value of 710 mV and an iFF value of 84.5 %. Increasing the oxidation time slightly decreased the passivation quality after RPHP.

Figure 5.4b shows the iFF values both before and after RPHP. For the first three oxidation processes, good iFF values in the 84-85 % range were obtained for both annealing temperatures. The hydrogen passivation only had a minor effect on the iFF. The one exception is for the fourth oxidation process, here a stark decrease in the iFF is observed after the RPHP step. This is not a commonly occuring phenomenon as hydrogen passivation usually increases the passivation quality by saturating dangling bonds.

Good passivation was obtained for all oxidation processes, even the one where theoretically no oxygen was present. For this process, the SE measurement also resulted in a nonzero oxide thickness. These results implied that an oxide did grow during this process. This could mean that even though only nitrogen is fed into the furnace, oxygen is still present in the tube at the time of oxidation. It could also imply that a native oxide with a thickness of $\approx$ 1 nm was grown before the samples were exposed to the oxidation process in the

furnace.

The results from the QSSPC measurements conducted on the n-TOPCon samples can be found in Figure 5.5. Figure 5.5a shows that all samples annealed at 900 °C showed similar iV_{oc} values, even the sample

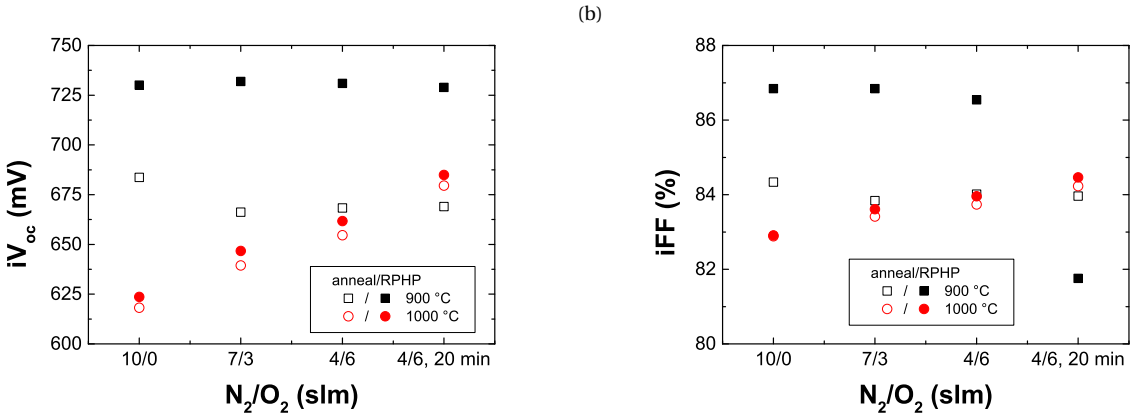

Figure 5.5: Obtained data for iV_{oc} and iFF values of the the n-TOPCon lifetime samples with thermally grown oxide.

which was treated with pure nitrogen. After hydrogen passivation in the RPHP reactor, the iV_{oc} values are drastically increased and all laid above 725 mV, which indicates excellent passivation. The top values being a 732 mV iV_{oc} and a 86.8 % iFF. For the samples which were annealed at 1000 °C a change in the passivation quality can be seen after annealing. The passivation of these samples increased with increasing oxygen flow and increasing oxidation time. After RPHP, the iV_{oc} values were slightly improved, but still far inferior to the samples which were annealed at 900 °C. It is remarkable that the sample which was treated with pure nitrogen shows a similar passivation to the other oxidation methods at the 900 °C. This implies that indeed an oxide is grown with the aid of either remaining oxygen, or through native oxidation.

Figure 5.5b shows that after annealing, the samples which received the 900 °C anneal all had an iFF value of approximately 84 %. After hydrogen passivation an increase of around 3 % in iFF values was observed for the first three oxidation processes, leading to excellent iFF values of 86-87 %. For the sample with the long oxidation time, the RPHP step caused a drop in iFF, which was also observed for the p-TOPCon lifetime samples as can be seen in Figure 5.4b. For the samples annealed at 1000 °C, a gradient in iFF values can be observed. The iFF increased with oxygen gas flow and increasing oxidation time. Like for the iV_{oc} values from Figure 5.5a, the RPHP step had only a slight positive effect on the iFF values.

The thermally grown oxide provided good passivation quality for both p-TOPCon and n-TOPCon, competing with the UV/O_3 oxide for p-TOPCon in terms of iV_{oc} and iFF values. Also for the n-TOPCon samples, excellent passivation quality was achieved. A drop in iFF was observed for the 20 minute oxidation process, but since the sample size is limited there is not enough statistic to conclude there is a trend. The 1000 °C was far below the standard level for n-TOPCon and also the iFF values were lower than normally observed. In order to better understand the decrease in passivation for n-TOPCon at the 1000 °C anneal, ECV profiles were obtained for both the p-TOPCon and the n-TOPCon samples which were annealed at 1000 °C for each of the four oxidation processes. The resulting dopant concentration profiles can be found in Figure 5.6.

Comparing the boron profiles from Figure 5.6a with the phosphorus profiles from Figure 5.6b, two differences stand out. The boron profiles show a sharp decline in the first few nanometers of the profile, up to the location where the tunnel oxide after which a more or less stabilized tail is observed. For the phosphorus profiles, this sharp drop is not observed and a more or less continuous profile is observed for all oxidation pro-

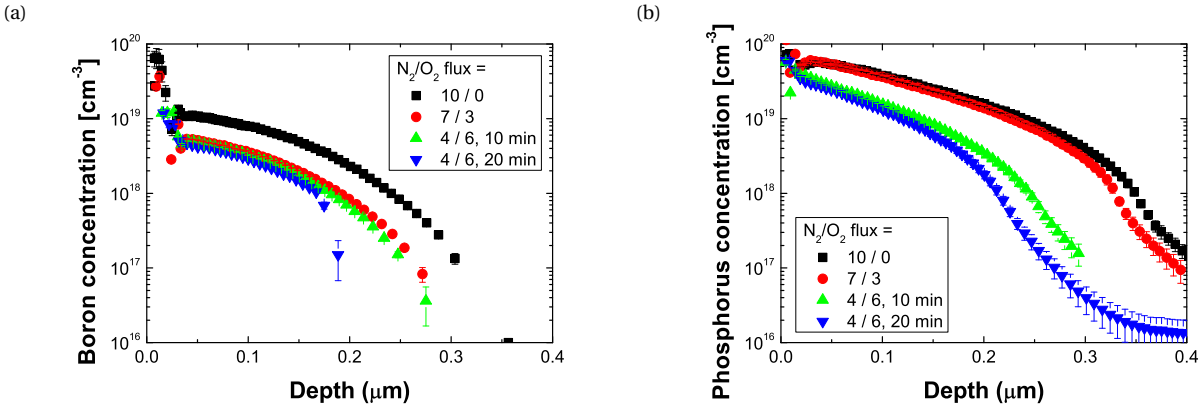

Figure 5.6: Obtained dopant concentration profiles for both the p-TOPCon and the n-TOPCon samples for the four different oxidation processes.

cesses. The phosphorus profiles also have deeper tails into the bulk when compared with the boron profiles. When focusing on Figure 5.6a, it is observed that the presence of oxygen during the oxidation process strongly reduces boron diffusion. There is a significant difference between the sample that was oxidized under a pure nitrogen atmosphere, and the three oxidation processes with oxygen flowing. The amount of oxygen present during the oxidation process seems to only have a slight influence on the profile depth. Prolonging the oxidation time results in a shallower profile and a slightly lower surface dopant concentration. In Figure 5.6b, a slightly different behavior can be observed. For the phosphorus profiles, there is no significant difference between the 10/0 and the 7/3 gas flow ratio oxidation. When the gas flow ratio is changes to 4/6, however, a strong decrease in the profile depth is observed. Further increasing the oxidation time further reduces the profile depth, but only slightly. It is not yet clear what causes this different behavior. It should be noted that there is not a lot of statistic available since only one sample was measured. The wafers underwent the oxidation processes simultaneously, however. A possible interaction of one type of dopant molecules with the oxide could be the cause of this different diffusion behavior, but more statistic is needed.

Summarizing the findings from this experiment, it can be concluded that the thermally grown tunnel oxide is a promising candidate for both the p-TOPCon and the n-TOPCon passivating contacts. For the p-TOPCon contact, a slight improvement of the passivation quality over the UV/O_3 oxide was observed, with the best result being an iV_{oc} value of 710 mV and an iFF value of 84.5 %. For n-TOPCon, excellent passivation was obtained at a 900 °C anneal, with the top values being a 732 mV iV_{oc} and a 86.8 % iFF. For the 1000 °C anneal, a strong decrease in the passivation quality was observed for n-TOPCon, which was not observed for p-TOPCon. When looking at the dopant concentration profiles, it was observed that the n-TOPCon profiles were both deeper and showed no drop in concentration in the poly-Si layer.

Combining all these results, there are several possible causes for the drop in passivation quality for n-TOPCon at a 1000 ° anneal. One possible cause is a break-up of the oxide which occurs with increasing annealing temperature. It is known that for example the ChemOx oxide breaks down at annealing temperatures above 900 °C [39]. If this were the case, however, one would expect the same effect for the p-TOPCon layer at the same annealing temperatures, which was not observed. Another possible cause is that the carbon in the SiC layer from n-TOPCon caused the oxide to deteriorate. This has been reported in literature by researchers at EPFL [91]. The n-TOPCon layer consists entirely of SiC whereas p-TOPCon only has carbon in the 4 nm capping layer on top of the stack. Since these carbon atoms would have to diffuse through 14 nm of carbon-

free material before it could react with the SiO_x layer, this effect should be less pronounced for the p-TOPCon layer. Looking at the ECV profiles in Figure 5.6, it seems as though the barrier in the boron profiles is more pronounced than in the phosphorus profiles. Breakup of the oxide would lead to increased dopant diffusion into the bulk, which would undermine the passivation. Since the diffusion of phosphorus and boron depends on different mechanisms, it is possible that his phenomena is not observed for both TOPCon types [92].

In order to see if the dopant diffusion was the main cause of the drop in passivation quality at the higher annealing temperatures, the doping concentration of the n-TOPCon was varied in an experiment and these samples were annealed at high temperatures of 900-1000 °C. The results of this experiment can be found in Figure 5.7. From Figure 5.7, it can be concluded that for an annealing temperature up until 950 °C, the

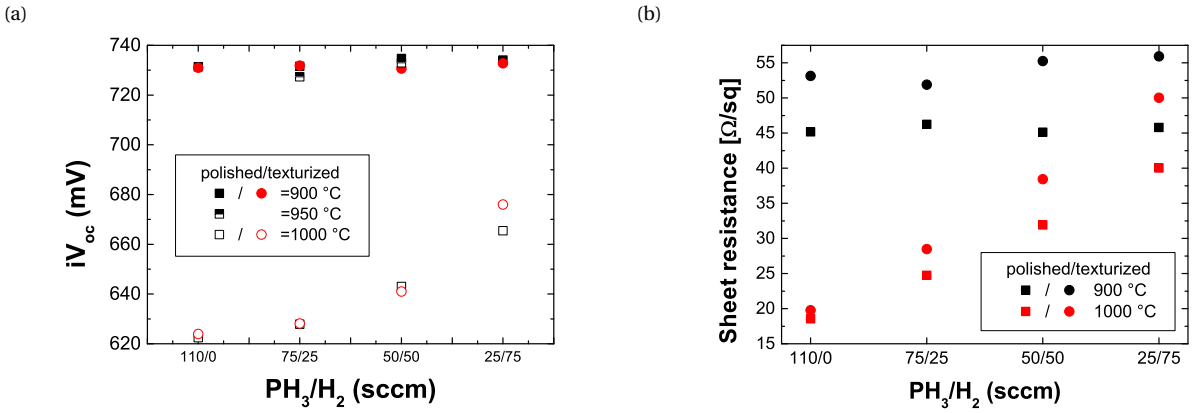

Figure 5.7: Obtained data for iV_{oc} and R_{sheet} values of the the n-TOPCon lifetime samples with varied dopant concentration annealed at high temperatures.

passivation was excellent on both planar and textured surfaces. For an annealing temperature of 1000 °C, this was not the case. Here we can see that lowering the dopant gas concentration did have a positive effect on the passivation, but it did not match the quality obtained at lower temperatures. This even though the sheet resistance approached the same value for a low dopant concentration. Since the sheet resistance correlates with the dopant diffusion into the bulk as was observed in Section 5.1, the dopant diffusion does not seem to be the determining factor which causes the loss of passivation. The ECV profiles indicate no significant diffusion barrier is present for the n-TOPCon at a 1000 °C, where there still is a barrier for the p-TOPCon samples. This hints towards some interaction between components of the n-TOPCon layer and the tunnel oxide at high annealing temperatures.

5.3. Comparison of different oxidation techniques

Since the thermally grown oxide seemed promising it was decided to benchmark it against the three competing oxides: HNO_3, wet-chemically grown O_3 and the UV/O_3 oxide. In this experiment base materials with two different base resistivity values of 1 and 10 Ωcm were chosen. The 1 Ωcm p-type FZ wafer were used to fabricate TLM samples, for which a low base resistivity is very important. As for the 10 Ωcm samples, they were used for J_0 extraction and later on for ECV profiling, this will be discussed more elaborately in Chapter 6. For J_0 determination 10 Ωcm wafers were preferred because the requirement $n_{min} \geq 10 \cdot N_D$ as described in Section 4.1 is fulfilled more easily when the wafer is less heavily doped. This leads to a J_0 extraction which is less prone to error[75].

5.3.1. Experimental details

For each of the oxidation methods two 1 Ωcm and two 10 Ωcm wafers received the same treatment. The four oxidation methods were: UV/O_3, O_3, HNO_3, and the thermally grown tunnel oxide. The oxidation process is explained more thoroughly in Section 3.2. After oxidation, the wafers received a symmetric p-TOPCon layer with the optimal process parameters determined in Section 5.1. After deposition, the wafers were halved and the halves were annealed at a wide temperature range of 850-1000 °C. Finally the defects were passivated using RPHP and the contact resistivity as well as the dopant profiles were measured.

5.3.2. Results and discussion

The minority charge carrier lifetime was measured once after the high temperature anneal and once more after hydrogen passivation. These are indicated by the open and filled symbols, respectively. Since two types of substrates were used two identical samples could be produced, with the only variation being the base resistivity of the substrate. The resulting iV_{oc} can be found in Figure 5.8. For the 850 °C anneal, the best

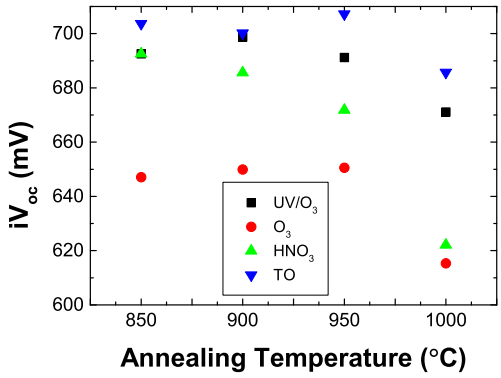

Figure 5.8: iV_{oc} values for the four different oxides for different annealing temperatures. The results are for the 1 Ωcm substrate

passivation is achieved with the thermally grown oxide, followed by the UV/O_3 and the HNO_3 oxides. The lowest iV_{oc} value was obtained with the O_3 oxide. For the 900 °C anneal, the UV/O_3 improved slightly, and the HNO_3 decreased slightly, as well as the TO. The O_3 remained constant at a level inferior to what is normally observed for these temperatures. For the 950 °C anneal, the UV/O_3 and the HNO_3 oxides showed decreased iV_{oc} values. The thermally grown oxide improved, reaching the overall best iV_{oc} value of 707 mV. For the 1000 °C anneal, all oxides showed deteriorated passivation. The thermally grown oxide still performed best, followed by the UV/O_3 oxide. The HNO_3 and O_3 showed far inferior passivation.

The sheet resistance values corresponding to the iV_{oc} values from Figure 5.8 can be found in Figure 5.9.

Analysing Figure 5.9, two clear trends are observed. There was a clear decline in base resistivity when the annealing temperature was increased. This can possibly be explained by a higher dopant diffusion into the crystalline base material. The thermally grown oxide had the highest sheet resistance for all annealing temperatures regardless of the substrate base resistivity, indicating that the thermally grown oxide was the best diffusion barrier. Furthermore, the HNO_3 and the O_3 oxides showed a sharper decline with annealing temperature than the TO and the UV/O_3 oxides. Once again, it seems that oxides that effectively block boron diffusion, also have good passivation quality. In order to cross-check this hypothesis the ECV measurement technique was used to determine the dopant concentration profile in the substrate. The resulting profiles can be found in Figure 5.10. By examining Figure 5.10 it becomes clear that these profiles had a good correla-

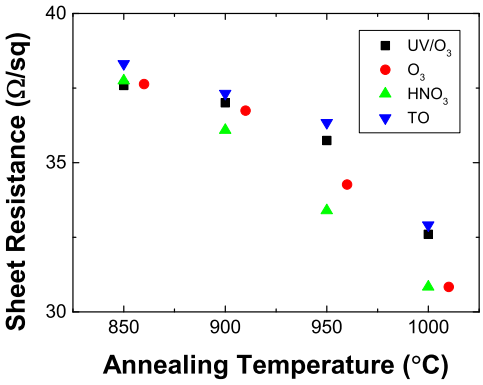

Figure 5.9: R_{sheet} values for both the 1 Ωcm substrate for the four differently grown oxides.

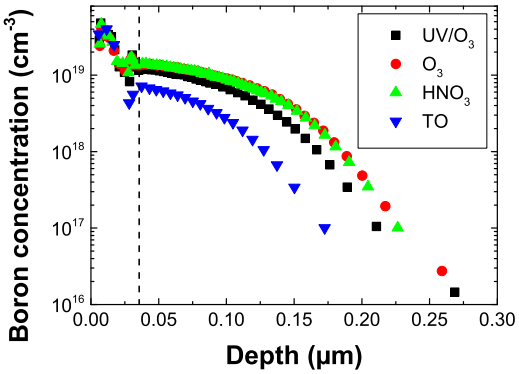

Figure 5.10: Dopant profiles obtained by ECV measurements for the four different oxides at 950 ° C. The dotted line indicates approximated interface between the poly-crystalline Silicon and the bulk material

tion with the sheet resistance values of Figure 5.9. The deepest profile was obtained with the O_3 oxide, which corresponded to the lowest sheet resistance measurement. The thermally grown oxide, which showed superior passivation and the highest sheet resistance, had a significantly shallower profiles as well as the lowest surface dopant carrier concentration. As first mentioned in Section 5.2 there indeed seems to be a positive correlation between passivation quality and shallow dopant profiles.

In order to further analyse and compare the passivation quality of the different oxides, the effective surface recombination velocity was determined with EDNA. The ECV profiles from Figure 5.10 were used for analysis in the EDNA freeware which was developed by McIntosh et al. [83]. For the EDNA analysis, the part of the dopant concentration profile that is of interest is the part in the c-Si bulk, this is the part of the dopant concentration profile on the right side of the dotted line in Figure 5.10. The poly-Si region of the profile was cropped and the profile was loaded into EDNA. An elaborate explanation about the approach EDNA uses to the SRV can be found in Section 4.4. Since the samples annealed at 950 °C showed different profiles for different oxides, it was chosen to track the relationship between the saturation current density J_0 and the effective surface recombination velocity S_{eff}, as was explained in Section 4.4. The resulting curves can be found in Figure 5.11. In this graph, the SRV value which was used as input for EDNA is displayed on the x-axis. The resulting saturation current is displayed on the y-axis. The filled symbols indicate the J_0 values which were obtained from the QSSPC measurements, and their corresponding S_{eff} values. First of all, Figure 5.11 shows

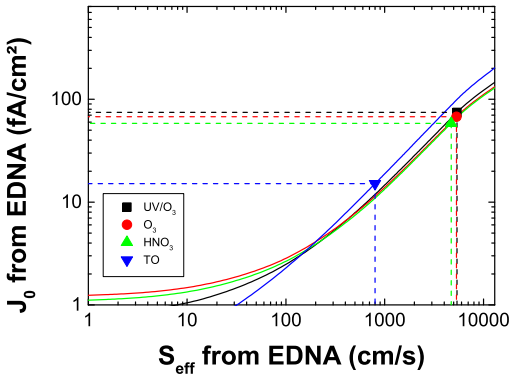

Figure 5.11: Plot of J_0 versus S_{eff} for the samples with different oxides annealed at 950 °C. The open symbols indicate the point on the curve where the saturation current density corresponds to the value obtained during the QSSPC measurement of the sample.

that the thermally grown oxide showed a lower S_{eff} value than the other oxides. Furthermore, for low S_{eff} values, the saturation current density dropped to values below 1 fA/cm^2. This indicates that Auger recombination only plays a minor role in the total recombination current and that the passivation of the samples is limited by SRH recombination. Finally, J_0 increased rapidly with increasing S_{eff}. This indicated that all the dopant profiles are transparent, they do not shield any highly recombination active surfaces.

Since the EDNA analysis provided valuable insight into the sample's passivation quality, the other samples were subjected to the same analysis. The S_{eff} gave an J_0 value which matched the QSSPC analysis was obtained by iteration and the resulting plot of J_0 verses S_{eff} can be found in Figure 5.12. Figure 5.12 showed a

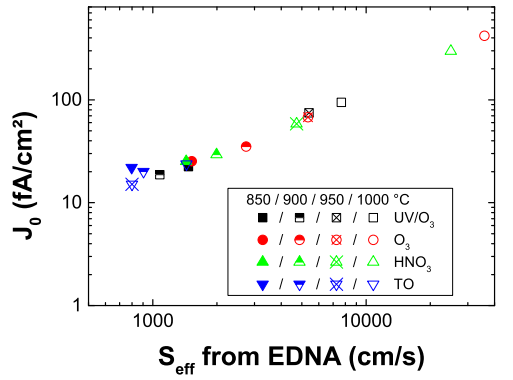

Figure 5.12: Plot of J_0 versus S_{eff} the samples with different oxides at all annealing temperatures

clear correlation between the saturation current density and the effective surface recombination velocity. Increasing the recombination undermines the passivation of the contact which led to an increased saturation current density. Furthermore, it is evident from Figure 5.12 that the thermally grown tunnel oxide consistently showed the best passivation. For all annealing temperature it resulted in a low J_0 and S_{eff} value. The HNO_3 and the O_3 oxides showed the biggest increase in saturation current density with annealing temperature, whereas the UV/O_3 oxide performed slightly better, but was still inferior compared to the thermally grown oxide. If the results from Figure 5.12 are compared with the iV_{oc} values from Figure 5.8, similar trends are observed. The deterioration in passivation can now be linked to an increase in the effective surface recombination velocity, which in it's turn can be linked to the tunnel oxide. Therefore it is important to have a

tunnel oxide with low interface state density and a high thermal stability. Since the recombination was described using the effective surface recombination velocity parameter, it was not possible to determine with certainty which parameter is responsible for the lower S_{eff} value for the thermally grown oxide. From literature it is known that a thermally grown oxide usually shows a lower initial interface state density and thus this is a likely candidate [93]. Although it is not possible to isolate one property of the oxide is essential for good passivation, what does become evident from the EDNA analysis is that the tunnel oxide seems essential for a good passivating contact. Looking at the EDNA analysis, the thermally grown oxide seemed the most suitable candidate thus far.

5.4. Optimization of the p-TOPCon configuration

After the most suitable oxide was determined, and the performance of this oxide was optimized in terms of dopant concentration and annealing temperature, the optimization of the p-TOPCon layer was investigated. This investigation consists of two experiments, in the first section the traditional three layer configuration is varied. Some work has already been done by Guerra [90], but it is not clear if the behaviour of these layers is the same for the denser thermally grown oxide. In the second section, the intrinsic layer will be replaced by an undoped amorphous silicon layer deposited with low pressure chemical vapour deposition technology. One of the possible advantages of this configuration is the lower hydrogen content in the a-Si layer, which possibly reduces the risk of blistering [94].

5.4.1. Varying the p-TOPCon layer configuration

In this experiment the influence of the undoped intrinsic layer as well as the SiC capping layer on the p-TOPCon passivation quality was investigated. Furthermore, the thickness of the a-Si:H(p) layer was varied to investigate the influence of the layer thickness on the passivation quality.

Experimental details

Four different configurations were investigated. A schematic representation of all the configurations used during this investigation can be found in Figure 5.13. In Figure 5.13 configuration I is the standard p-TOPCon

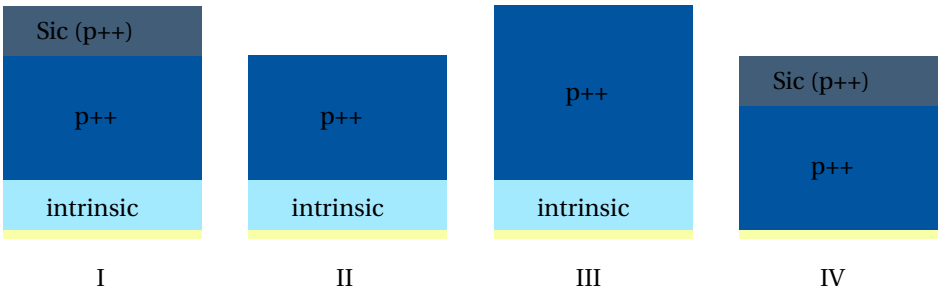

Figure 5.13: Different layer configurations to examine the behaviour of p-TOPCon grown on a thermal oxide.

stack which was used in Section 5.1. In configuration II, the SiC capping layer was removed and in configuration III, the thickness of the a-Si:H(p) layer was increased to 14 nm. Finally, in configuration IV, the intrinsic a-Si:H layer was omitted from the standard p-TOPCon stack. A brief survey of the layer dimensions and dopant concentrations can be found in Table 5.5. The substrate that was used in this experiment were n-type FZ wafers with a base resistivity of 1 Ωcm. These wafers received the thermally grown oxide which provided

Table 5.5: Overview of the configuration parameters used for the p-TOPCon optimization experiment.

Configuration	a-Si:H [nm]	a-Si:H(p) [nm]	SiC(p) [sccm]	B_2H_6 flow [sccm]	H_2 flow [sccm]
I	4	10	4	50	50
II	4	10	-	50	50
III	4	14	-	50	50
IV	-	10	4	50	50

the best passivation in Section 5.2. This oxide was grown at 600 ° C with a N_2/O_2 ratio of 7/3 slm. Thereafter the different layer stacks were deposited during PECVD processing and the samples were annealed at 900 and 950 ° C, respectively. The next step consisted of hydrogen passivation and finally the minority carrier lifetime was investigated using QSSPC.

Results and discussion

The iV_{oc} and iFF values of the different configurations can be found in Figure 5.14. In Figure 5.14a the iV_{oc}

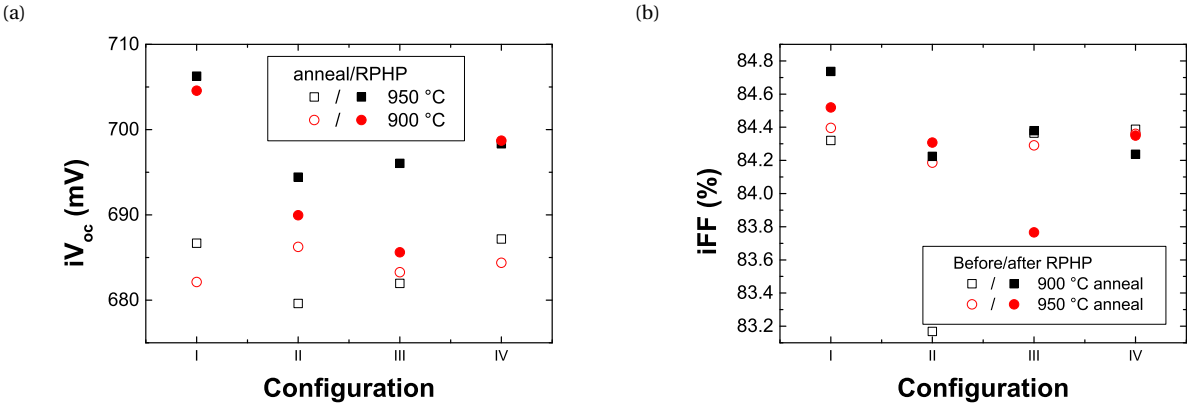

Figure 5.14: Obtained data for iV_{oc} and iFF values of the the different p-TOPCon layer configurations

values for all four configurations are displayed both before and after hydrogen passivation. Before RPHP, all configurations showed iV_{oc} values in the 680-690 mV range. The lowest iV_{oc} value was obtained for configuration II, without the capping layer and with a 10 nm a-Si:H(p) layer. After hydrogen passivation the standard stack, indicated by configuration I, showed the best passivation with an iV_{oc} value of 706 mV for the 900 °C anneal. Omiting the intrinsic a-Si:H layer only caused a slight reduction in the passivation quality. A bigger effect was observed for configuration II, where the capping layer was omitted. This effect could be partially compensated by the increased thickness of the a-Si:H(p) layer in configuration III, but only for the 900 °C anneal. For the 950 °C anneal, this configuration yielded the lowest iV_{oc} value. The iFF values from Figure 5.14b show reasonable results for all configurations. Again the best result was obtained for the standard stack with a T_{anneal} of 900 °C. The configuration with the thicker a-Si:H(p) layer showed a decrease in iFF value after RPHP for the 950 ° anneal, which was also observed for some samples in Section 5.2.

The sheet resistance was also extracted during the QSSPC measurements and can be found in Figure 5.15. From Figure 5.15 it can be seen that for the 950 °C anneal the R_{sheet} was 3-4 Ω/sq lower than for the 900 °C anneal. Removing the intrinsic layer resulted in approximately the same R_{sheet} value for the lower annealing temperature, and for the higher annealing temperature a small decrease was observed. Removing the

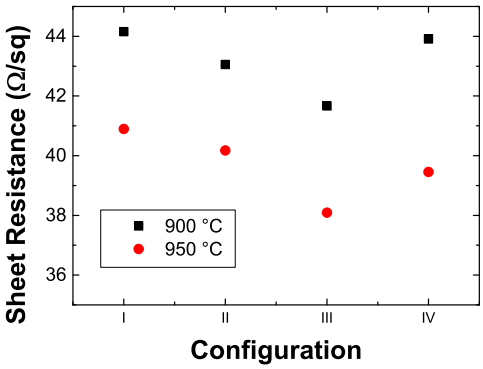

Figure 5.15: R_{sheet} values for the four different p-TOPCon configurations.

capping layer seemed to have a stronger influence on the sheet resistance with a decrease of 3-4 Ω/sq for both annealing temperatures. This effect was more visible when the the highly doped layer was increased in thickness. Since the base substrate consisted of 1 Ωcm n-type FZ material with a thickness of 200 μm a sheet resistance of 50 Ω/sq was to be expected, this was not observed for any of the measurements.

One of the possible explanations which was also mentioned in Section 5.1.2 is the decreased resistance due to dopant diffusion into the bulk material. To cross-check the dopant diffusion ECV profiles were obtained. The resulting profiles are shown in Figure 5.16. By looking at Figure 5.16 it becomes clear that the

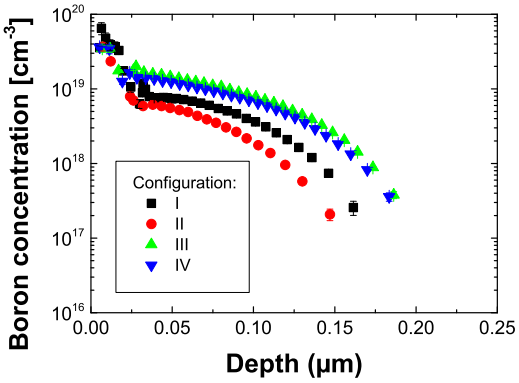

Figure 5.16: Dopant concentration profiles for the four different p-TOPCon configurations annealed at 950 ° C.

standard configuration had a profile that is of medium depth. Removing the capping layer reduced the profile depth, which can be overcompensated by the thicker doped layer. Removing the intrinsic layer increased the dopant profile depth and the surface dopant concentration. Comparing the resulting profiles with the sheet resistance values of Figure 5.15, the following stands out: removing the capping layer reduced the sheet resistance, but this was not reflected in the boron concentration profile. The profile was shallower and the surface boron concentration level lower than the standard sheet configuration. When the capping layer was replaced by 4 nm of a-Si:H(p), the boron diffusion increased significantly and the R_{sheet} value is reduced. This implies that boron diffusion occurs more easily in the a-Si:H(p) layer than it does in the SiC(p) layer. Finally, removing the intrinsic layer resulted in a higher surface boron concentration as well as a deeper profile. This was not reflected in the sheet resistance value, which was approximately at the same level as the standard configuration. Thus the intrinsic layer seems to function as a diffusion barrier for the boron atoms, whilst

only contributing slightly to the sheet resistance of the p-TOPCon stack. A possible explanation for the lower sheet resistance value for configuration II in combination with the shallow dopant concentration profile and the high R_{sheet} value for configurations I & IV could be that the capping layer has a high resistivity value. This would also explain the R_{sheet} value for configuration III, where the capping layer is replaced by an a-Si:H(p) layer.

Summarizing the results from this experiment: it was observed that both the intrinsic a-Si:H and the SiC(p) capping layer contribute significantly to the passivation quality of the p-TOPCon stack. Furthermore, removing the capping layer decreased boron diffusion into the bulk, implying that the capping layer is a source of boron atoms. Removing the a-Si:H(i) layer promoted boron diffusion into the bulk. The intrinsic layer might be important for the p-TOPCon stack because it inhibits boron diffusion, therefore minimizing the profile depth which seemed to have a beneficial effect on the passivation. The capping layer, although a source of boron, shows less diffusion than when the capping layer is replaced by an a-Si:H(p) layer. Therefore the capping layer also seems to slow down boron diffusion slightly. When looking at the sheet resistance, the intrinsic layer seems to have a minor contribution to the entire p-TOPCon R_{sheet} value. The capping layer, however, seemed to have a significant contribution to the R_{sheet} value.

5.4.2. Implementing the LPCVD a-Si layer

Since oxide deterioration under the influence of carbon diffusion has been reported in literature [91], the idea of implementing a carbon free intrinsic a-Si layer deposited by LPCVD underneath the TOPCon layers in order to protect the oxide arose. A further benefit of LPCVD deposited a-Si is the low hydrogen content of the layer, which allows for thicker layers to be grown whilst minimizing the risk of blistering.

Experimental details

In this experiment, a p-type 1 Ωcm FZ substrate was used. All wafers received the standard thermally grown oxide after the standard cleaning procedure. Thereafter a symmetric a-Si layer with a thickness of 5 nm was deposited with LPCVD at a temperature of 485 ° C. Thereafter the samples received six different TOPCon configurations deposited by PECVD. The process parameters for each of the six configurations can be found in Table 5.6. Two identical wafers were fabricated at the PECVD process and thereafter halved in order to

Table 5.6: Summary of the process parameters for the different configurations which were deposited on the 5 nm a-Si layer deposited by LPCVD.

Cofiguration	**a-Si:H(p) [nm]**	**B_2H_6/H_2 flow [sccm]**	**SiC(p) [nm]**	**B_2H_6/H_2 flow [sccm]**
I	10	50/50	4	50/50
II	25	50/50	4	50/50
III	-	-	14	50/50
IV	10	100/0	4	100/0
V	25	100/0	4	100/0
VI	-	-	14	100/0

obtain data for a wide range of annealing temperatures. The wafers were annealed at 900,950 and 1000 °C in the Tempress furnace.

Results and discussion

The resulting QSSPC data can be found in Figure 5.17. It becomes clear that adding the LPCVD layer did not improve the minority carrier lifetime with respect to the standard p-TOPCon configuration. Configuration II, which consists of the 25 nm a-Si:H(p) layer with normal dopant gas flow seemed to have the best iV_{oc} value, which also seemed to be stable with annealing temperature. However, the iFF values were not as good as for the standard p-TOPCon layer. Generally, the best iV_{oc} and iFF values were obtained for the 900 °C anneal. For the layers where the entire layer consists of SiC(p), a drop in iV_{oc} values was observed for the 1000 ° C anneal. For the other configurations this drop was less severe. Also increasing the dopant gas flow seemed to increase the temperature dependent degradation of the p-TOPCon layer.

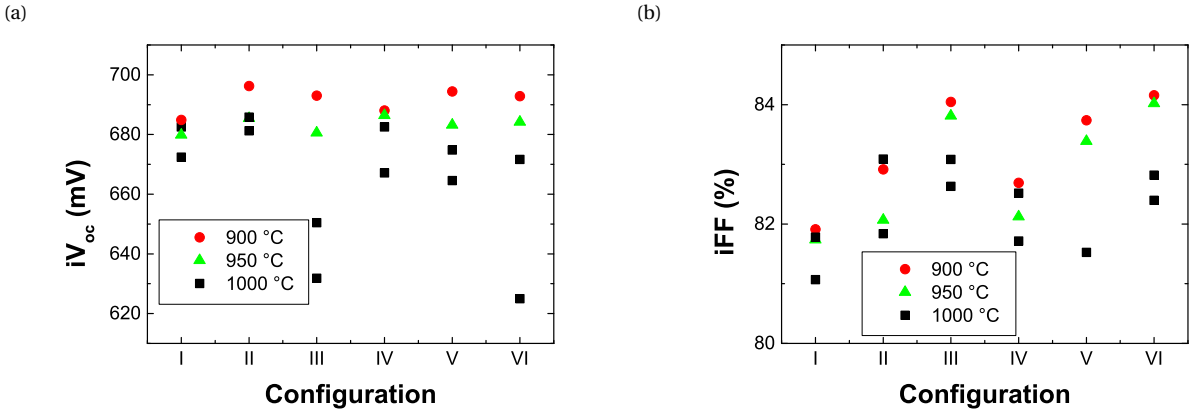

Figure 5.17: Obtained data for iV_{oc} and iFF values of the the lifetime samples with different TOPCon configurations deposited on top of 5 nm undoped a-Si.

The sheet resistance as well as the dopant profiles obtained with ECV measurements can be found in Figure 5.18. Comparing graphs Figure 5.18a and Figure 5.18b several interesting observations can be made about

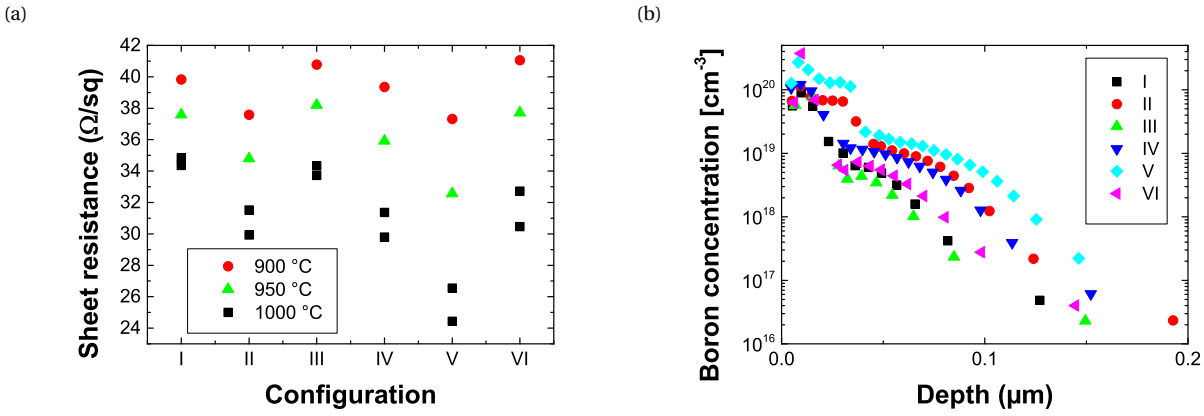

Figure 5.18: Obtained data for R_{sheet} from the QSSPC measurements as wel as the dopant concentration profiles obtained by ECV measurement for the samples annealed at 900 °C.

the correlation between the sheet resistance and the dopant profile depth. Figure 5.18a shows that by increasing the annealing temperature, the sheet resistance dropped, this usually corresponded with deeper dopant profiles. Futhermore, the configurations III and VI had the highest sheet resistance. These are the two configurations where the entire layer consists of SiC material. Looking at the configuration pairs I and II as well as IV and V, a clear decrease of the sheet resistance with an increasing doped layer thickness was observed. The

dopant gas flow seemed to have relatively little impact on the sheet resistance. By looking at the dopant profiles in Figure 5.18b one can observe that the SiC samples III and VI had a relatively shallow profile. Especially the highly doped configuration VI was shallow compared to the medium doped sample with the same thickness. The deepest profile was obtained by having a 25 nm doped layer with a high dopant gas flow and the second deepest profile was obtained by the 25 nm layer with normal dopant gas flow. It seems that increasing the a-Si:H(p) thickness led to a deeper dopant profile in combination with superior passivation. It is unclear if this improved passivation was caused by the enhanced dopant diffusion, or that the thicker poly-Si layer on top of the tunnel oxide was the cause. From Section 5.3 it can be concluded that a shallower dopant profile led to an increased passivation, this seems contradictory to the findings reported in this experiment. Thus it is more likely that the slight increase in passivation quality was caused by a thicker poly-Si layer instead of the increased diffusion of dopants into the bulk. Furthermore, the highest R_{sheet} values were obtained for the samples which contained entirely of SiC(p), this supports the hypothesis from Section 5.4.1 that the SiC(p) has a high sheet resistance and thus contributes to the sheet resistance of the entire p-TOPCon stack in a significant way. In past experiments, blistering has been reported for the TOPCon configuration layers [90]. In order to prevent blistering it is important to minimize the hydrogen content of the layer or to facilitate hydrogen effusion. No blistering occurred during this experiment, so increased thickness of the TOPCon layer proved possible on the intrinsic layer deposited using LPCVD. But since the passivation of the p-TOPCon layer was not enhanced it is not beneficial to implement a LPCVD layer into the p-TOPCon configuration at this point. The fabrication in two different reactors increases the risk of contamination as well as increasing the fabrication process complexity.

5.5. Summary of the results

In this chapter, the p-TOPCon stack was optimized by conducting four experiments. In the first experiment, the status quo was reproduced for both the UV/O_3 and the O_3 oxide. The dopant gas flow as well as the annealing temperature was optimized for both oxides. It was shown that the fabrication line functioned as expected, obtaining good passivated contacts with an iV_{oc} of 712 mV for an asymmetric n-TOPcon/p-TOPCon sample for the UV/O_3 oxide at a T_{anneal} of 875 °C and a B_2H_6/H_2 flow ratio of 50/50 sccm. For the sheet resistance both a sharp decline with increasing diboran flow as well as annealing temperature was observed. The O_3 oxide structurally showed lower R_{sheet} values than the UV/O_3. This was also reflected in the dopant concentration profiles which were obtained using ECV. Increasing diboran flow increased the dopant concentration profile depth and the O_3 oxide structurally had deeper profiles. Hence, it is concluded that there is a correlation between the ability of the tunnel oxide to block boron diffusion and the passivation quality of the p-TOPCon layer.

In the following experiment, a thermally grown tunnel oxide was introduced which yielded excellent passivation quality for both n- and p-TOPCon. The superior oxide was grown at a N_2/O_2 gas flow ratio of 7/3 slm and an oxidation temperature of 600 °C. This oxide resulted in an iV_{oc} of 710 mV with an iFF of 84.5 % for a symmetric p-TOPCon sample and an iV_{oc} of 732 mV with an iFF of 86.8 % for n-TOPCon. The thermally grown oxide showed a good thermal stability up to 1000 °C for p-TOPCon. For n-TOPCon, the thermal stability was lower. It was observed from ECV profiles that after a 1000 °C anneal, phosphorus was able to diffuse into the bulk unhindered, whereas boron still encountered a diffusion barrier. A structural difference between p- and n-TOPCon is the possible cause of this enhanced phosphorus diffusion and thus decreased thermal stability for n-TOPCon.

The thermally grown oxide was compared to the UV/O_3, O_3, and HNO_3 oxides, yielding the best results

for the TO. Not only the passivation quality, but also the thermal stability and the boron diffusion blocking proved to be superior for the thermally grown oxide. The oxides were compared in the EDNA freeware, from which it was concluded that the effective SRV was lowest for the TO, indicating superior passivation quality.

The final experiment consisted of variations of the p-TOPCon stack itself. The importance of the intrinsic a-Si:H and SiC(p) for the passivation quality were investigated. It was concluded that both layers are essential to obtain good passivation, since both layers slow down boron diffusion into the bulk. Furthermore, it was found that the intrinsic a-Si:H only has a slight contribution to the R_{sheet} value of the p-TOPCon layer, whereas the SiC(p) layer contributes significantly to this value. This might have consequences for the contactability of the p-TOPCon layer with SiC(p) capping. Furthermore, the intrinsic a-Si:H layer was replaced by an a-Si layer deposited with LPCVD. This was investigated since the lower hydrogen content of the layer deposited with LPCVD might allow for thicker layer deposition without blistering and to protect the oxide from deterioration through components from the TOPCon layer. It was found that implementing an LPCVD did not increase the passivation quality. Increasing the a-Si:H(p) layer did partially compensate the passivation loss, but not to an extend where it became beneficial. Furthermore it was observed that the configurations which entirely consisted of SiC(p) had a substantially higher R_{sheet} value, further supporting the hypothesis that the capping layer made a significant contribution to the sheet resistance of the p-TOPCon layer.

6

Surface recombination versus contact resistivity

In this chapter the relationship between the surface recombination velocity S_{eff} *and the contact resistivity* ρ_c *will be examined. There seems to be an intrinsic trade-off between these two parameters. One possibility is that there is extremely good passivation with only few defects at the interfaces, which results in a very low surface recombination velocity, but it is extremely difficult to obtain a good contact between the metal and the passivating contact. On the other hand contacts with a very low specific resistivity are often plagued by a high number of of interface defects, undermining the passivation and increasing the surface recombination velocity and the leakage current. In order to better understand this relationship, the contact resistivity of the samples was determined and both the oxide tunneling model and the pinhole model, which are described in Section 2.7, were fitted to the data points.*

6.1. contact resistivity comparison between metallization stacks

The first experiment that was conducted in order to determine the contactability of the p-TOPCon configuration, was a variation of the metallized layer. The goal of this experiment was to determine which metal stack provided a good contact to the boron doped capping layer.

6.1.1. Experimental details

A general overview of the metal stacks used to make TLM samples can be found in Table 6.1. Since the fabrication sequence of solar cells usually includes a TCO on top of the doped poly-Si layer, the contactability of this layer was investigated. A material that is typically used as a TCO layer is indium tin oxide (ITO), hence an ITO layer was chosen as one of the metallization schemes. Another metallization scheme that showed good contactability in earlier experiment is a stack of titanium, palladium, and silver, this stack will hereafter be indicated by TiPdAg. The metals were deposited with thermal evaporation with a thickness of 50/50/300 nm. Since good results were obtained before, this stack was also chosen as one of the metallization schemes. The third and final metallization stack that was chosen, is a 15 nm layer of tungsten oxide, combined with the standard TiPdAg layer. This configuration was chosen since tungsten oxide is a well known transition metal

oxide used for hole selective contacts [46]. Therefore, it might increase the contactability of the TiPdAg stack and result in a lower contact resistivity.

Table 6.1: Overview of the metallization stacks used to make TLM samples in order to compare contact resistivity values

Stack name	**Material 1**	**Thickness [nm]**	**Material 2**	**Thickness [nm]**	**Material 3**	**Thickness [nm]**
TiPdAg	titanium	50	palladium	50	silver	300
WO_x+TiPdAg	WO_x	15	TiPdAg	400		
ITO	ITO	100				

6.1.2. Results and discussion

An exemplary measurement for both the ITO stack and the TiPdAg stacks at 950 °C anneal can be found in Figure 6.1 From Figure 6.1, the following conclusions can be drawn: the ITO layer resulted in the lowest to-

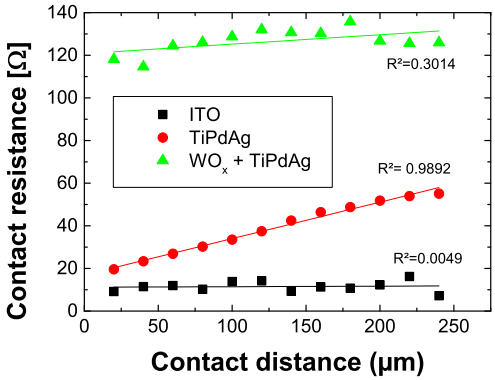

Figure 6.1: Plot of the contact resistance versus the contact distance for the three metallization schemes. The fits are plotted in the same graph.

tal contact resistance, but since the slope of the curve was not steep, the resulting specific contact resistivity value was quite high. Also the linear fit through the data points was not accurate, with an R-squared value of only 0.005. This fit resulted in a great uncertainty in the contact resistivity which becomes clear from Figure 6.2. The TiPdAg resistance showed a stronger increase with increasing contact distance, which led to a lower specific contact resistivity value. The linear fit also showed a good R-squared value of 0.98. Finally, the WO_x TiPdAg stack showed the highest contact resistance. Since the slope of this graph was also relatively low, the resulting specific contact resistivity value was high. The R-squared value was low at 0.3014. The resulting specific contact resistivity values from the circular TLM measurements can be found in Figure 6.2. The following can be concluded from Figure 6.2: TiPdAg provided the lowest contact resistivity results, followed by the ITO layer and the combination of WO_x and TiPdAg provided the highest contact resistivity value. Furthermore, it can be concluded that the uncertainty in the contact resistivity value is extremely high. This is caused by a large fluctuation in the contact resistance values. Since the relationship is assumed to be linear, as is described in Section 4.5, these fluctuations lead to high uncertainty in the contact resistivity value, which can be seen by looking at the R-squared values from Figure 6.1. It seems that adding the WO_x layer does not enhance the contact resistance the p-TOPCon layer, but rather diminishes it. The annealing temperature did not seem to have a big effect on the contact resistivity values. For the TiPdAg contacts, a slight increase is

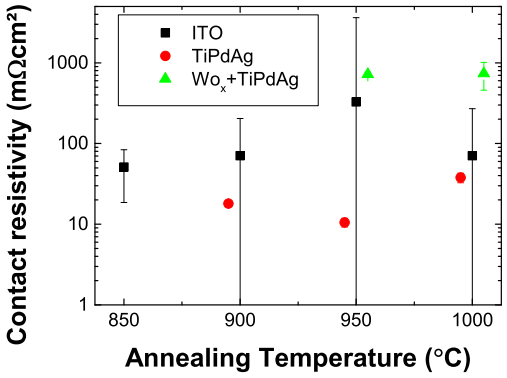

Figure 6.2: Specific contact resistivity values for different metallization stacks on p-TOPCon for different annealing temperatures for the TOPCon layer. The contact resistivity values were obtained using circular TLM structures.

observed for the 1000 °C anneal, but there is not enough data present at this moment to draw conclusions. From Figure 6.1 the TiPdAg showed the best fit for the TLM measurements and in Figure 6.2 it also showed the lowest specific contact resistivity values. Thus the TiPdAg layer seemed the most promising metallization scheme.

6.2. Contact resistivity comparison between oxides

After the optimal metallization scheme was determined, the relationship between the passivation quality and the contact resistivity was investigated and the influence of the tunnel oxide on the contact resistivity determined. In order to better understand this relationship, the samples that were subjected to the EDNA analysis in Section 5.3 were also used to conduct contact resistivity measurements using TLM. The TiPdAg metal stack was chosen since it yielded promising contact resistivity values.

6.2.1. Results and discussion

The resulting contact resistivity values of the samples with the four different oxides can be found in Figure 6.3. It is clear that most of the measured contact resistivity values were at a level where no fill factor losses are to

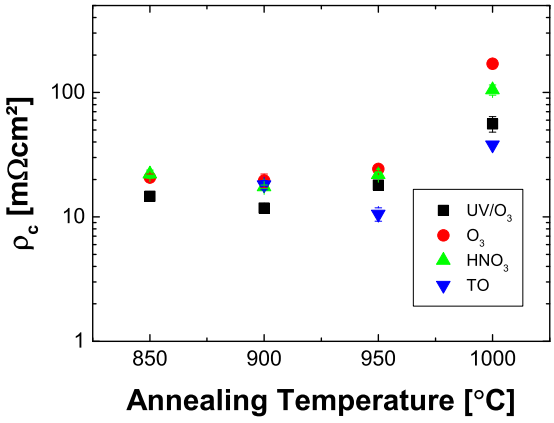

Figure 6.3: Specific contact resistivity values for all four oxides plotted against annealing temperature. The contact resistivity values were obtained using circular TLM structures.

be expected. If the contact resistivity is too high, the high series resistance in the metal poly-silicon contact will cause these fill factor losses. The boundary value where this occurs lies around 100 mΩcm^2 for full area contacts. Since a TOPCon layer is typically used in this configuration, the contact resistivity values observed here fell well within that margin. The O_3 oxide generally resulted in the highest contact resistivity values, followed by the HNO_3 oxide. The UV/O_3 oxide showed the best contactability for the lower annealing temperatures, but for the 950 and 1000 °C anneal the thermally grown oxide had the lowest contact resistivity values. The lowest contact resistivity value was obtained for the thermally grown oxide at an annealing temperature of 950 °C. For this sample a ρ_c of 10 mΩcm^2 was obtained. From Figure 5.8 it was concluded that this fabrication process also yielded the best passivation quality.

Another striking trend in Figure 6.3 is the rise in specific contact resistivity for the 1000 °C anneal. This was also observed in Section 6.1, but then not enough data point were available. Traditionally a trade-off between passivation and contactability is observed, so one would expect decreasing contact resistivity values with increasing annealing temperature, at least between the TOPCon layer and the bulk. This was also observed for the n-TOPCon layer in earlier experiments [95]. Another possibility is that the contact resistivity between the TOPCon layer and the metallization layer was increased. It is known that during the high temperature anneal, the semiconductor surface oxidizes, even if the samples are annealed under a pure nitrogen atmosphere. In order to remove this parasitic oxide, a 30 second dip in hydrofluoric acid was built into the processing sequence before metallization. Since the capping layer of the p-TOPCon layer contains carbon, there is a possibility that instead of a SiO_x oxide, a parasitic SiC_xO_y oxide was grown, as has been reported before in literature by Schnabel et al. [96]. An increased stability in HF solutions was observed for this parasitic oxide which might mean that a 30 second HF dip was not sufficient to completely remove the oxide. This would increase the contact resistivity between the metal and the TOPCon layer, and thus the entire contact resistivity.

It should be noted that the circular TLM measurements, although better than the linear TLM measurements, still not allow perfect extraction of the specific contact resistivity. As mentioned in Section 4.5, bulk current flow is neglected during contact resistivity determination, thereby overestimating the contact resistivity value. Since the main goal of this thesis is to ensure proper solar cell functioning, it is more important to determine whether the contact resistivity is below a level where fill factor losses become significant. For good extraction of the specific contact resistivity, Quokka simulations of each sample have to be made and fitted manually. There is research going on which aims to further automate this process, thereby allowing for more accurate contact resistivity determination.

6.3. Influence of tunnel oxide on contact resistivity

In order to better understand the influence of the tunnel oxide on the specific contact resistivity value, and experiment was designed in which the tunnel oxide was varied. All the other fabrication remained equal which enabled isolation of the influence of the tunnel oxide on the passivation as well as the contact resistivity value. The experimental details will be described in the following section.

6.3.1. Experimental details

As a substrate material the 250 μm thick 1 Ωcm p-type FZ wafers were used. After the standard cleaning procedure, the tunnel oxides were grown under different conditions in two identical Centrotherm furnaces. The process parameters for the tunnel oxide growth process can be found in Table 6.2. The thickness of the grown oxides were determined using spectroscopic ellipsometry. In order to measure the thickness as accurately

Table 6.2: Parameter from the oxidation process to grow the four different tunnel oxides.

process	N_2/O_2 flow [sccm]	Furnace temperature [° C]	Oxidation time [min]
1	10/0	600	10
2	7/3	600	10
3	4/6	600	20
4	4/6	700	10

as possible, a spare wafer was cleaned and a base ellipsometry measurement was conducted on this wafer directly after receiving the HF-Dip. For each of the oxidation processes, one extra wafer was processed which was measured using spectroscopic ellipsometry after the wafers left the clean room. For increased accuracy, the measurement was conducted at three angles and three different methods of extracting the oxide thickness were implemented, which are described in Section 4.2. The remaining wafers which were oxidized received the standard p-TOPCon stack during PECVD processing. After PECVD deposition, the samples were halved and annealed at three different temperatures: 900,950 and 1000 °C. Finally, RPHP processing for 30 minutes at 400 °C was used for dangling bond passivation. To see if the diffusion of the dopants into the bulk was different for the different tunnel oxides, ECV measurements were conducted on the samples annealed at 950 °C for each oxide. For each oxide and annealing temperature, TLM samples were produced using the thermally evaporated TiPdAg stack on top of the p-TOPCon layer. In order to prevent an increase in contact resistivity values for the 1000 °C anneal, the SiO_x etching step during the fabrication process was increased to 1 minute.

6.3.2. Results and discussion

The resulting thickness from the spectroscopic ellipsometry measurements of each of the four oxidation processes can be found in Table 6.3. For each oxidation process, four points on the wafer were measured and the minimum and maximum measured thickness is shown in Table 6.3. Looking at Table 6.3 it becomes clear

Table 6.3: Measurement results from the spectroscopic ellipsometry measurements.

Oxidation process	S_{rough} method [nm]	I_{jaw} method [nm]	Optical constants method [nm]
1	0.49-0.55	1.00-1.03	0.48-0.52
2	0.82-0.90	1.32-1.38	0.806-0.862
3	0.67-0.79	1.18-1.28	0.66-0.77
4	0.99-1.06	1.49-1.54	0.98-1.02

that the oxidation process under a pure nitrogen flow yielded the thinnest tunnel oxide. The oxide thickness, was still nonzero, however. The oxide with a 4/6 N_2/O_2 gas flow, which was grown at 600 °C for 20 minutes, resulted in the second thinnest oxide. The thickest tunnel oxide was obtained during the oxidation process at 700 °C. The different measurement methods yielded different thickness results, with the I_{jaw} method structurally resulting in a higher oxide thickness than the other two methods. This can be explained by the fact that the native oxide, or surface roughness which is present on the wafer even after the HF dip, is not subtracted for the I_{jaw} method. It should be noted that the thickness of a layer with sub-nanometer thickness cannot be determined accurately with spectroscopic ellipsometry. It is difficult to obtain the right values for the optical constants and the bulk influences the measurement to a great extent [77].

The passivation of the samples after RPHP was determined by QSSPC measurements and the resulting iV_{oc} values can be found in Figure 6.4. Figure 6.4 shows that there was a great variation in the passivation

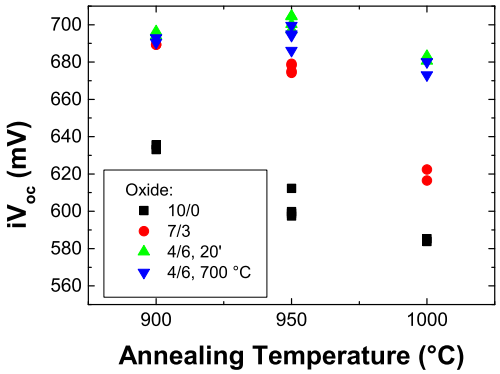

Figure 6.4: iV_{oc} for the four different oxidation processes at three different annealing temperatures.

quality for the different oxidation processes. The first oxide, which was grown under a pure nitrogen gas flow, shows inferior passivation to the other oxides. The passivation further decreases for increasing annealing temperature. The second oxide, with a 7/3 slm N_2/O_2 flow, showed good passivation for the 900 and 950 °C anneal. For the 1000 °C anneal, however, the passivation dropped significantly. Both oxides with the 4/6 N_2/O_2 showed good passivation, with the oxide grown at 600 °C performing slightly better. It is remarkable that in Section 5.2, the oxide grown under pure nitrogen showed good passivation, where it performs significantly worse in this experiment. This oxidation process is not very consistent from experiment to experiment and yields varying passivation quality results.

In order to investigate the boron diffusion, dopant profiles were obtained. The resulting dopant profiles from the ECV measurements can be found in Figure 6.5. From Figure 6.5 it can be seen that the oxide grown

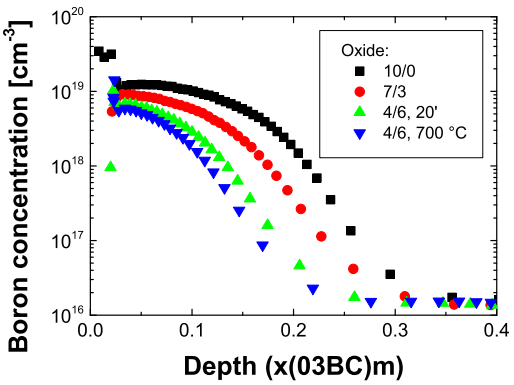

Figure 6.5: Dopant concentration profiles obtained through ECV measurements for the four different oxidation methods. All samples were annealed at 950 °C.

under a pure nitrogen atmosphere allowed the most dopant diffusion into the bulk. The dopant diffusion decreased with increasing oxygen flow. The lowest dopant diffusion was observed for the oxide grown at 700 ° C. This oxide showed also the highest thickness during the spectroscopic ellipsometry measurements as can be seen in Table 6.3. The thinnest oxide also showed the most diffusion of dopants into the bulk. A remarkable phenomenon is observed for the oxide which is grown at a 4/6 N_2/O_2 gas flow ratio for 20 minutes. Although

the oxide is thin according to the SE measurements

The TLM measurement results can be found in Figure 6.6. Comparing the oxides in Figure 6.6, the oxide

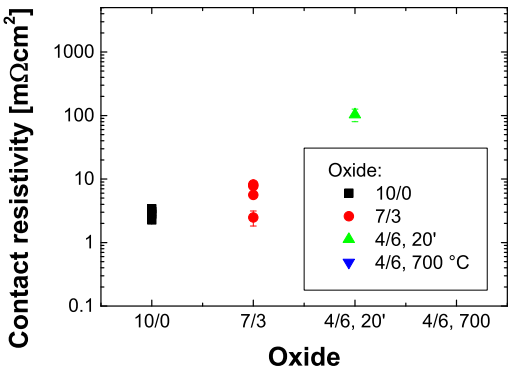

Figure 6.6: TLM measurement results from circular TLM structures for four different oxides.

grown under a pure nitrogen gas flow showed the lowest contact resistivity values. It should be noted that the specific contact resistivity values which are obtained during circular TLM measurements, are likely to be an overestimation of the actual specific contact resistivity values. This is due to inaccuracies when accounting for the bulk current flow and other measurement uncertainties as was explained in Section 4.5. All data points were below 10 mΩcm^2 for this oxide. With an increasing oxygen flow, the specific contact resistivity values increased as well. For the oxide which was grown at 700 °C, no specific contact resistivity values could be extracted from the TLM data. No ohmic contact was achieved between the metal and the TOPCon layer, which is a prerequisite for a good contact resistivity measurement. From this experiment is is shown that the tunnel oxide can make a significant contribution to the contact resistivity of the TOPCon layer. For oxides with a long oxidation time or which are oxidized at a high temperature, no ohmic contact was achieved after metallization. It is still unclear if the oxide itself prevented the formation of an ohmic contact. All samples received identical treatments except for the oxidation process, which makes the tunnel oxide a likely cause. More data points are needed in order to make a statistically relevant statement, however. For the tunnel oxide which is typically used in the TOPCon layer, ρ_c values below 10 mΩcm^2 were obtained, which is below the FF loss limit for full area contacted cells.

6.4. Fitting to the theoretical models

In order to better understand the phenomena that describe the current flow through the tunnel oxide, the specific contact resistivity data obtained for the different oxides at an annealing temperature were fitted to both the oxide tunnelling and the pinhole model in order to determine whether these models can be used to describe the relationship between contact resistivity and recombination current.

6.4.1. Experimental details

For the tunneling oxides, which is described in Section 2.7, the used parameter values can be found in Table 2.1. As can be seen in Figure 2.5, the oxide thickness should be varied over a large range in order to simulate the entire range of contact resistivity values. Since the grown tunnel oxides have a thickness from approximately 0.5 till approximately 1.5 nm, this is not a realistic scenario. Hence, it is important which values for the barrier heights for electrons and holes are chosen. The values which are found in literature vary

from the values used in Table 2.1 until barrier heights of $\phi_{ox,e}$ = 1 eV and $\phi_{ox,h}$ = 0.3 eV. The resulting graphs for both barrier height pairs can be found in Figure 6.7. Figure 6.7 shows that the different barrier height values lead to different regimes for an oxide thickness of 0.5-1.5 nm. The low barrier heights of 1 and 0.3 eV for electrons and holes, showed a strong dependence of the recombination current on the contact resistivity. It is therefore clear that for these barrier heights, the recombination current is limited by the tunneling through the oxide and not the recombination at the Si/SiO_x interface. For the barrier heights as mentioned in Table 2.1, the recombination current reaches the saturated regime where the interface recombination becomes dominant. The higher barrier values were chosen since these correlated with the contact resistivity values that were obtained during the TLM measurements in Section 6.1. If the region within the two regions shown in Figure 6.7 is to be described, this can be done by either varying the oxide thickness or barrier heights. Since an oxide thickness of several nm is not realistic for a TOPCon sample, this region is left blank. In the following

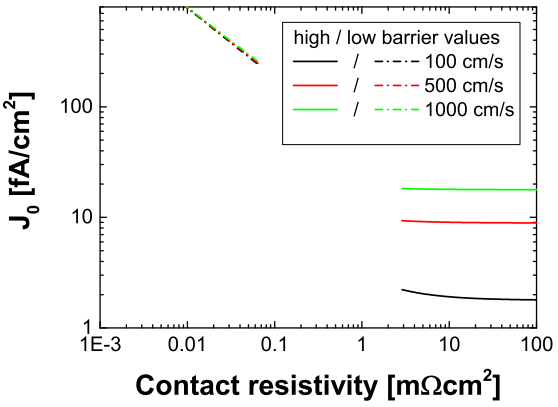

Figure 6.7: Comparison between the different barrier height values for electrons and holes

section the obtained TLM values from Section 6.2 and Section 6.3 will be fitted to the oxide tunneling and the pinhole model. For the pinhole model, the parameters can be found in Table 2.2 and they were determined as follows: the pinhole radius and the recombination velocity at the pinhole surface were adopted from earlier work by Peibst et al [4]. The depth of the profile and the acceptor concentration were adopted from the ECV profile. Since the model assumes a square profile, an estimate is made for which the profile resembles the ECV profile. And example can be found in Figure 6.8. From this profile, the depth of the diffused layer and the surface concentration were determined, the resulting values can be found in Table 2.2. For the experimental values, contact resistivity values from Section 6.2 were used.

6.4.2. Results and discussion

In Figure 6.9, the experimental ρ_c values are plotted against the extracted J_0 values. The open symbols represent the samples for which the TOPCon layer was annealed at 900 °C, the filled symbols represent the samples for which the TOPCon layer was annealed at 950 °C. The dotted lines represent the outcome of both the oxide tunnelling and the pinholes model for different interface recombination velocity values. The used SRV values are indicated next to the dotted lines.

It becomes clear from Figure 6.9 that all samples had contact resistivity values in the same range. The samples annealed at 950 °C showed a higher saturation current density J_0 than the samples annealed at 900 °C. Both the tunnel oxide model and the pinholes model can be fitted to the experimental data points. Furthermore, it is evident from Figure 6.9a and Figure 6.9b that all experimental data laid in the saturated regime

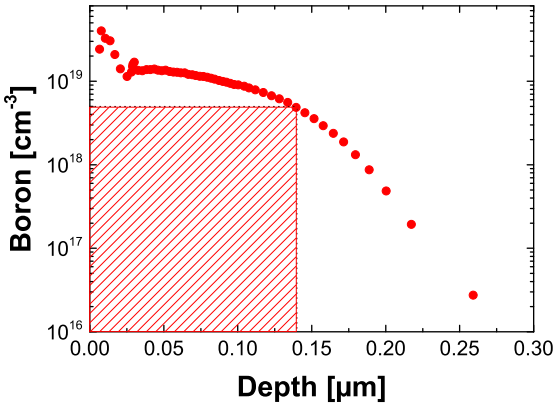

Figure 6.8: Examplary approximation of the profile depth W and the profile dopant concentration N_A used for the pinhole model implementation.

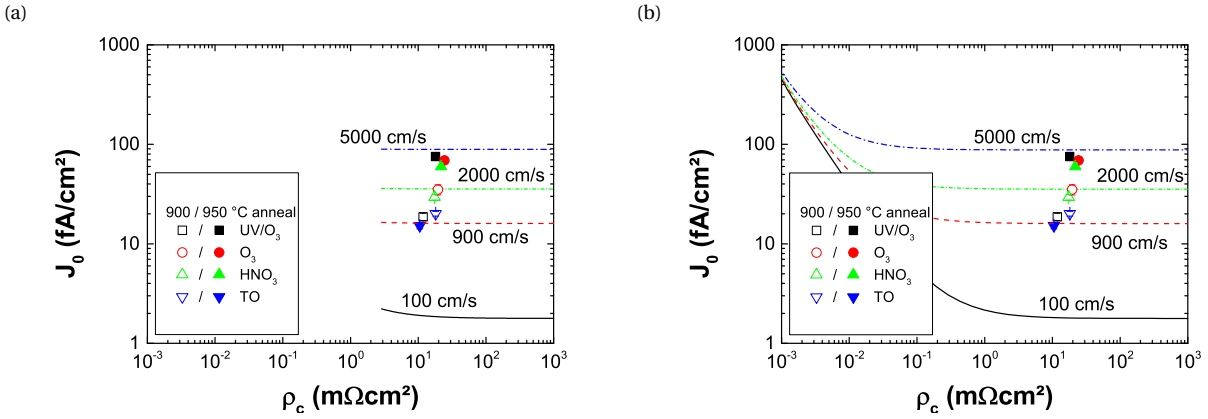

Figure 6.9: Experimental contact resistivity values obtained by TLM plotted against saturation current density obtained by QSSPC. The data is fitted by both the oxide tunnelling and the pinholes model.

of the curves. The tunnel oxide is best fitted with a SRV value of 900 cm/s, which corresponds well with the result obtained during the EDNA analysis in Section 5.3 as can be seen in Figure 5.11. The samples with the other three oxides, which were annealed at 950 °C, showed S_{eff} values in the 5300-5500 cm/s range during the EDNA analysis. In Figure 6.9 the value that best fits these data point laid below 5000 cm/s, so there was a small discrepancy between the EDNA analysis and the model fit.

This discrepancy can have multiple causes. First of all, some of the model parameters are quite arbitrary and not obtained from measurements. Altering these values will alter the model output curves of the model and thereby altering the SRV value that results in the best fit. The ECV profiles are not identical for all oxides, but in order to make a comparable fit a general profile depth and acceptor concentration was assumed. This can lead to a slight offset in the SRV value for some samples. Furthermore, an uncertainty is present in the saturation current extraction from the QSSPC measurement. There is a standard deviation shown in Figure 6.9, but it might be possible that this does not include all measurement uncertainties. An erroneous J_0 extraction would shift the data points vertically and thereby altering the SRV value for which the best fit is obtained. Problematic is the fact that both models show the same behaviour for the range where the experimental data was obtained, which makes it impossible to rule out one of the two models. Experimental data with a contact resistivity values below 0.1 mΩcm^2 would be a good addition to prove the validity of the

models. Unfortunately, the lowest contact resistivity value that was obtained with the thermally grown oxides was 2 mΩcm^2. For this sample, the passivation quality was not good enough to extract the saturation current using the Kane & Swanson method. Future work could entail development of samples with a lower contact resistivity value. Another possibility is that the contact resistivity is overestimated during TLM measurements, as was described in Section 4.5. Further development of accurate contact resistivity extraction from TLM measurement could also help determine the accuracy of both models, and eventually come to a better understanding of the underlying principle which controls the current flow through p-TOPCon contacts.

6.5. Summary of the Results

In this chapter, the contact resistivity of the p-TOPCon passivation contact was investigated and the correlation with the passivation quality determined. During the first experiment, three different contacts were compared: the ITO layer, the TiPdAg stack and a 15 nm WO_x layer combined with the TiPdAg layer. The TiPdAg layer resulted in the best contactability. For the ITO and WO_x+TiPdAg stack, it proved difficult to obtain good TLM measurement, as the contact resistance showed large fluctuation. After the metallization with the lowest ρ_c value was determined, the contact resistivity of the TO was compared with the UV/O_3, O_3 and HNO_3 oxides. All oxides showed contact resistivity values in the same order of magnitude. For the higher annealing temperatures of 950 and 1000 °C, the thermally grown oxide performed the best. With the lowest contact resistivity value being 10 mΩcm^2 for the thermally grown oxide at an annealing temperature of 950 °C. An increase in the contact resistivity was observe for all oxides at a 1000 °C anneal. It is expected that a parasitic SiC_xO_y layer grew during the high temperature anneal, thereby increasing the interface resistance between the metal and the TOPCon layer. In order to further understand the contribution of the tunnel oxide on the specific contact resistivity, four oxidation processes were performed after which identical p-TOPCon layers were deposited. From these samples the thinnest oxide, which was grown under pure nitrogen gas, showed the lowest contact resistivity. This was combined with a bad passivation quality. Increasing the oxygen flow increased both the passivation and the contact resistivity. The thickest oxide, which was grown at 700 °C, prevented the formation of an ohmic contact between the metal layer and the bulk.

In the final experiment, the experimental data was fitted by both the oxide tunnelling model and the pinholes model. Both models could successfully describe the experimental results and the SRV values that resulted in the best fit were comparable to the S_{eff} values from the EDNA analysis. All experimental data point laid in the saturated regime of the models, thereby making it difficult to confirm the validity of both models. In order to do this, experimental data with lower contact resistivity values are needed, or the contact resistivity value extraction needs to be improved.

7

Conclusions and Outlook

In this thesis, the p-TOPCon passivating contact was further developed and optimized. In order to achieve this, two approaches were taken. First, the passivation quality was optimized in four experiments. Secondly, the contact resistivity of the p-TOPCon contact was investigated and the link to the passivation quality determined in four more experiments. From the first experiment, it was determined that the status quo could be reproduced without major issues occuring during the processing sequence. Good passivation quality was obtained for both the UV/O_3 and the O_3 oxide. It was determined that the UV/O_3 oxide proved a better barrier for dopant diffusion, and also showed higher iV_{oc} values.

In the next experiment, the thermally grown oxide was introduced to the p-TOPCon fabrication sequence. The thermally grown oxide was expected to be dense and thus might improve the passivation quality. Good passivation results were obtained for the thermally grown oxide, with the best performing oxide having an oxidation temperature of 600 °C and a gas flow ratio of 7/3 slm N_2/O_2. The thermally grown oxide was compared to three other oxidation methods in terms of passivation quality, contact resistivity and temperature stability. The passivation obtained with the thermally grown oxide was superior to the other oxides. Furthermore, the TO showed an improved thermal stability over the other three oxides, maintaining good passivation for an annealing temperature up to 1000 °C. The boron diffusion was also lower for the thermally grown oxide.

After the most suitable tunnel oxide was determined, the p-TOPCon layer was optimized, investigating the contribution of the individual components to the passivation quality. It was found that both the intrinsic a-Si:H and the SiC(p) capping layer proved beneficial to the passivation. The intrinsic a-Si:H layer reduced the diffusion of boron into the bulk and the same effect was observed for the SiC(p) capping layer. Therefore it is concluded that both the intrinsic and the capping layer lead to decreased boron diffusion. Removing the capping layer caused a drop in the sheet resistance, which led to the hypothesis that the capping layer makes a significant contribution to the sheet resistance of the p-TOPCon stack. For the intrinsic layer, this contribution appeared to be minimal. Replacing the a-Si:H layer by an intrinsic layer deposited with LPCVD proved detrimental to the passivation quality. Replacing the TOPCon stack by one SiC layer also proved detrimental, although a rise in sheet resistance was observed which supported the hypothesis that the capping layer contributes significantly to the sheet resistance. For the LPCVD configuration, no blistering occurred even for the thicker doped layer. It is yet unclear at which thickness blistering starts to occur. Further work could

be done on the influence of the p-TOPCon layer stack on the contact resistivity. Omitting the capping layer might lead to better contactability for the TOPCon stack.

The contact resistivity values for different metallization schemes were compared. ITO, a common TCO, proved to have a high contact resistivity and it proved difficult to obtain a clean TLM measurement due to high resistance fluctuations. For the WO_x+TiPdAg stack, the same problems occured. The TiPdAg stack itself proved to make a good contact to the p-TOPCon layer which lead to a contact resistivity value for which no fill factor losses are to be expected. The contactability of p-TOPCon with four different tunnel oxides was compared. The contact resistivity proved to be comparable for all of the four oxides, with the TO having a slightly lower value for the higher annealing temperatures. Research could be done on improving the accuracy of the TLM measurement technique as the contact resistivity is likely to be overestimated during circular TLM measurements due to bulk current flow and other effects [88]. For the thermally grown oxide, the oxidation process was varied to obtain oxides with different thicknesses. The effect on this oxide thickness on the passivation and the contact resistivity was investigated. The oxide grown under pure nitrogen resulted in the lowest contact resistivity, but the passivation quality was inferior. It is remarkable that oxidation occured, even under a pure nitrogen atmosphere. It is not yet fully understood what causes the oxidation of the wafer under these conditions. It was observed that the contact resistivity increased with increasing oxygen flow, showing that the tunnel oxide might have a significant effect on the contact resistivity. For the thickest oxide, no ohmic contact could be achieved. More statistical data is needed however, to be able to draw conclusions about the influence of the tunnel oxide on the contact resistivity.

In order to better understand the relationship between the contact resistivity and the surface recombination velocity, two theoretical models were selected and fitted to the data. The oxide tunneling model and the pinhole model were fitted to experimental contact resistivity data and a reasonable fit was obtained. The resulting SRV values from the models correlated with the S_{eff} values from the EDNA analysis. Since all data points laid in the saturated regime of both models, it was impossible to exclude a model. Samples with lower contact resistivity should be developed in order to get more insight in the correctness of the models.

Overall, the passivation of the p-TOPCon contact was improved over the status quo. The main contribution to this improvement is made by the thermally grown oxide. In order to further optimize the p-TOPCon contact, this oxide should be studied more thoroughly. It was experienced that some fluctuations in the passivation quality occur due to oxidation inhomogeneities, thus optimizing the oxidation process could further improve the p-TOPCon contact. As for the p-TOPCon stack itself, it seems that the optimal configuration has been achieved. It might be possible that the equipment used to fabricate the samples is the limiting factor at this moment, which is not easily resolvable.

A

List of acronyms

ALD atomic layer deposition

Al_2O_3 aluminium oxide

a-Si amorphous silicon

a-Si:H hydrogenated amorphous silicon

BOS balance of system

c-Si crystalline silicon

DI water deionized water

ECV electrochemical capacitance-voltage

FF fill factor

FZ float zone

Ga_2O_3 gallium oxide

HF hydrofluoric acid

HIT Heterojunction with Intrinsic Thinlayer

HNO_3 nitric acid

IBC inderdigitated back contact

IC integrated circuit

iFF implied fill factor

ISFH Institute for Solar Energy Research

iV_{oc} implied open-circuit voltage

LPCVD low pressure chemical vapour deposition

MoO_x molybdenum oxide

PECVD plasma enhanced chemical vapour deposition

PERC passivated emitter and rear cell

poly-Si polycrystalline silicon

PV photovoltaic

QSSPC quasi-steady-state photo conductance

RPHP remote plasma hydrogen passivation

R_{sheet} sheet resistance

RTP rapid thermal processing

SE spectroscopic ellipsometry

Si silicon

SiC silicon carbide

SiN_x silicon nitride

SiO_x silicon oxide

SIPOS semi-insulating polysilicon

SRV surface recombination velocity

T_{anneal} annealing temperature

TCO transparent conductive oxide

TiO_x titanium oxide

TLM transfer length method

TOPCon tunnel oxide passivating contact

V_{oc} open-circuit voltage

WO_x tungsten oxide

Bibliography

[1] K. Yoshikawa, H. Kawasaki, W. Yoshida, T. Irie, K. Konishi, K. Nakano, T. Uto, D. Adachi, M. Kanematsu, H. Uzu, *et al.*, "Silicon heterojunction solar cell with interdigitated back contacts for a photoconversion efficiency over 26%," *Nature Energy*, vol. 2, p. 17032, 2017.

[2] "New world record efficiency of 25.7 % for both sides-contacted monocrystalline silicon solar cell," *Fraunhofer.de*, Apr 2017.

[3] Y. H. Kwark, R. Sinton, and R. M. Swanson, "SIPOS heterojunction contacts to silicon," in *Electron Devices Meeting, 1984 International*, pp. 742–745, IEEE, 1984.

[4] R. Peibst, U. Römer, Y. Larionova, M. Rienäcker, A. Merkle, N. Folchert, S. Reiter, M. Turcu, B. Min, J. Krügener, D. Tetzlaff, E. Bugiel, T. Wietler, and R. Brendel, "Working principle of carrier selective poly-Si/c-Si junctions: Is tunnelling the whole story?," *Solar Energy Materials and Solar Cells*, pp. –, 2016.

[5] A. H. M. Smets, K. Jäger, O. Isabella, R. A. van Swaaij, and M. Zeman, *Solar energy: The physics and engineering of photovoltaic conversion, technologies and systems*. Cambridge, England: UIT Cambridge Ltd, 2016.

[6] S. Philipps and W. Warmuth, "Photovoltaics report 2016." Presentation, 2016.

[7] J. Zhao, A. Wang, and M. A. Green, "24.5 % efficiency silicon PERT cells on MCZ substrates and 24.7 % efficiency PERL cells on FZ substrates," *Progress in Photovoltaics: Research and Applications*, vol. 7, no. 6, pp. 471–474, 1999.

[8] J. Zhao, A. Wang, P. Altermatt, and M. A. Green, "24 % efficient silicon solar cells with double layer antireflection coatings and reduced resistance loss," *Applied Physics Letters*, vol. 66, no. 26, pp. 3636–3638, 1995.

[9] F. Feldmann, M. Bivour, C. Reichel, M. Hermle, and S. W. Glunz, "Passivated rear contacts for high-efficiency n-type Si solar cells providing high interface passivation quality and excellent transport characteristics," *Solar Energy Materials and Solar Cells*, vol. 120, pp. 270–274, 2014.

[10] J.-P. Colinge and C. A. Colinge, *Physics of semiconductor devices*. Springer Science & Business Media, 2005.

[11] D. A. Neamen, *Semiconductor physics and devices: Basic principles*. New York: McGraw-Hill Higher Education, 4th ed., international ed. ed., 2012.

[12] P. Würfel and U. Würfel, *Physics of solar cells: From basic principles to advanced concepts*. Physics textbook, Weinheim: Wiley-VCH, 2nd, updated and expanded ed., 2009.

[13] D. J. Griffiths and E. G. Harris, "Introduction to quantum mechanics," *American Journal of Physics*, vol. 63, no. 8, pp. 767–768, 1995.

[14] D. J. Griffiths and R. College, *Introduction to electrodynamics*, vol. 3. prentice Hall Upper Saddle River, NJ, 1999.

[15] A. Richter, S. W. Glunz, F. Werner, J. Schmidt, and A. Cuevas, "Improved quantitative description of Auger recombination in crystalline silicon," *Physical Review B*, vol. 86, no. 16, pp. 1–14, 2012.

[16] A. G. Aberle, "Surface passivation of crystalline silicon solar cells: A review," *Progress in Photovoltaics: Research and Applications*, vol. 8, no. 5, pp. 473–487, 2000.

[17] H. Angermann, W. Henrion, A. Röseler, and M. Rebien, "Wet-chemical passivation of Si(111)- and Si(100)-substrates," *Materials Science and Engineering: B*, vol. 73, no. 1–3, pp. 178 – 183, 2000.

[18] A. G. Aber;e, S. Glunz, and W. Warta, "Field effect passivation of high efficiency silicon solar cells," *Solar Energy Materials and Solar Cells*, vol. 29, no. 2, pp. 175 – 182, 1993.

[19] M. Ghannam, G. Shehadah, Y. Abdulraheem, and J. Poortmans, "Basic understanding of the role of the interfacial inversion layer in the operation of silicon solar cells with a-Si/c-Si heterojunction (HIT)," in *the 28th European Photovoltaic Solar Energy Conference and Exhibition, Paris, France*, vol. 30, 2013.

[20] J. Dziewior and W. Schmid, "Auger coefficients for highly doped and highly excited silicon," *Applied Physics Letters*, vol. 31, no. 5, pp. 346–348, 1977.

[21] F. Feldmann, *Carrier-selective contacts for high-efficiency Si solar cells*. Dissertation, Universität Freiburg, Freiburg, 2015.

[22] M. Zeman and D. Zhang, "Heterojunction silicon based solar cells," in *Physics and Technology of Amorphous-Crystalline Heterostructure Silicon Solar Cells* (W. G. J. H. M. van Sark, L. Korte, and F. Roca, eds.), pp. 13–43, Berlin, Heidelberg: Springer Berlin Heidelberg, 2012.

[23] S. de Wolf, A. Descoeudres, Z. C. Holman, and C. Ballif, "High-efficiency silicon heterojunction solar cells: A review," *Green*, vol. 0, no. 0, p. to be published, 2012.

[24] K. Wakisaka, M. Taguchi, T. Sawada, M. Tanaka, T. Matsuyama, T. Matsuoka, S. Tsuda, S. Nakano, Y. Kishi, and Y. Kuwano, eds., *More than 16% solar cells with a new 'HIT' (doped a-Si/nondoped a-Si/crystalline Si) structure: Photovoltaic Specialists Conference, 1991., Conference Record of the Twenty Second IEEE*, 1991.

[25] K. Masuko, M. Shigematsu, T. Hashiguchi, D. Fujishima, M. Kai, N. Yoshimura, T. Yamaguchi, Y. Ichihashi, T. Mishima, N. Matsubara, T. Yamanishi, T. Takahama, M. Taguchi, E. Maruyama, and S. Okamoto, "Achievement of more than 25% conversion efficiency with crystalline silicon heterojunction solar cell," *IEEE Journal of Photovoltaics*, vol. 4, no. 6, pp. 1433–1435, 2014.

[26] D. W. Stefaan, D. Antoine, H. Z. C., and B. Christophe, *green*, vol. 2, ch. High-efficiency Silicon Heterojunction Solar Cells: A Review, p. 7. 2017 2012. 1.

[27] F. Feldmann, K.-U. Ritzau, M. Bivour, A. Moldovan, S. Modi, J. Temmler, M. Hermle, and S. W. Glunz, "High and low work function materials for passivated contacts," *Energy Procedia*, vol. 77, pp. 263–270, 2015.

[28] Post, I. R. C., P. Ashburn, and G. R. Wolstenholme, "Polysilicon emitters for bipolar transistors: A review and re-evaluation of theory and experiment," *IEEE Transactions on Electron Devices*, vol. 39, no. 7, pp. 1717–1731, 1992.

[29] F. A. Lindholm, A. Neugroschel, M. Arienzo, and P. A. Iles, "Heavily doped polysilicon-contact solar cells," *IEEE Electron Device Letters*, vol. 6, no. 7, pp. 363–365, 1985.

[30] E. Yablonovitch and T. Gmitter, "A study of n-SIPOS:p-Si heterojunction emitters," *IEEE Electron Device Letters*, vol. 6, no. 11, pp. 597–599, 1985.

[31] N. G. Tarr, "A polysilicon emitter solar cell," *IEEE Electron Device Letters*, vol. 6, no. 12, pp. 655–658, 1985.

[32] P. Borden, L. Xu, B. McDougall, C. P. Chang, D. Pysch, P. Voisin, and S. W. Glunz, "Polysilicon tunnel junctions as alternates to diffused junctions," in *23rd EU PVSEC*, pp. 1149–1152, 2008.

[33] F. Feldmann, M. Bivour, C. Reichel, M. Hermle, and S. W. Glunz, "A passivated rear contact for high-efficiency n-type silicon solar cells enabling high V_{oc} and FF>82%: Proceedings of the 29th eupvsec, paris, france," in *28th EU PVSEC*, p. to be published, 2013.

[34] Asuha, S.-S. Im, M. Tanaka, S. Imai, M. Takahashi, and H. Kobayashi, "Formation of 10-30 nm SiO_2/Si

structure with a uniform thickness at ~120 °C by nitric acid oxidation method," *Surface Science*, vol. 600, no. 12, pp. 2523–2527, 2006.

[35] Asuha, S. Imai, M. Takahashi, and H. Kobayashi, "Nitric acid oxidation of silicon at ~120 °C to form 3.5-nm SiO_2/Si structure with good electrical characteristics," *Applied Physics Letters*, vol. 85, no. 17, pp. 3783–3785, 2004.

[36] H. Kobayashi Asuha, O. Maida, M. Takahashi, and H. Iwasa, "Nitric acid oxidation of Si to form ultra-thin silicon dioxide layers with a low leakage current density," *Journal of Applied Physics*, vol. 94, no. 11, pp. 7328–7335, 2003.

[37] Christian K Fink, Ken Nakamura, Shingo Ichimura, and Stephen J Jenkins, "Silicon oxidation by ozone," *Journal of Physics: Condensed Matter*, vol. 21, no. 18, p. 183001, 2009.

[38] Karim M. Gad, Daniel Vössing, Patrice Balamou, Daniel Hiller, Bert Stegemann, Heike Angermann, and Martin Kasemann, "Improved Si/SiO_x interface passivation by ultra-thin tunneling oxide layers prepared by rapid thermal oxidation," *Applied Surface Science*, vol. 353, pp. 1269–1276, 2015.

[39] Anamaria Moldovan, Frank Feldmann, Martin Zimmer, Jochen Rentsch, Jan Benick, and Martin Hermle, "Tunnel oxide passivated carrier-selective contacts based on ultra-thin SiO_2 layers," *Solar Energy Materials and Solar Cells*, vol. 142, pp. 123–127, 2015.

[40] F. Feldmann, M. Simon, M. Bivour, C. Reichel, M. Hermle, and S. W. Glunz, "Efficient carrier-selective p- and n-contacts for Si solar cells," *Solar Energy Materials and Solar Cells*, vol. 131, no. 0, pp. 100–104, 2014.

[41] S. W. Glunz, F. Feldmann, A. Richter, M. Bivour, C. Reichel, H. Steinkemper, J. Benick, and M. Hermle, "The irresistible charm of a simple current flow pattern – 25% with a solar cell featuring a full-area back contact," in *31st EU PVSEC*, pp. 259–263, 2015.

[42] Di Yan, A. Cuevas, Y. Wan, and J. Bullock, "Passivating contacts for silicon solar cells based on boron-diffused recrystallized amorphous silicon and thin dielectric interlayers," *Solar Energy Materials and Solar Cells*, vol. 152, pp. 73–79, 2016.

[43] C. M. Maritan and N. G. Tarr, "Polysilicon emitter p-n-p transistors," *IEEE Transactions on Electron Devices*, vol. 36, pp. 1139–1144, Jun 1989.

[44] J. Snel, "The doped Si/SiO_2 interface," *Solid-State Electronics*, vol. 24, no. 2, pp. 135–139, 1981.

[45] J. Y. Gan and R. M. Swanson, "Polysilicon emitters for silicon concentrator solar cells," in *Polysilicon emitters for silicon concentrator solar cells* (J. Y. Gan and R. M. Swanson, eds.), pp. 245–250, IEEE Explore, 1990.

[46] M. Bivour, J. Temmler, H. Steinkemper, and M. Hermle, "Molybdenum and tungsten oxide: High work function wide band gap contact materials for hole selective contacts of silicon solar cells," *Solar Energy Materials and Solar Cells*, vol. 142, pp. 34–41, 2015.

[47] C. Battaglia, S. M. de Nicolãs, S. D. Wolf, X. Yin, M. Zheng, C. Ballif, and A. Javey, "Silicon heterojunction solar cell with passivated hole selective MoO_x contact," *Applied Physics Letters*, vol. 104, no. 11, p. 113902, 2014.

[48] B. Liao, B. Hoex, A. G. Aberle, D. Chi, and C. S. Bhatia, "Excellent c-Si surface passivation by low-temperature atomic layer deposited titanium oxide," *Applied Physics Letters*, vol. 104, no. 25, p. 253903, 2014.

[49] T. G. Allen and A. Cuevas, "Electronic passivation of silicon surfaces by thin films of atomic layer deposited gallium oxide," *Applied Physics Letters*, vol. 105, no. 3, p. 031601, 2014.

[50] U. Römer, R. Peibst, T. Ohrdes, B. Lim, J. Krügener, E. Bugiel, T. Wietler, and R. Brendel, "Recombination

behavior and contact resistance of n+ and p+ poly-crystalline Si/mono-crystalline Si junctions," *Solar Energy Materials and Solar Cells*, vol. 131, pp. 85–91, 2014.

[51] M. Stodolny, M. Lenes, Y. Wu, G. Janssen, I. Romijn, J. Luchies, and L. Geerligs, "n-type polysilicon passivating contact for industrial bifacial n-type solar cells," *Solar Energy Materials and Solar Cells*, 2016.

[52] G. Yang, A. Ingenito, O. Isabella, and M. Zeman, "IBC c-Si solar cells based on ion-implanted poly-silicon passivating contacts," *Solar Energy Materials and Solar Cells*, 2016.

[53] "Passivated tunneling contacts to n-type wafer silicon and their implementation into high performance solar cells: Preprint," 2014.

[54] W. Nemeth, V. LaSalvia, M. R. Page, E. L. Warren, A. Dameron, A. G. Norman, B. G. Lee, D. L. Young, and P. Stradins, "Implementation of tunneling pasivated contacts into industrially relevant n-Cz Si solar cells," in *Photovoltaic Specialist Conference (PVSC), 2015 IEEE 42nd*, pp. 1–3, June 2015.

[55] Y. Tao, E. L. Chang, A. Upadhyaya, B. Roundaville, Y. W. Ok, K. Madani, C. W. Chen, K. Tate, V. Upadhyaya, F. Zimbardi, J. Keane, A. Payne, and A. Rohatgi, "730 mv implied V_{oc} enabled by tunnel oxide passivated contact with PECVD grown and crystallized n+ polycrystalline Si," in *Photovoltaic Specialist Conference (PVSC), 2015 IEEE 42nd*, pp. 1–5, June 2015.

[56] H. C. de Graaff and J. G. de Groot, "The sis tunnel emitter: A theory for emitters with thin interface layers," *IEEE Transactions on Electron Devices*, vol. 26, pp. 1771–1776, Nov 1979.

[57] R. Peibst, U. Römer, K. R. Hofmann, B. Lim, T. F. Wietler, J. Krügener, N. P. Harder, and R. Brendel, "A simple model describing the symmetric I-V characteristics of p-Polycrystalline Si/n-Monocrystalline Si, and n-Polycrystalline Si/p-Monocrystalline Si junctions," *IEEE Journal of Photovoltaics*, vol. 4, pp. 841–850, May 2014.

[58] B. Fischer, *Loss analysis of crystalline silicon solar cells using photoconductance and quantum efficiency measurements*. Cuvillier, 2003.

[59] W. Kern *et al.*, *Handbook of semiconductor wafer cleaning technology*. 1993.

[60] W. Kern, *Thin film processes II*, vol. 2. Academic press, 2012.

[61] H. Kobayashi, K. Imamura, W.-B. Kim, S.-S. Im, *et al.*, "Nitric acid oxidation of Si (NAOS) method for low temperature fabrication of SiO_2/Si and SiO_2/SiC structures," *Applied Surface Science*, vol. 256, no. 19, pp. 5744–5756, 2010.

[62] K. Wolke, C. Gottschalk, J. Rentsch, and H. Angermann, "Ozone based chemical oxide growth for crystalline solar cell production," in *Solid State Phenomena*, vol. 187, pp. 321–324, Trans Tech Publ, 2012.

[63] H. Angermann, K. Wolke, C. Gottschalk, A. Moldovan, M. Roczen, J. Fittkau, M. Zimmer, and J. Rentsch, "Electronic interface properties of silicon substrates after ozone based wet-chemical oxidation studied by SPV measurements," *Applied Surface Science*, vol. 258, no. 21, pp. 8387–8396, 2012.

[64] A. Moldovan, F. Feldmann, G. Krugel, M. Zimmer, J. Rentsch, M. Hermle, A. Roth-Fölsch, K. Kaufmann, and C. Hagendorf, "Simple cleaning and conditioning of silicon surfaces with UV/Ozone sources," *Energy Procedia*, vol. 55, pp. 834 – 844, 2014.

[65] S. L. Wu, D. M. Chiao, C. L. Lee, and T. F. Lei, "Characterization of thin textured tunnel oxide prepared by thermal oxidation of thin polysilicon film on silicon," *IEEE Transactions on Electron Devices*, vol. 43, pp. 287–294, Feb 1996.

[66] S. Janz, *Amorphous silicon carbide for photovoltaic applications*. PhD thesis, 2006.

[67] W. Van Sark, "Methods of deposition of hydrogenated amorphous silicon for device applications," *Thin Films and Nanostructures*, vol. 30, pp. 1–216, 2002.

[68] M. Brodsky, "On the deposition of amorphous silicon films from glow discharge plasmas of silane," *Thin Solid Films*, vol. 40, pp. L23–L25, 1977.

[69] R. Ross and J. Jaklik Jr, "Plasma polymerization and deposition of amorphous hydrogenated silicon from RF and DC silane plasmas," *Journal of applied physics*, vol. 55, no. 10, pp. 3785–3794, 1984.

[70] J. Williams, "Solid phase epitaxial regrowth phenomena in silicon," *Nuclear Instruments and Methods in Physics Research*, vol. 209, pp. 219 – 228, 1983.

[71] B. Pawlak, W. Vandervorst, A. Smith, N. E. Cowern, B. Colombeau, and X. Pages, "Enhanced boron activation in silicon by high ramp-up rate solid phase epitaxial regrowth," *Applied Physics Letters*, vol. 86, no. 10, p. 101913, 2005.

[72] B. Gorka, *Hydrogen passivation of polycrystalline Si thin film solar cells*. PhD thesis, HZB, 2010.

[73] S. Lindekugel, H. Lautenschlager, T. Ruof, and S. Reber, "Plasma hydrogen passivation for crystalline silicon thin-films," in *23rd EU PVSEC*, pp. 2232–2235, 2008.

[74] R. A. Sinton and A. Cuevas, "Contactless determination of current–voltage characteristics and minority-carrier lifetimes in semiconductors from quasi-steady-state photoconductance data," *Applied Physics Letters*, vol. 69, no. 17, pp. 2510–2512, 1996.

[75] D. E. Kane and R. M. Swanson, "Measurement of the emitter saturation current by a contactless photoconductivity decay method (silicon solar cells)," in *18th IEEE Photovoltaic Specialists Conference Las Vegas*, pp. 578–583, 1985.

[76] A. Kimmerle, J. Greulich, and A. Wolf, "Carrier-diffusion corrected J_0-analysis of charge carrier lifetime measurements for increased consistency," *Solar Energy Materials and Solar Cells*, vol. 142, pp. 116–122, 2015.

[77] H. Tompkins and E. A. Irene, *Handbook of ellipsometry*. William Andrew, 2005.

[78] C. Herzinger, B. Johs, W. McGahan, J. A. Woollam, and W. Paulson, "Ellipsometric determination of optical constants for silicon and thermally grown silicon dioxide via a multi-sample, multi-wavelength, multi-angle investigation," *Journal of Applied Physics*, vol. 83, no. 6, pp. 3323–3336, 1998.

[79] T. Ambridge and M. M. Faktor, "An automatic carrier concentration profile plotter using an electrochemical technique," *Journal of Applied Electrochemistry*, vol. 5, no. 4, pp. 319–328, 1975.

[80] P. Analysis, "Electrochemical CV-Profiling," feb 2016.

[81] P. Blood, "Capacitance-voltage profiling and the characterisation of III-V semiconductors using electrolyte barriers," *Semiconductor Science and technology*, vol. 1, no. 1, p. 7, 1986.

[82] D. K. Schroder, *Semiconductor material and device characterization*. John Wiley & Sons, 2006.

[83] K. R. McIntosh and P. P. Altermatt, "A freeware 1D emitter model for silicon solar cells," in *2010 35th IEEE Photovoltaic Specialists Conference*, pp. 002188–002193, June 2010.

[84] K. R. McIntosh, P. P. Altermatt, T. J. Ratcliff, K. C. Fong, L. E. Black, S. C. Baker-Finch, M. D. Abbott, *et al.*, "An examination of three common assumptions used to simulate recombination in heavily doped silicon," *Proceedings of the 28th EU PVSEC, Paris*, pp. 1672–1679, 2013.

[85] D. Klaassen, "A unified mobility model for device simulation. model equations and concentration dependence," *Solid-State Electronics*, vol. 35, no. 7, pp. 953–959, 1992.

[86] A. Schenk, "Finite-temperature full random-phase approximation model of band gap narrowing for silicon device simulation," *Journal of Applied Physics*, vol. 84, no. 7, pp. 3684–3695, 1998.

[87] A. Goetzberger and R. Scarlett, "Research and investigation of inverse epitaxial UHF power transistors," tech. rep., DTIC Document, 1964.

[88] S. Eidelloth and R. Brendel, "Analytical theory for extracting specific contact resistances of thick samples from the transmission line method," *IEEE Electron Device Letters*, vol. 35, no. 1, pp. 9–11, 2014.

[89] A. Fell, "A free and fast three-dimensional/two-dimensional solar cell simulator featuring conductive boundary and quasi-neutrality approximations," *IEEE Transactions on Electron Devices*, vol. 60, no. 2, pp. 733–738, 2013.

[90] L. E. Guerra Flores, F. Fraunhofer-Institut für Solare Energiesysteme-ISE, A.-L.-U. Freiburg, and S. Glunz, "Analysis and process optimization of a passivated contact for p-type si solar cells," 01.01.2015.

[91] G. Nogay, J. Stuckelberger, P. Wyss, Q. Jeangros, C. Allebã, X. Niquille, F. Debrot, M. Despeisse, F.-J. Haug, P. Lãper, and C. Ballif, "Silicon-rich silicon carbide hole-selective rear contacts for crystalline-silicon-based solar cells," *ACS Applied Materials & Interfaces*, vol. 8, no. 51, pp. 35660–35667, 2016. PMID: 27959489.

[92] G. S. Oehrlein, S. A. Cohen, and T. O. Sedgwick, "Diffusion of phosphorus during rapid thermal annealing of ion-implanted silicon," *Applied Physics Letters*, vol. 45, no. 4, pp. 417–419, 1984.

[93] R. J. Carter, E. Cartier, A. Kerber, L. Pantisano, T. Schram, S. D. Gendt, and M. Heyns, "Passivation and interface state density of SiO_2/HfO_2-based polycrystalline-Si gate stacks," *Applied Physics Letters*, vol. 83, no. 3, pp. 533–535, 2003.

[94] P. John, I. Odeh, M. Thomas, M. Tricker, J. Wilson, and R. Dhariwal, "Physical degradation of a-Si films on thermal treatment: a scanning electron microscope study," *Journal of Materials Science*, vol. 16, no. 5, pp. 1305–1309, 1981.

[95] F. Feldmann, "Advanced passivated contacts and their applications to high-efficiency cells," in *25th Workshop on Crystalline Silicon Solar Cells & Modules: Materials and Processes*, 2015.

[96] M. Schnabel, P. Löper, S. Gutsch, P. R. Wilshaw, and S. Janz, "Thermal oxidation and encapsulation of silicon–carbon nanolayers," *Thin Solid Films*, vol. 527, pp. 193–199, 2013.